Titre: Title: Initialization Methods of Inverter-Based Resources for Accelerated Computation of Power System Transients

Auteur: Author: Juan Antonio Ocampo Wilches

Date: 2026

Type: Mémoire ou thèse / Dissertation or Thesis

Référence: Citation: Ocampo Wilches, J. A. (2026). Initialization Methods of Inverter-Based Resources for Accelerated Computation of Power System Transients [Ph.D. thesis, Polytechnique Montréal]. PolyPublie. https://publications.polymtl.ca/76593/

URL de PolyPublie: PolyPublie URL: https://publications.polymtl.ca/76593/

Directeurs de recherche: Advisors: Jean Mahseredjian

Programme: Program: Génie électrique

POLYTECHNIQUE MONTRÉAL

affiliée à l'Université de Montréal

Initialization Methods of Inverter-Based Resources for Accelerated Computation of Power System Transients

JUAN ANTONIO OCAMPO WILCHES

Département de génie électrique

Thèse présentée en vue de l'obtention du diplôme de *Philosophiæ Doctor*

Génie électrique

Avril 2026

POLYTECHNIQUE MONTRÉAL

affiliée à l'Université de Montréal

Cette thèse intitulée:

Initialization Methods of Inverter-Based Resources for Accelerated Computation of Power System Transients

présenté par **Juan Antonio OCAMPO WILCHES**

en vue de l'obtention du diplôme de *Philosophiæ Doctor*

a été dûment accepté par le jury d'examen constitué de :

Antoine LESAGE-LANDRY, président

Jean MAHSEREDJIAN, membre et directeur de recherche

Omar SAAD, membre

Omid BEIK, membre externe

DEDICATION

To my family, for their encouragement.

To Laura, for her support.

To my friends, for their companionship.

ACKNOWLEDGEMENTS

I would first like to thank my supervisor, Prof. Jean Mahseredjian, for the guidance, patience, and understanding he showed me. His mentorship has been fundamental to my personal and professional growth. I also appreciate the support from my research collaborators, Prof. Ahda Pavani and Prof. Abner Ramirez, who guided me even when I doubted my own abilities and capabilities.

I could not be more grateful to Dr. Keijo Jacob for his invaluable and constant support during this research. His continuous encouragement, mentorship, and overall ability to listen and guide me made his presence fundamental to reaching this point in my work.

I would also like to thank the members of my examination committee for their direct and indirect contributions to my progress.

To my friends Ahmad Allabadi, Anoosh Dini, Emmanuel François, Haoyan Xue, Ruyguara Meyberg, Nicolas Mora, Marios Salepsis, Afaf Allabadi, Armin Mirnikjoo, Mohammad Jafari, Kouamé Abraham N'Zi, and Renan Furlaneto: thank you for accompanying me and offering your continuous feedback and companionship during this time.

Finally, a special thank you to my family: Laura, my support and motivation during the difficult times and happy moments; my parents, Federico and Luisa, for always giving me the wings and confidence I needed to reach even further than what I considered possible; and my sister and brother, Ana and Luis, for their encouraging words. To all of you, thank you for being my source of strength and motivation.

RÉSUMÉ

Les ressources basées sur des convertisseurs (IBR, sigle en anglais), telles que les parcs photovoltaïques, les éoliennes à convertisseur pleine échelle et les générateurs asynchrones à double alimentation (DFIG, sigle en anglais), sont devenues des éléments essentiels des réseaux modernes de transmission et de distribution. Les études des transitoires électromagnétiques (EMT) sont indispensables pour analyser leur interaction avec le réseau, ainsi que leur protection et leur contrôle. Cependant, elles deviennent coûteuses en temps de calcul et sujettes à des erreurs lorsque les modèles démarrent avec des conditions initiales arbitraires.

Cette thèse propose une analyse des méthodes existantes et de nouvelles avancées pour l'initialisation des IBR. Le processus développé détermine les états de commande, mécaniques et électriques de chaque sous-modèle, ce qui permet aux simulations EMT de commencer directement au point de fonctionnement réel. En alignant le modèle temporel avec la solution du flux de charge, la procédure réduit fortement les transitoires initiaux et le coût de calcul.

L'approche repose sur trois étapes : (i) un calcul de flux de charge multi phasé établit le point de fonctionnement, (ii) les éléments passifs et synchrones sont initialisés, et (iii) les états des convertisseurs et des parties mécaniques sont reconstruits à leur consigne stationnaire. Implémentée dans EMTP et testée sur différents cas de référence, elle montre jusqu'à 92 % de réduction du temps de simulation, la suppression de transitoires indésirables et une meilleure robustesse numérique.

Enfin, une variante hybride est proposée pour les modèles « boîte grise » ou « boîte noire », où la logique interne est partiellement ou totalement inaccessible. Elle combine la solution de flux de charge avec des indices comportementaux limités (courbes constructeur, mesures expérimentales), permettant encore des gains de 70 à 85 % et étendant l'applicabilité aux bibliothèques propriétaires.

ABSTRACT

Inverter-based resources (IBR), including photovoltaic parks (PV), full-scale-converter wind turbines (FSC), and doubly-fed induction generators (DFIG), are now a fundamental component throughout modern transmission and distribution networks. Electromagnetic transient (EMT) studies are fundamental for understanding the interactions of these devices with the grid, their protection, and control. Yet, such studies become prohibitively slow and susceptible to error when models start from arbitrary initial conditions and try to readjust toward the true operating point.

This thesis undertakes a comprehensive review of existing methods and introduces new advances for the initialization of IBRs. The proposed initialization process determines the control, mechanical, and electrical states of each model or sub-network, ensuring that EMT simulations start from the correct operating point. By aligning the time-domain model with the converged load-flow solution, the procedure minimizes initial transients and significantly reduces the computational cost of EMT studies.

This dissertation evaluates the impact of IBR initialization, implementing a three-stage framework that drives large-scale EMT models to the steady-state solution, thereby reducing computational cost while minimizing unwanted transients.

The proposed methodology is divided into a three-stage workflow: (i) a multiphase load-flow establishes the network operating point, (ii) passive and synchronous elements are initialized to that solution, and (iii) converter and mechanical states are set so that every IBR is fixed at its steady-state set-point. The implementation of the proposed initialization in EMTP is evaluated against established techniques in various benchmarks, achieving up to 92% reductions in runtime, reducing unwanted transients, and improving computational cost. The comparative analysis, detailed in the following chapters, underscores the technique advantages and practical applicability.

A proposed hybrid initialization methodology is presented for grey-box and black-box inverter models, where only partial control logic is disclosed. It fuses the external load-flow solution with limited behavioural variables to estimate the IBR's behavior. Despite this reduced information, the method still delivers substantial computational savings, typically cutting EMT initialization time by 70–85 %, and extends the applicability of the workflow to proprietary libraries.

TABLE OF CONTENTS

LIST OF TABLES

LIST OF FIGURES

LIST OF SYMBOLS AND ABREVIATIONS

AVM	Average Value Model
BESS	Battery Energy Storage Systems
BTB	Back-to-back converter
CBA	Capacitor Balancing algorithms
CCS	Circulating Current Suppression
CG	Collector Grid
CP	Constant Parameters (line model)
DFIG	Doubly Fed Induction Generators
DI	Decoupled Initialization
DM	Detailed Model
DSO	Distribution system operator
EMT	Electromagnetic Transient
FCI	Full Control Initialization
FLL	Frequency Locked Loop
FOC	Field Oriented Control
FRT	Fault ride-through
GFEC	Generator with Front End Converter
GSC	Grid-Side Converter
HDI	Hybrid Decoupled Interface
HVDC	High Voltage DC
IA	Initialization Algorithm
IBR	Inverter-Based Resources
IG	Induction Generator

IGBT Insulated-Gate Bipolar Transistor

ISS Initialized Subsystem

IM Induction Machine

LF Load-Flow

LFSI Load-Flow and Source Initialization

MANA Modified Augmented Nodal Analysis approach

MMC Modular Multilevel Converters

MPPT Maximum Power Point Tracker

MSC Machine-Side Converter

NI No-Initialization

PCC Point of Common Coupling

PF Power Factor

PI Proportional Integral Controller

PID Proportional Integral Derivative Controller

PLL Phase-Locked Loop

PMSG Permanent Magnet Synchronous Generator

POI Point of Interconnection

PV Photovoltaic Systems

PVPC PV Park Controller

PWM Pulse Width Modulation

RSC Rotor-Side Converter

SCIG Squirrel-cage Induction Generator

SiC Silicone Carbide

STATCOM Static Synchronous Compensator

VSC Voltage-Source Converter

WP Wind Park

WPC Wind Park Controller

WT Wind Turbine

WTC Wind Turbine Controller

WTGU Wind turbine generating units

LIST OF APPENDICES

CHAPTER 1 INTRODUCTION

By 2025, variable renewable energy sources will have transitioned from marginal resources to a fundamental part of the global power supply. With global wind capacity reaching approximately 3 TW and solar PV increasing to 2.6 TW, wind and solar now meet approximately 15% of worldwide demand and account for most of the new growth in the power sector [1]. This transition has reshaped national energy profiles, with renewables now accounting for a significant portion of annual generation in several countries. During periods of high production, such as windy nights or sunny afternoons, renewable generation contributions to the system can be several times higher than the annual averages, meaning many synchronous areas now rely almost entirely on IBR for prolonged periods [2].

Under such conditions, IBR must ride through deep voltage droops, provide reactive power regulation, and increasingly contribute to active power frequency response and synthetic inertia [3]-[5]. Manufacturers, academia, and utilities have responded with advanced converter controls, transforming wind and solar plants into active system participants rather than passive bulk generators [5]-[6].

Modeling practices have progressed in parallel. In response, international standards and regional grid codes now define specific requirements for dynamic models for all major IBR technologies and their plant-level controllers [7]-[8]. These publicly documented frameworks provide a common foundation, enabling manufacturers, utilities, and researchers to exchange data and benchmark models.

However, accurately representing every individual unit in large-scale wind or solar parks, whether in megawatts or gigawatts, complicates time-domain stability studies, particularly when the broader system already includes numerous IBRs. Hence, aggregated or equivalent-machine methods, whether based on electrical equivalence, control-system aggregation, or parameter scaling, have become essential [9]-[11]. The primary challenge lies in finding the optimal balance between simulation efficiency and dynamic fidelity to accurately represent crucial phenomena, such as subsynchronous interactions, transient interactions, and post-fault power recovery.

While phasor-domain (RMS) simulations were adequate for traditional grids governed by the slow electromechanical dynamics of synchronous machines, this paradigm is no longer valid for modern grids. The proliferation of IBRs, whose behavior is dictated by fast-acting power electronics rather than physical inertia, introduces microsecond-scale dynamics that phasor-based tools cannot resolve [12]-[13]. Consequently, EMT simulations are now indispensable for analyzing fast converter controls, complex interactions, and non-sinusoidal fault responses. This necessary shift to high-fidelity EMT modeling introduces its own challenge: a far more complex initialization process is required to ensure that simulations start from a stable operating point derived from the load-flow (LF) solution [12]-[14].

For accurate EMT simulations, establishing the correct initial steady-state condition is crucial for effectively analyzing system dynamics [13]-[14]. Using arbitrary initialization conditions can result in high computational costs, as the system requires extended simulation times to achieve a steady-state. Thus, correctly initializing IBR models minimizes initial transients, lowering computational costs and improving simulation accuracy. Inadequate initialization may cause discrepancies in steady-state conditions, delays in operational points, unnecessary protection triggers, magnetic saturation, and prolonged transient behavior, especially within intricately modeled large power grids [15]-[16]. This issue is becoming increasingly important as the number of IBRs grows, since the complexity and interconnected dynamics result in notably longer initialization times.

This thesis focuses on the initialization of IBR models, generalizing the converter initialization, and automating the initialization for other inverter-based resources. It presents and validates dynamic models for wind turbine and solar PV plants that (i) can be implemented within any EMT software, and (ii) are scalable through effective aggregation techniques. Comparative case studies against existing techniques demonstrate that the proposed method provides appropriate initialization for critical electromechanical and converter dynamics at a significantly lower computational cost, thereby facilitating the secure and cost-effective operation of power systems where wind and solar energy increasingly contribute to generation.

1.1. Literature Review

This section reviews the literature on the initialization of power system EMT simulations, with a focus on networks with high penetration of IBR. It begins by establishing the context of the modern power grid and the increasing prevalence of IBR. It then focuses on the critical role of EMT simulations for analyzing such systems and identifies the core challenge of initialization. A comprehensive review of existing initialization techniques for both conventional power system components and various types of IBRs is presented. Finally, the chapter identifies key research gaps in current methodologies, particularly regarding proprietary and black-box models, thereby establishing the scientific contributions and objectives of this dissertation.

1.1.1 The Modern Power System and the Rise of IBR

The global energy landscape is undergoing a profound transformation, driven by the urgent need to decarbonize electricity production and meet ambitious environmental targets. This has led to the widespread integration of renewable energy sources, primarily wind and solar, into transmission and distribution networks. Unlike conventional power plants based on synchronous generators, these modern resources interface with the grid through power electronic converters, as shown in Figure 1.1 [17]. These technologies are collectively known as IBR.

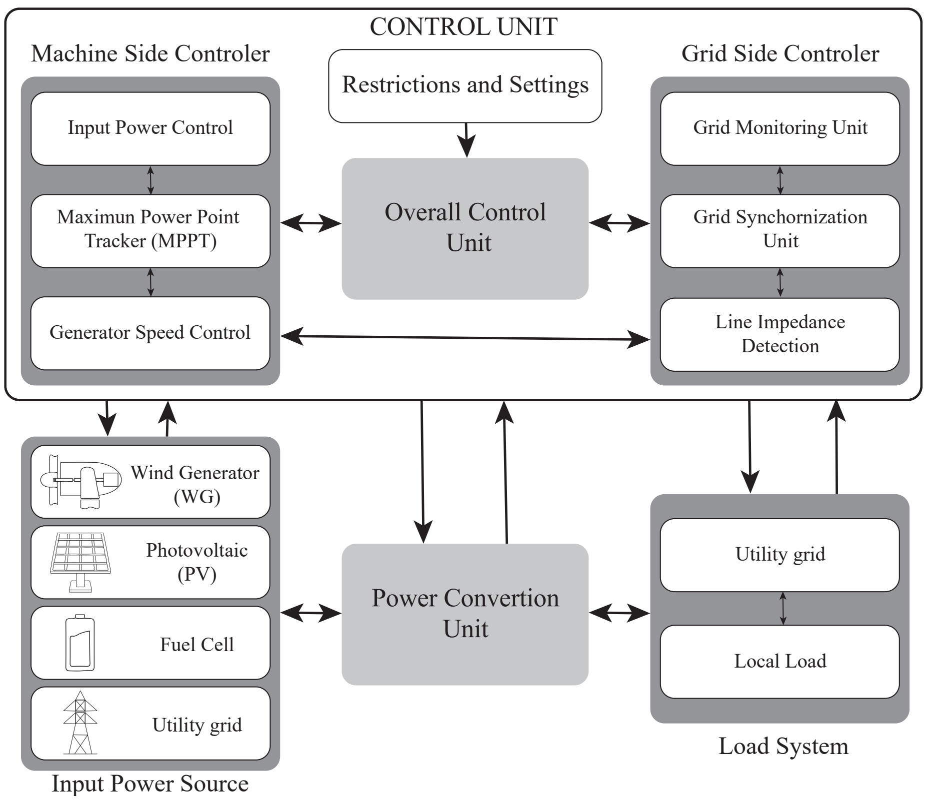

Figure 1.1 General control scheme for the IBR [17].

The evolution of wind power technology exemplifies this technological shift. Since the first aerogenerators were designed, the development of this technology has evolved at an exponential pace. The different kinds of wind generators can be grouped into the following categories [18]-[22]:

Type 1 (Fixed Speed WTGU): The first wind turbines had fixed-speed turbines and squirrel-cage induction generators (SCIG). The rated power was reached at 105% of synchronous speed, and the maximum slip is -1%. This type of generator only consumes reactive power and utilizes power electronics for the soft starting of the turbine.

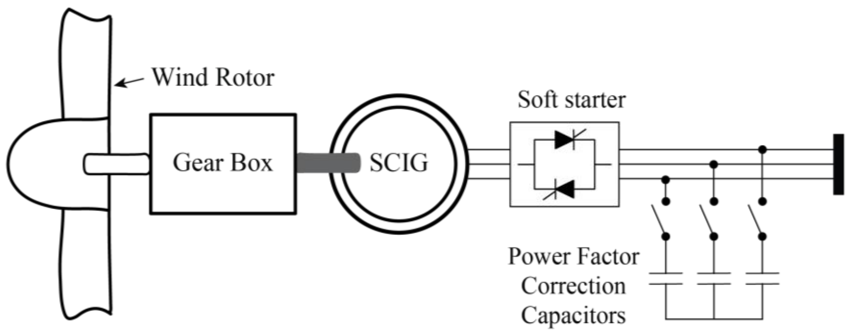

Figure 1.2 Wind Turbine type 1.

Type 2 (Semi-Variable Speed WTGU): The wound-rotor induction generator with external rotor resistance is the first wind turbine to incorporate specific control components. The improvement of its control allowed an increase in its pitch angle to 10%. This type of turbine also featured a rotor resistance controller, which enabled the control of real power output. This allowed the turbine to produce maximum power at its nominal speed and to reach the rated power once the rated wind speed was exceeded.

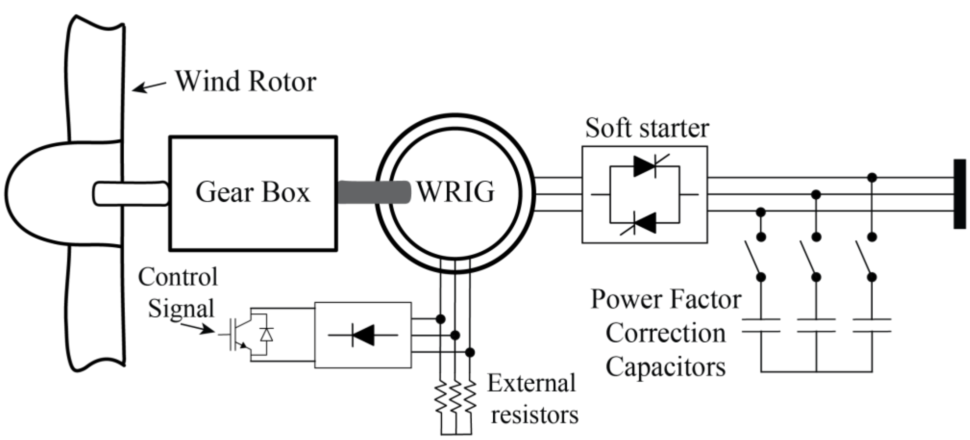

Figure 1.3 Wind Turbine type 2.

Type 3 (DFIG Wind Turbines): This kind of wind turbine is designed with a doubly-fed induction generator (DFIG), in a configuration that allows the rotor speed to slip from 30% to -30%, meaning that with a converter rated to 30% of the WT power, it is possible to control the full power of the generator. This model reduces the costs and complexity of the converter. The wind turbine is operated using a maximum power point tracking (MPPT) control below the nominal wind speed and at rated power after the nominal wind speed is reached. Today, these turbines are widely integrated into wind parks, as the control of the generated active and reactive power can be handled independently through the GSC and the RSC control.

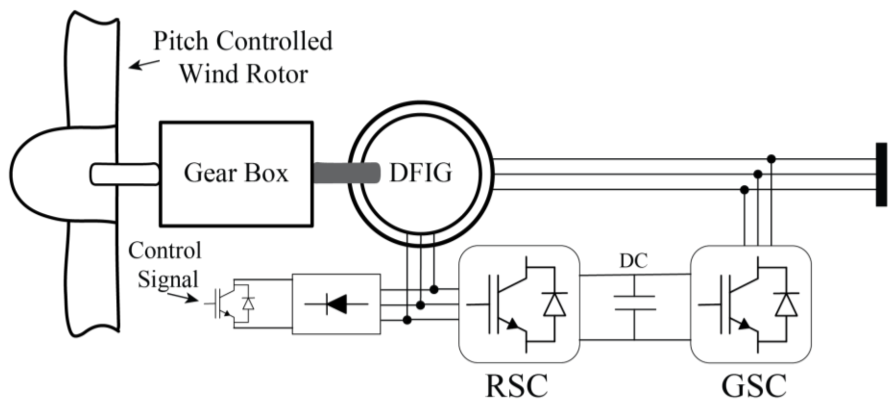

Figure 1.4 Wind Turbine type 3.

Type 4 (Full-Scale Converter Wind Turbine): In this generator, all the power generated is transmitted through the power converter. One of its main benefits is that the grid frequency can be controlled independently of the turbine frequency. Its mathematical model is more straightforward than that of the Type 3 WT model, and the dynamics of the Permanent Magnet Synchronous Generator (PMSG) can be isolated from the grid. This technological difference results in reduced losses and increased torque of the generator.

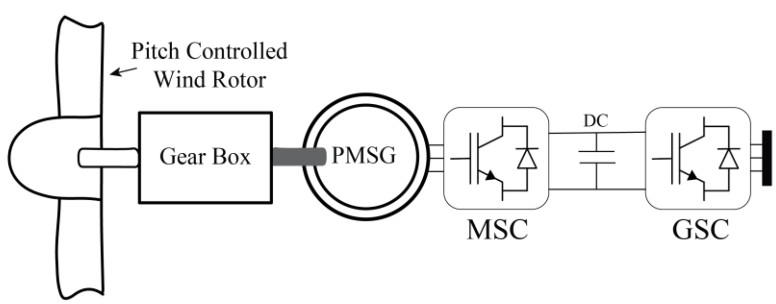

Figure 1.5 Wind Turbine type 4.

Similarly, photovoltaic (PV) parks, the other major class of IBRs, have various configurations depending on their scale and design philosophy. For PV modelling, there exist four basic configurations [23]-[25]:

A) Microinverter: The easiest way to connect the solar panels into an expandable solar farm is by using independent microinverters for each module. However, this configuration is often discarded for large PV farms due to the increase in its cost and maintenance requirements.

B) String Inverters: Multiple panels are connected in a series "string," which then connects to a single inverter.

C) Multi-string Inverters: This is the most common solution for large parks. It combines multiple strings, each with its own DC-DC boost converter for independent MPPT, into a central inverter. This implementation has two significant advantages compared to B): The boost controllers facilitate the MPPT and enable more complex control schemes for fault ride-through [25].

D) Central Inverters: For very large PV parks, the most straightforward solution is using a single, large central inverter. However, due to the variation in solar irradiance at different points within the solar farm, this approach is not always the most accurate or efficient option.

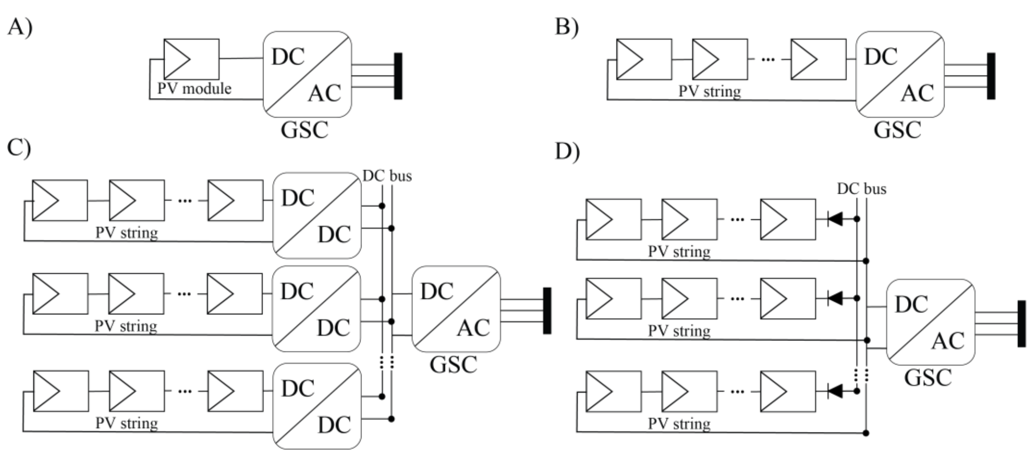

Figure 1.6 PV park configurations.

The fundamental difference between these IBR and traditional synchronous generators lies in their power electronic interfaces. This interface decouples the prime mover (turbine blades or PV cells) from the grid frequency, thereby altering grid dynamics. These include reduced system inertia, altered fault-current characteristics, and the potential for complex, high-frequency control interactions. These new challenges make it necessary to use highly detailed simulation tools to ensure the safe and reliable operation of the modern power system.

1.1.2 The Role of EMT Simulations

To analyze the complex interactions introduced by IBR, power system engineers rely on time-domain simulations. Among these, EMT simulations offer the highest level of detail [26]. Unlike steady-state LF, which calculates a single operating point, or phasor-domain dynamic simulations, which model electromechanical oscillations over seconds, EMT simulations solve the system's differential equations in the time-domain with small numerical integration time-steps (typically on the order of microseconds) [13]. This fidelity is essential for studying high-frequency phenomena such as switching transients, control system interactions, subsynchronous resonance, and protection system performance.

A key aspect of EMT studies is the modeling fidelity, which must be appropriate for the studied phenomenon. The models for induction generators used in wind turbines illustrate this concept well:

- **Fifth-Order Model:** Also known as the full EMT Model, it is the most detailed representation. It includes all the non-ideal characteristics of the induction generator and captures the dynamics of both stator and rotor fluxes. This level of detail is necessary to study the harmonic response of the wind turbine and its interaction with the grid's electrical components [27]-[33]. The complexity is represented by a system of differential equations governing the machine's fluxes and currents.

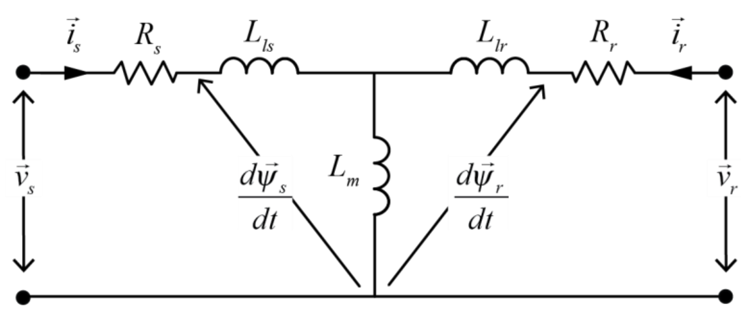

Figure 1.7 Fifth-order model generator.

$$\vec{v}_s = \vec{i}_s R_s + j\omega_s \vec{\psi}_s + \frac{d\vec{\psi}_s}{dt} \tag{1.1}$$

$$\vec{v}_r = 0 = \vec{i}_r R_r + j\left(\omega_s - \omega_r\right)\vec{\psi}_r + \frac{d\vec{\psi}_r}{dt} \tag{1.2}$$

The flux is calculated based on the current, as detailed in

$$\vec{\psi}_s = \vec{i}_s\left(L_{sl} + L_m\right) + \vec{i}_r L_m \tag{1.3}$$

$$\vec{\psi}_r = \vec{i}_r\left(L_{rl} + L_m\right) + \vec{i}_s L_m \tag{1.4}$$

- **Third-Order Model:** This model, also known as the electromechanical transient model, offers a simplification by neglecting the stator flux dynamics. This is equivalent to ignoring the DC transient component in the stator current. While this reduces the model's order and computational cost, it is only accurate for phenomena near the fundamental frequency. It is widely used in nominal frequency stability studies to reduce computation time compared to the fifth-order model [28], [34]-[37].

$$\vec{v}_s = \vec{i}_s R_s + j\omega_s \vec{\psi}_s \tag{1.5}$$

$$0 = \vec{i}_r R_r + j\left(\omega_s - \omega_r\right)\vec{\psi}_r + \frac{d\vec{\psi}_r}{dt} \tag{1.6}$$

- **First-Order Model:** This is the simplest representation, often called the steady-state model. It neglects all electrical dynamics of the turbine and considers only the mechanical dynamics [34]. This model is generally unsuitable for most transient studies, but it can be helpful in understanding the purely mechanical response of the system.

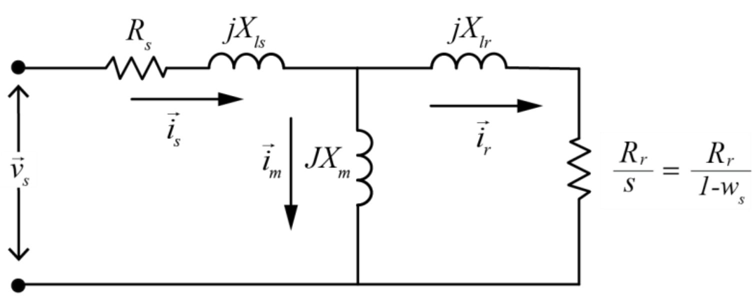

Figure 1.8 First-order model generator.

The necessity of using high-fidelity models, such as the fifth-order representation for the induction generator, underscores the computational challenge.

As with the induction generator, the converters also need to be modeled based on the required level of detail. Voltage-source converters (VSCs) govern grid interaction, power regulation, and protection response. Because of their nonlinear switching, fast control loops, and coupling with non-linear generator models, models are selected based on the level of detail required and the intended study objective.

Following CIGRE classifications [36]-[37], converter models can be grouped by fidelity and computational complexity:

- **Type 1 – Physics-based model:** Include semiconductor-level and parasitic element representation (e.g., IGBT or SiC behavior). Used for validating switching losses or converter hardware, but impractical for system-level EMT studies.
- **Type 2 – Detailed switching model:** Explicitly reproduce switching states and modulation patterns. Applied in fault, protection, or control interaction studies of a single wind or PV converter where microsecond resolution is needed.
- **Type 3 – Simplified switch model:** Replace switches with equivalent resistances or logic states to emulate conduction and blocking. Reduce complexity while maintaining switch-level logic—suitable for converter start-up and fault-injection analysis.
- **Type 4 – Detailed equivalent model (DM):** Aggregate submodules or converter cells into equivalent controlled sources or admittance networks. Commonly used in large systems where multiple PV or wind parks are modeled without simulating every switch.
- **Type 5 – Average-value model (AVM):** Represent converter behavior using averaged voltage or current sources derived from the modulation process. They capture grid dynamics, control loops, and DC-link behavior efficiently and are standard for EMT studies of large IBR plants.
- **Type 6 – Phasor models:** Operate at the fundamental frequency and are mainly used for stability and control design where high-frequency switching is not relevant.
- **Type 7 – Steady-state or load-flow models:** Provide the initial operating point for EMT studies, ensuring consistency with network power-flow results.

For wind turbines, these model types are applied to both DFIG converters and full back-to-back VSCs. Depending on the required simulation detail also full or half bridge models can be selected.

For PV systems, the inverter topology can highly impact the simulation cost as the number of controller models can escalate easily depending on the representation of the PV park.

As only minimal detail can be considered using the LF model and the Phasor model (type 6 and 7), only EMT tools get to correctly represent the behavior of the IBR sources. However, for IBR in EMT simulations, these detailed models involve a large number of state variables that must all be correctly initialized to represent a specific, desired operating point of the power system. Failure to do so leads to the significant problems discussed in the next section.

1.1.3 Hierarchical Control Structure of IBR sources

At the converter, IBR control systems are typically organized in hierarchical layers that ensure stable and coordinated operation from the device to the park. Although several architectures exist (e.g., model predictive, direct power, or droop-based control), this research focuses on the cascaded control structure, as it provides a clear separation between fast electrical dynamics and slower system-level objectives, making it the most widely used scheme for wind and PV systems [38]-[39].

The hierarchy comprises five layers (from fastest to slowest dynamic response):

1. **Lower-Level Control:** Handles converter-internal dynamics and switching processes [36]. It includes:

- Modulation schemes such as Nearest Level Control (NLC), Phase-Shift PWM, and Phase-Disposition PWM to generate semiconductor switching pulses.
- Capacitor Balancing Algorithms (CBA) to maintain uniform submodule voltages.
- Circulating Current Suppression (CCS) to minimize negative-sequence or DC-offset currents between converter arms.

2. **Inner Current Control:** Regulates the converter output currents in the d–q reference frame, ensuring fast decoupled control of active and reactive power. It operates at the highest control bandwidth and interfaces directly with the converter model.
3. **Outer Voltage Control:** Governs power, DC-link voltage, and AC voltage/frequency regulation. Depending on the converter type, it implements P/Q, Vdc/Vac, or V/f control

modes, generating current references for the inner loop. This layer ensures compliance with grid codes and overall energy dispatch objectives.

4. **Input Control Layer:** Connects the converter to the primary energy source. In wind parks, it performs the Maximum Power Point Tracking (MPPT) or torque control through the generator-side converter. In PV systems, it regulates the DC-DC converter to track the optimal voltage/current of the solar array. This layer determines the instantaneous power available to the DC link.

5. **Park Control Layer:** Supervises and coordinates the operation of multiple converters within a wind or PV park. It distributes setpoints (active/reactive power, voltage, frequency) among units, enforces limits on ramp rates or power factor, and ensures compliance with grid-code requirements during faults. Park controllers typically communicate with the Grid-Side Converter (GSC) controls via a supervisory or SCADA layer.

An example of the structure of the control system can be seen in Figure 1.9, for the case of the DFIG model, that will be studied in detail in CHAPTER 4. Lower-level control in the RSC and GSC models (depends on the converter model). Inner Current Control, GSC and RSC dq-current control. Outer voltage control, GSC and RSC outer control layer, power and voltage control of the WT equivalent model. Input control layer, pitch control based on the mechanical model of the wind turbine model and MPPT function. Park control layer, wind park controller (WPC), setting the base frame for the wind park power, voltage and frequency operation point.

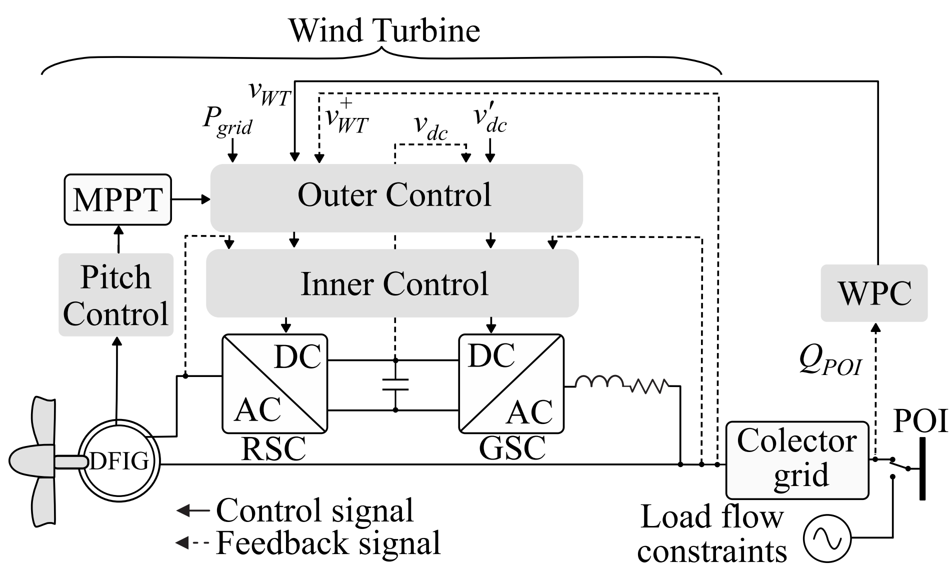

Figure 1.9 DFIG wind park model with LF initialization.

1.1.4 The Core Challenge: Initialization of EMT Simulations

The primary purpose of initialization is to begin the transient simulation from a stable state, thereby minimizing artificial transients that can corrupt or invalidate the study results [13]-[14]. The process for systems with IBR can be conceptualized in three stages:

1. **Load-Flow Simulation:** A load-flow (LF) is solved to determine the steady-state voltages, currents, and power injections at the point of interconnection (POI) for all components in the network. This establishes the target operating point for the entire system.
2. **State Reconstruction:** Based on the LF solution, a mathematical model is used to back-calculate the required internal initial states for each component. This includes the electrical states of converters and filters, as well as the mechanical states of prime movers.
3. **EMT Simulation Start:** The time-domain simulation begins with every component's state variables set with the calculated steady-state values, allowing the simulation to start smoothly.

Historically, the most common approach to bypassing this complex process has been the "run-up" or "brute-force" method [13], [40]. In this technique, the simulation is initiated from arbitrary initial conditions in many cases a "flat start" with zero voltage and current everywhere. It is allowed to run for a prolonged period until it reaches a steady-state. This method, while simple to implement, has severe drawbacks:

- **Prohibitive Computational Cost:** The run-up period can be extremely long, often hundreds of times longer than the actual transient event being studied. For large-scale networks, this makes EMT studies impractical.
- **Unwanted Transients:** The simulation start-up creates large, unrealistic electrical and mechanical transients that have no physical meaning. These transients can obscure the actual phenomenon of interest or, in worst-case scenarios, trigger protection models or prevent the system from initializing, leading to a collapse.
- **Uncertainty of Convergence:** There is no guarantee that the simulation will converge to the desired operating point. The simulation may collapse or settle at a state different from the intended load scenario, leading to incorrect study conclusions.

A robust and accurate initialization method is therefore not merely a convenience but a fundamental requirement for conducting efficient, reliable, and valid EMT studies in modern power systems.

1.1.5 State-of-the-Art in Power System Initialization

The development of accurate initialization methods has been an active area of research. The approaches vary significantly depending on the type of component being modeled, with a clear distinction between conventional power system elements and the more complex IBR.

1.1.5.1 Initialization of Conventional Components

The initialization of traditional power system components is a well-established and largely solved problem. For passive elements in sinusoidal steady-state, the initial inductor current and capacitor voltage are initialized to their instantaneous steady-state values. For synchronous machines, the internal states, such as the rotor angle (δ) and speed (ω), can be directly and analytically determined from the machine's terminal power, voltage, and current provided by a converged LF solution [41], [42]. These established methods provide a reliable foundation for initializing the non-IBR portions of a network.

1.1.5.2 Initialization Methods for IBR (White-Box Models)

The initialization of IBR is significantly more complex due to their internal control systems. For "white-box" models, where all internal control logic and parameters are known, the process follows the previously outlined three-stage framework, as shown in Figure 1.10.

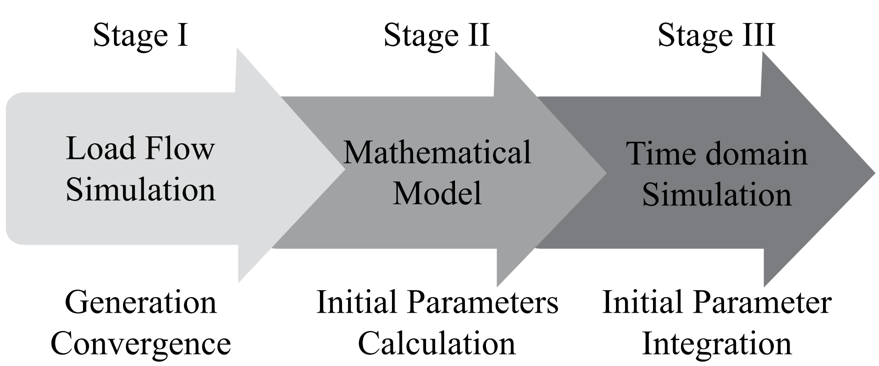

Figure 1.10 DFIG wind park model with LF initialization.

Stage I: Establishing the Network Operating Point via Load-Flow solution

The first step is to perform a LF simulation to define the system-wide operating point. While traditional LF methods, such as the Newton-Raphson method, are standard, they face challenges with modern networks that are unbalanced, multi-phase, and include nonlinear devices. To address this, advanced LF approaches have been developed.

For this research, the Modified Augmented Nodal Analysis (MANA) approach is of particular interest [42]-[44]. MANA is a derivative-based method that expands upon Kirchhoff's current nodal analysis by including supplementary equations and variables, method use in EMTP due to its speed, accuracy and ability to include non-linear components of the system. This allows it to robustly model the non-linearities inherent in IBR and other power electronic devices. Its main benefits include the ability to analyze multi-phase unbalanced systems and incorporate switching devices directly into the formulation. The MANA formulation results in a matrix system **Ax=b,** that once solve allows to find the steady-state (SS) conditions which is solve using a robust Newton method [42]-[44].

During this stage, the IBR themselves are typically represented by simplified models at their POI, such as a PQ bus (specifying active and reactive power) or a PV bus (specifying active power and voltage magnitude), to integrate them into the LF solution [13], [17], [45].

Stage II: Reconstructing the IBR Internal States

Once the LF has converged and the terminal conditions active and reactive powers (P,Q), and voltage magnitude V and its angle θ) at the IBR POI are known, the second stage is to back-calculate the initial values for all internal state variables of the IBR. This is a multi-faceted process that involves the mechanical, electrical, and control subsystems.

- **Mechanical and Aerodynamic Control:** For wind turbines, the mechanical power extracted from the wind must be consistent with the electrical power output. This requires initializing the aerodynamic control system. Based on the wind speed and the desired power output from the MPPT curve, the initial pitch angle (β) and tip-speed ratio (λ) are calculated to ensure the mechanical power equation is satisfied at steady-state [46]-[48].

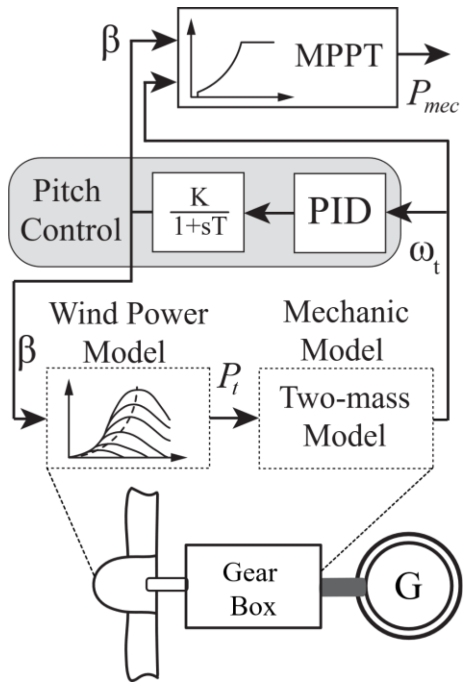

Figure 1.11 Mechanical model WP.

$$P_t = \frac{1}{2}\rho A v^3 C_P(\lambda,\beta) \tag{1.7}$$

$$C_P(\lambda,\beta) = \sum_{i=1}^{n}\sum_{j=1}^{n}\alpha_{ij}\lambda^i\beta^j \tag{1.8}$$

$$\lambda = \frac{\omega_t R}{v} \tag{1.9}$$

Where P_t is the mechanical power extracted from the wind (1.7), the ρ constant corresponds to the air density in kg/m^3, *A* in m^2 is the area swept by the turbine blades, *v* is the wind speed, and C_p is the power coefficient. The power coefficient is calculated as a function of the tip-speed ratio *λ* and the pitch angle of the blade *β*. Its value is calculated based on manufacturer data and fitted using comparison tables. For this research, the polynomial function of C_p, shown in (1.8) , is used. The tip-speed ratio is expressed as a function of the wind turbine speed ω_t in (rad/s), the blade radius *R* in *m*, and the wind speed in m/s

$$\frac{d\omega_r}{dt} = \frac{1}{2H_g}\left(k\theta_{tw} + c\frac{d\omega_r}{dt} - T_e\right) \tag{1.10}$$

$$\frac{d\omega_t}{dt} = \frac{1}{2H_t}\left(T_t - k\theta_{tw} - c\frac{d\omega_r}{dt}\right) \tag{1.11}$$

$$\frac{d\omega_{tw}}{dt} = \omega_b\left(\omega_t - \omega_r\right) \tag{1.12}$$

$$T_e = L_m\left(i_{qs}i_{dr} - i_{ds}i_{qr}\right) \tag{1.13}$$

The mechanical model is represented by a two-mass system, connected by a flexible shaft. The aerodynamic power P_m is converted to mechanical torque T_t. The torque transmitted through the flexible shaft, T_{sh}, is governed by the shaft stiffness K, and the damping coefficient D_{sh}, and it represents the dynamic coupling between the turbine and generator, controlled by the turbine and generator inertia H_t, and H_g respectively. The electric torque T_e is calculated based on the inductance of the machine L_m and the currents in the rotor (i_{dr}, i_{qr}) and stator (i_{ds}, i_{qs}), expressed in *dq*-frame for this particular scenario.

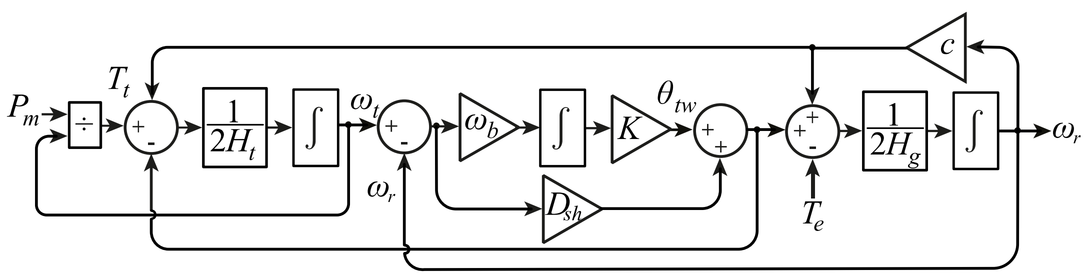

Figure 1.12 Two mass model.

The function of the wind speed control includes the power limit control and the speed control. To extract the maximum power from the wind, the turbine has an MPPT function that controls the pitch angle of the blades and the turbine's position inside the wind park. In Figure 1.13, the four regions of wind control are shown.

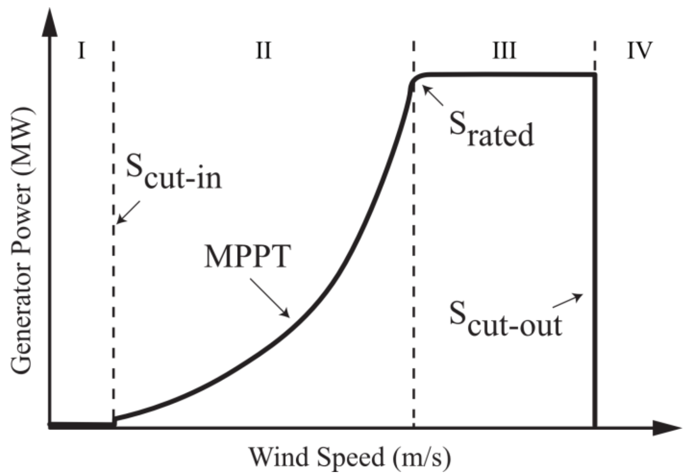

Figure 1.13 MPPT curve for the WP.

Three wind speed threshold points limit the four regions of the wind speed control. The cut-in speed, $S_{cut\text{-}in}$, is the minimum wind speed at which the wind turbine begins to generate power. After this point, the MPPT function control the power generation of the wind turbine. When the nominal speed of the wind turbine (S_{rated}) is reached, the production of power stabilizes at its rated value. Finally, $S_{cut\text{-}out}$ is the cut-out speed at which the turbine stops working to protect itself.

$$k_{opt} = \frac{1}{2} C_{P\max} \rho A \tag{1.14}$$

$$P_{opt} = P_{mec} = K_{opt} \omega_t^3 = K_{opt} \left(1 - s\right)^3 \tag{1.15}$$

The power extracted by the turbine in the MPPT curve shown in Figure 1.13 is calculated as a slip (s) function as shown in equations (1.14) and (1.15). P_{opt} is the optimal mechanical power P_{mec}, and K_{opt} is the optimal constant calculated from the mechanical coefficients explained in (1.7)

- **Machine and Converter Control:** The core of the initialization lies in setting the initial states of the fast internal controllers of the IBR. For a DFIG or FSC wind turbine, this involves initializing the Field-Oriented Control (FOC) scheme for both the GSC and RSC as shown in Figure 1.9. Knowing the desired active and reactive powers, one can solve the steady-state versions of the controller equations to find the initial values for all PI controller integrator states and the required dq-reference currents [46]. A similar process applies to

PV systems, where the outer voltage and power control loops and inner current control loops must be initialized to match the LF solution [48]-[49].

- **Phase-Locked Loop (PLL) Initialization:** The PLL is a critical component that synchronizes the IBR to the grid. Its internal state, the estimated grid angle (θ_{PLL}), must be initialized to match the actual grid angle from the LF solution at the POI. For a standard Synchronous Reference Frame PLL (SRF-PLL), this is straightforward in balanced systems. However, for unbalanced conditions or weak grids, more advanced PLLs, such as the decoupled double SRF-PLL or the dual second-order generalized integrator FLL (DSOGI-FLL), are used, which require more complex initialization to account for positive and negative sequence components [50]-[52].

Stage III: Time-domain Simulation

The final step is to set the calculated initial conditions of all components identified in the previous stage. The calculated states of the back-to-back converter controllers, mechanical drive system, induction machine, and electrical converters are applied to initialize the system, improving the transition into the time-domain simulation.

1.1.5.3 The Complication of Proprietary IBR Models

The method described above is highly effective for "white-box" models. However, in real-world engineering studies, IBR models are often provided by manufacturers as "black-box" or "grey-box" components [53].

- **Black-Box Models:** These are compiled, encrypted libraries where the user has no access to the internal control structure, equations, or parameters. The model is an opaque block that processes inputs and produces outputs.
- **Grey-Box Models:** These models offer partial information. For example, the general control topology might be known, but key parameters or specific non-linear functions remain hidden.

For these proprietary models, the full initialization methods discussed in Chapters 2-4 cannot be applied directly. The equations needed to back-calculate the internal states are not available. This creates a significant bottleneck, forcing engineers to revert to less efficient methods for a large and growing class of critical grid components. The literature contains very few systematic approaches to address this specific challenge, representing a significant gap in the current state of the art, and a proposed solution is described in more detail in chapter 5.

1.1.6 Identification of Research Gaps and Dissertation Objectives

There is a notable scarcity of literature addressing this specific challenge. The state of the art reveals two critical gaps in the current practice of EMT simulation. First, while methods exist for initializing white-box IBR models, there is a need for a more unified, automated, and robust framework that can handle large-scale, unbalanced systems in a modular and computationally efficient manner. Second, and more critically, there is a profound lack of effective initialization methodologies for the proprietary black-box and grey-box IBR models that are increasingly prevalent in industry. This practical challenge forces engineers to rely on slower methods, hindering the efficient study of modern power grids.

This dissertation directly addresses these gaps. The primary objective of this research is to improve and automate the initialization of converter-interfaced resources, by developing a modular and generalized framework. The specific objectives are:

- To improve the initialization of IBR models based on LF results through detailed mathematical modelling and the consideration of their respective control model restrictions.
- To develop fast and automated initialization techniques for a range of IBRs, including Type 3 and Type 4 wind turbines and photovoltaic parks.
- To define a general methodology for the automatic initialization of limited access converter-controlled components, allowing for the easy integration of future technologies and control schemes.

To achieve these objectives, this dissertation proposes a comprehensive three-stage initialization framework that systematically drives large-scale EMT models to their correct steady-state operating point. Furthermore, a novel hybrid initialization methodology is explicitly introduced for grey-box and black-box models. This hybrid approach fuses external LF data with limited variables to estimate the IBR internal state, thereby extending the benefits of accurate initialization to proprietary models.

The successful implementation of these methodologies is expected to have a significant impact on the field. By aligning the time-domain model with the converged LF solution, the proposed framework will drastically reduce the computational cost of EMT studies, suppress incorrect start-up transients that can lead to faulty protection tripping or mask underlying phenomena, and ultimately improve the reliability of power system simulations.

1.2. Motivation

The global power system is undergoing a historic transition. By 2025, variable renewable energy sources, such as wind and solar, will have grown from marginal contributors to fundamental pillars of the global electricity supply, together meeting approximately 15% of global demand. In many countries, their contribution is even more profound, with instantaneous penetration levels that often require the grid to operate almost entirely on IBR for prolonged periods. This paradigm shift demands that IBR evolve from passive generators into active participants, providing essential grid services such as frequency response, reactive power regulation, and fault ride-through capabilities.

To ensure grid stability and reliability in this new reality, power system engineers depend on high-fidelity EMT simulations. These studies are indispensable for understanding the complex, high-frequency interactions between advanced converter controls and the wider network. However, the practical utility of these essential simulations is severely impacted by a fundamental and persistent challenge: initialization.

As this literature review has established, accurately initializing a large-scale EMT model is a complex task. The conventional "run-up" method is computationally prohibitive and introduces non-physical transients that can corrupt study results. While systematic methods have been developed for traditional "white-box" models where all parameters are known, two critical gaps remain.

This research aims to improve, automate, and generalize the initialization of converter-interfaced resources, making large-scale EMT simulation a more efficient tool. By developing a comprehensive three-stage framework for white-box models and a novel hybrid methodology for proprietary models, this work provides a systematic solution to the initialization problem. The goal is to reduce the computational cost of vital grid studies and improve their accuracy where renewable energy is no longer the alternative, but the norm.

1.3. Contributions

The primary contribution of this dissertation is the development of a generalized and modular framework for the time-domain initialization of IBR in EMT simulations. By addressing the limitations of existing partial initialization methods, this research provides a mathematical and practical solution that ensures simulations start as close as possible to the operating point derived from the load-flow solution.

The specific contributions of this work are:

- **Development of the Full Control Initialization (FCI) Method for PV and FSC Wind Parks:** This thesis introduces the FCI methodology, a robust procedure that reconstructs the internal state variables of "white-box" models. Unlike previous existing techniques that only initialize terminal constraints, FCI back-calculates steady-state conditions for the entire control hierarchy, including PLL, inner current loops, outer voltage/power loops, and mechanical subsystems. This eliminates the need for time-domain pre-initialization, removing artificial start-up transients.
- **Unified Initialization of DFIG Models:** The research extends the initialization framework to DFIG wind parks, which present unique challenges due to the coupling between the stator, rotor, and the back-to-back converter. The proposed method solves the algebraic coupling of the induction machine and the converter bridge simultaneously, initializing the mechanical torque, rotor speed, and flux linkages at the same time of the electrical controls. This ensures faster initialization in detailed EMT simulations where slight initialization errors can lead to undesired transients.
- **A Novel Hybrid Initialization for Proprietary (Black-Box) Models:** Addressing a critical gap in industrial applications, this dissertation proposes the Hybrid Decoupling Interface (HDI) method for initializing "grey-box" and "black-box" models where internal control logic is inaccessible. By combining external decoupling interfaces with partial steady-state estimation of accessible control inputs, this method allows proprietary models to settle rapidly without requiring access to the manufacturer's source code.
- **Significant Reduction in Computational Cost for Large-Scale Grids:** The implementation of these methods demonstrates drastic reductions in simulation time.

Validated against multiple benchmarks, the proposed framework achieves up to 92% reduction for initialization processes compared to existing methods. This efficiency enables the practical use of high-detail generators EMT models for large-scale renewable integration studies.

1.4. Publications

1. J. A. Ocampo-Wilches, A. Ramirez, K. Jacobs, J. Mahseredjian and A. G. Pavani, "Full-Control Initialization of Photovoltaic Park Models for Electromagnetic Transient Simulations," IECON 2024 - 50th Annual Conference of the IEEE Industrial Electronics Society, Chicago, IL, USA, 2024, pp. 1-8, doi: 10.1109/IECON55916.2024.10905292.
2. J. A. Ocampo-Wilches, J. Mahseredjian, K. Jacobs, A. G. Pavani and H. Xue, "Comprehensive Full-Scale Converter Wind Park Initialization for Electromagnetic Transient Studies," in IEEE Transactions on Power Delivery, doi: 10.1109/TPWRD.2025.3551546.
3. J. Mahseredjian , M. Naidjate, Mehdi Ouafi and J. A. Ocampo-Wilches " Electromagnetic Transients Simulation Program: A unified simulation environment for power system engineers, " in IEEE Electrification Magazine, vol. 11, no. 4, pp. 69-78, Dec. 2023, doi: 10.1109/MELE.2023.3320511.
4. J. A. Ocampo-Wilches, A. G. Pavani and J. Mahseredjian " Detailed Control DFIG Wind Farm Initialization for Electromagnetic Transient Modeling," accepted to XXIV Power Systems Computation Conference (PSCC) 2026, 08-12 June 2026.
5. A. Allabadi, J. A. Ocampo-Wilches, J. Mahseredjian " A Novel Hybrid Initialization Method for DFIG Wind Park Simulation Models," submitted to IEEE Transactions on Power Delivery.

1.5. Thesis outline

Chapter 2 – Initialization of Photovoltaic Park Models for EMT Simulations develops a staged procedure for PV park initialization. The chapter details the PV generator model, VSC representation, park-level control architecture, and aggregation of linear components. The three-stage method is presented for PVs. Finally, the method is validated on systems ranging from a single aggregated PV park to the IEEE 34-bus feeder, and its accuracy and computational performance are compared against existing approaches.

Chapter 3 – Initialization of Full-Scale Converter Wind Park for EMT Studies extends the staged methodology to FSC wind parks. Two complementary schemes are formulated: a load-flow and source initialization (LFSI) baseline and a Full-Control Initialization (FCI) that sets both grid-side and machine-side converters with control-consistent states. Mechanical subsystem initialization is included to ensure torque-speed consistency. The methods are compared on aggregated, detailed, and large-scale test systems, demonstrating reductions in settling time and computational cost while maintaining stability.

Chapter 4 – Initialization of DFIG Wind Parks for EMT Modeling tackles initialization for Type-3 wind parks. The FCI scheme is designed to consistently set the wind-park controller (WPC), RSC, GSC, PLL, DC link, and mechanical states. The procedure combines operating-point reconstruction with targeted time-domain simulation and is validated on aggregated, detailed, and transmission-feeder test cases.

Chapter 5 – Initialization of Proprietary IBR Models: Grey- and Black-Box Approaches This chapter introduces two extensions tailored to industrial practice: a Decoupling-Interface (DI)–based initialization that reduces algebraic coupling during start-up, and a Black-Box Initialization scheme that reduces the required initialized components for proprietary IBR models when controller details are unavailable.

Chapter 6 – Conclusion synthesizes the main findings across PV, FSC, and DFIG technologies, emphasizing the generalizable elements of the proposed initialization framework and its impact on EMT study efficiency and robustness. It outlines future work, including simplified IBR models for fast simulation scenarios, parallel computing for improved simulation times, and broader treatment of proprietary models.

CHAPTER 2 INITIALIZATION OF PHOTOVOLTAIC PARK MODELS

The accurate initialization of photovoltaic (PV) park models is a fundamental step in EMT simulations. Correct initialization ensures that simulations start from a valid steady-state operating point consistent with the network's LF solution, thereby avoiding artificial transients, excessive computation times, or numerical instabilities.

Existing PV initialization methods can be broadly grouped into three categories [59].

1. **Phasor-domain methods** compute the steady-state solution at the nominal frequency but cannot accurately represent nonlinear converter dynamics or complex control interactions.
2. **EMT-based methods**, formulated as backward-forward iterative methods, offer detailed dynamic fidelity but suffer from high computational costs, poor convergence, and, at times, inaccurate steady-state solutions [54]-[57].
3. **Load-flow-based methods**, such as the Load-Flow and Source Initialization (LFSI) implemented in EMTP [58]. In this technique, during the initialization, the WP is disconnected from the power grid and temporarily connected to an ideal voltage source for a preset time t_{init}, with magnitude and angle values found from the LF solution, as shown in red in Figure 2.1. The general scheme for the LFSI is presented in Figure 2.1. The voltage source shown in blue connected to the power system, during the initialization, prevents the transients from the WP from propagating to the power system. Once the different controllers of the WP including the PV park Controller (PVPC), and the inner and outer control layers of the PV park reach steady state they are disconnected. The different components of the controllers will be described in the next subsection.

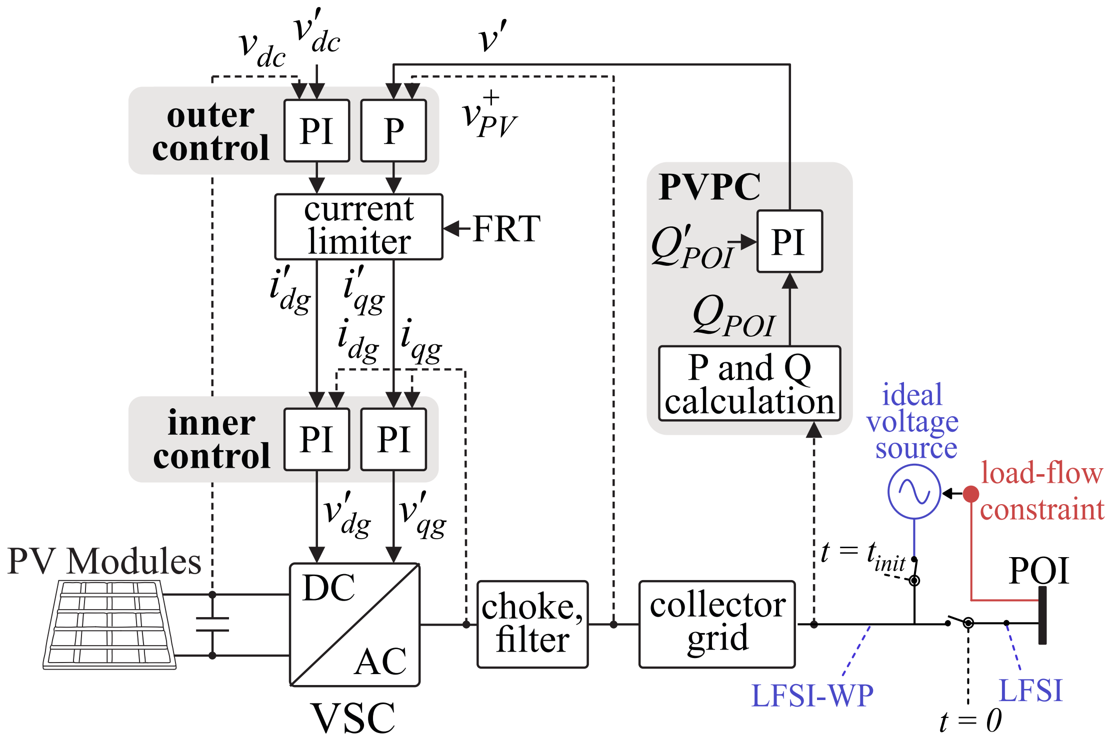

Figure 2.1 LFSI Initialization for PV parks.

This technique has proven reliable by mapping the LF solution into the time-domain model. LFSI initializes electrical quantities and key control systems such as the PLL but still requires a short time-domain run-up to initialize converter control states, during which the PV park is disconnected from the grid. This step introduces unnecessary initialization transients and increases computational effort.

To overcome these limitations, this chapter develops a Full Control Initialization (FCI) procedure tailored to PV park models. The proposed method builds from the LF-based initialization but extends it by fully reconstructing the internal states of the converter and control systems, thereby eliminating the need for time-domain pre-initialization. This approach reduces computational cost, improves accuracy, and ensures that EMT simulations start directly from the desired steady-state operating point.

2.1 Park Model

The generic model of the PV park, adopted from [10], [58], is depicted in Figure 2.2. It has five primary components: a) the equivalent electric circuit of the PV modules, which incorporates parameters from commercial datasheets [59]; b) the DC-AC voltage sourced converter (VSC) that change its detail based on the requirements of the simulation; c) its controls including an outer layer where the dc voltage of the PV modules V_{dc} and the voltage at the entry of the park V_{PV}^{+} are controlled, using the references V_{dc}' and the output of the PVPC v'; d) the PVPC, responsible for governing the reactive power at the POI Q_{POI}, and controlling it based on a reference Q_{POI}', and e) the PV park aggregated electrical components, which include the representation of the filters, the transformers, and the equivalent collector grid.

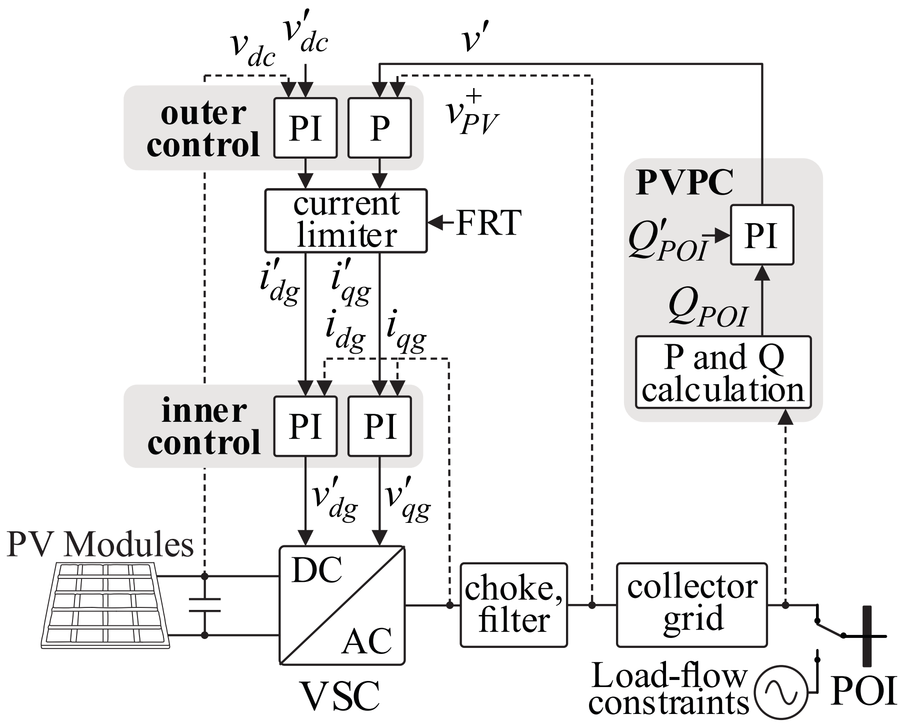

Figure 2.2 Aggregated PV Park model.

2.1.1 Photovoltaic Generator's Model

The single-diode model is adopted in this thesis for the PV cell modeling, which meets most EMT simulations' requirements [61].

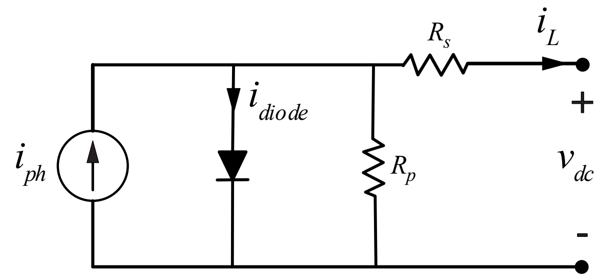

Figure 2.3 The equivalent circuit of the PV cell is used for modeling the PV generator.

Figure 2.3 presents the electric circuit of the PV cell corresponding to the adopted single-diode model. Its output current i_L is given by

$$i_L = i_{ph} - i_{diode} - \frac{v_{dc} + i_L R_s}{R_p} \tag{2.1}$$

Where i_{ph} is the dependent current source, i_{diode} the current across the diode, v_{dc} the voltage at the connection point, and R_s and R_p the series and parallel equivalent resistances, as shown in Figure 2.3. The parameters of this model account for several modules connected in series and parallel, as well as temperature and irradiance.

2.1.2 VSC Modeling

This chapter presents the initialization of two types of VSC models. The AVM and the DM can be used for different types of studies. The AVM and DM models are shown in Figure 2.4, where v_{dc} is the output voltage of the PV array model (see Figure 2.3). The initialization method is explained in section 2.2. The numerical comparisons between AVM and DM are presented in section 2.3.

2.1.3 PV Park Controller

The PVPC establishes the external voltage and reactive power setpoints for the outer control of the VSC, as shown in Figure 2.2. The VSC governs the output of reactive power and DC bridge voltage [62], while active power regulation is defined by the current delivered by the PV modules, which depends on the irradiance and the diode current [60]. The PVPC mode can be selected based on the grid requirements, with the three most common modes being reactive power control (Q-mode), voltage control (V-mode), and power factor control (PF-mode) [63], [64]. Additionally, the PVPC employs a PLL to monitor the voltage and frequency of the grid, ensuring compliance with the LF constraints.

2.1.4 Aggregation of Linear Components

In the proposed method, the linear electrical components within the PV park, including lines, cables, and transformers, are represented by an aggregated model [64], [65]. The computational advantages of using an aggregated model instead of detailed components are demonstrated in Section IV.

2.2 PV Park Initialization

The backbone of the new method named Full Control Initialization (FCI) consists of initialization of the integral blocks for every PI controller based on the values of power, voltage, and current at the POI provided by the LF solution. This results in a correct current and voltage reference at the first time-step, reducing initialization transients. In the following, the initial value for the integrator blocks is referred to as the history term, H . Since a steady-state is assumed, all time derivatives are set to zero [66] to calculate the initial conditions.

The proposed initialization procedure comprises the following three stages.

- Stage I: The PV parks are modeled as LF buses, and a multi-phase LF analysis is conducted using the MANA approach [44]. This provides steady-state voltage, current, and power values at the POI.
- Stage II: According to the LF results, the steady-state outputs of PVPC, inner and outer converter control, and the measuring components are calculated using analytical equations. The computed values are then used to initialize the system. Further details on the initialization of PVPC and VSC controllers are provided in subsections 2.2.1 to 2.2.3.
- Stage III: The time-domain simulation is started with the initialized controller parameters. The following procedure is applied to further match the voltage value at the converter terminals. As the measurement of the converter will impact the behavior of the controllers after the initialization point, it is needed to also fix the initial condition in the converter itself. To do so, for the first simulation point, i.e. $t = 0$, an ideal voltage source is connected in parallel to set either the AVM's or DM's initial angle and magnitude calculated from the LF solution. The ideal voltage sources for AVM and DM are depicted in blue in Figure 2.4.

The source is disconnected at the next time-point Δt. With this procedure, the output measurement that will be use by the controllers will be set correctly to its correct operation point.

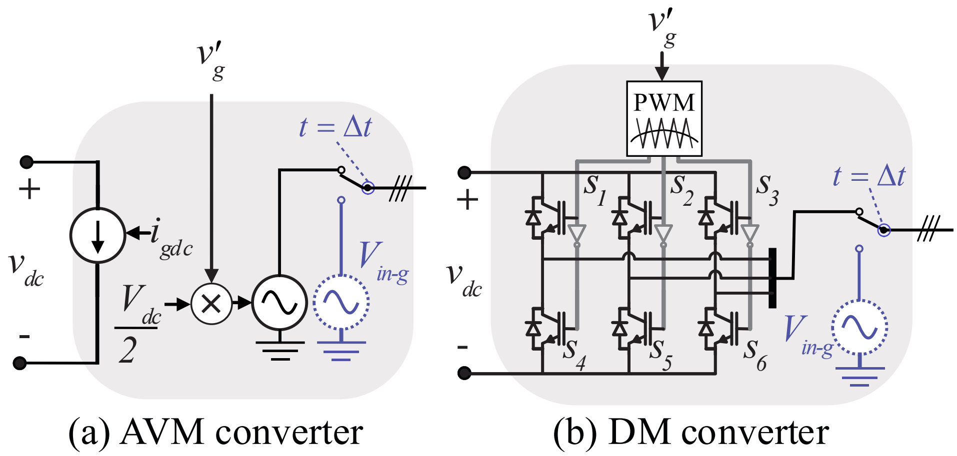

Figure 2.4 VSC Initialization for AVM and DM.

2.2.1 PVPC Initialization

The control mechanism for the reactive power of the PV park is based on the secondary voltage control concept [67]. The corresponding diagram is shown in Figure 2.5. At the primary level (right-hand-side in Figure 2.5), the VSC controller controls the positive sequence terminal voltage, v_{PV}^{+}, through a proportional voltage controller. At the secondary level, the PVPC monitors the reactive power at the POI (left-hand-side in Figure 2.5), Q_{POI}, and performs its control by adjusting the reference voltage values v' of the PV inverter. The apostrophe symbol denotes the reference values. The history term H_Q of the corresponding PI controller is calculated as

$$H_Q = \frac{\Delta v'}{k_i} \tag{2.2}$$

$$\Delta v' = \left(\frac{i'_{qg}}{k_p} \right) + v_{PV}^{+} - 1 \tag{2.3}$$

The reference current i'_{qg} corresponds to the measured steady-state current from the choke filter. At the same time, the positive sequence voltage v^{+}_{PV} is equal to the measured voltage at the harmonic filter, as shown in Figure 2.2.

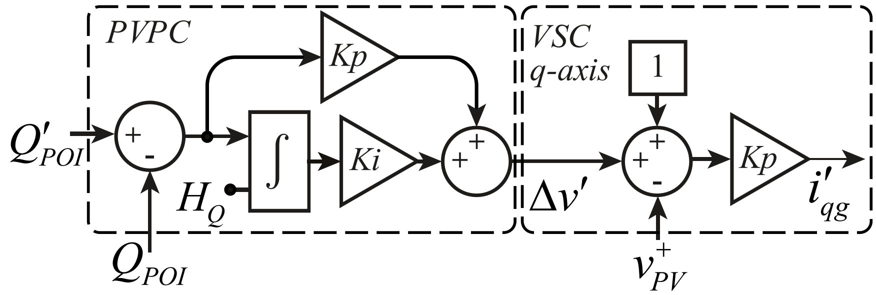

Figure 2.5 Control diagram of the PVPC and VSC outer control q-axis, including the initialization with the history term H_Q.

2.2.2 VSC Outer v_{dc} Control Initialization

Under stable operational conditions, the power generated by the PV array matches the power delivered to the grid, while the DC-link voltage corresponds to its predetermined nominal level. Consequently, the history term of the integrator of the PI- controller can be determined from the dq-frame transformed three-phase currents (i_{dg} and i_{qg}) at the VSC. The block diagram shown in Figure 2.6 depicts the architecture comprising the v_{dc} outer control loop and the d-axis inner control loop. The history term $H_{v_{dc}}$ is given by

$$H_{v_{dc}} = i'_{dg} / k_i \qquad (2.4)$$

where k_i is defined based on the DC-link, as detailed in [10].

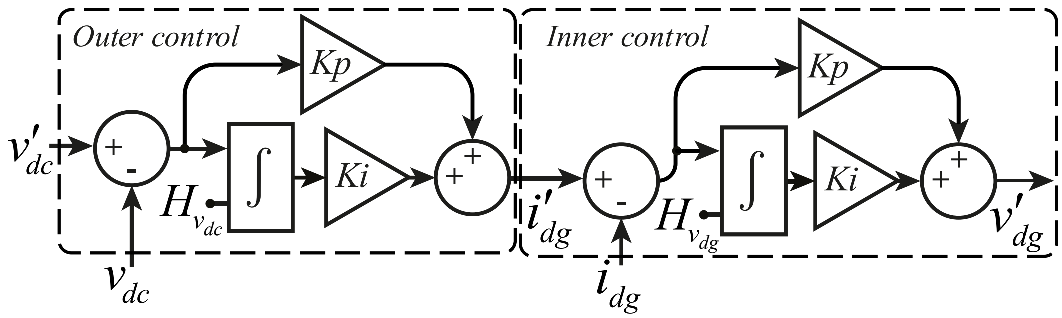

Figure 2.6 Control diagram of the VSC d-axis, including the initialization with the history terms $H_{v_{dc}}$ and $H_{v_{dg}}$.

2.2.3 VSC Inner current control initialization

The inner current control system provides the VSC dq-frame voltage reference, as shown in Figure 2.7. For the VSC, the history terms for the PI-controller within the d-axis and q-axis inner control loop are computed by

$$H_{v_{dg}} = v'_{dg} / k_i \tag{2.5}$$

$$H_{v_{qg}} = v'_{qg} / k_i \tag{2.6}$$

$$v'_{dg} = v_{dg} + \omega L_{choke} i_{qg} - v_{d-ref} \tag{2.7}$$

$$v'_{qg} = v_{qg} - \omega L_{choke} i_{dg} - v_{q-ref} \tag{2.8}$$

where v_{dg}, v_{qg} and i_{dg}, i_{qg} represent the dq-frame steady-state voltage and current measured at the choke terminals (see Figure 2.2). L_{choke} denotes the inductance of the choke filter, while ω stands for the nominal angular frequency. Additionally, v_{d-ref} and v_{q-ref} represents the reference voltage value in the dq-frame obtained from the LF solution.

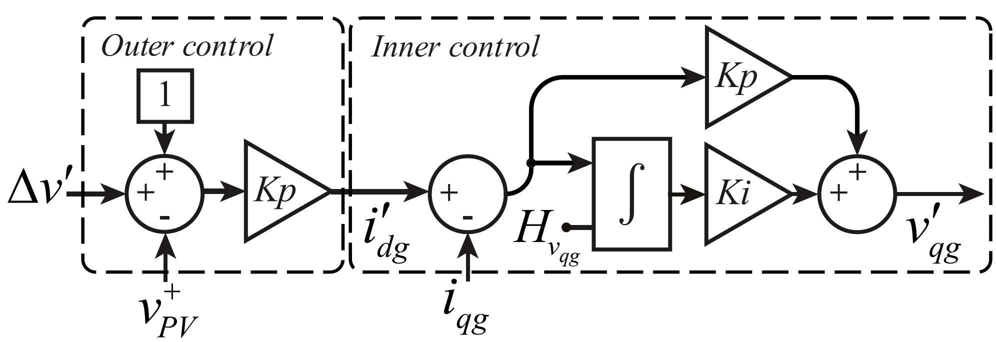

Figure 2.7 Control diagram of the VSC q-axis, including the initialization with the history term

$H_{v_{qg}}$.

2.2.4 Phase-Locked Loop Initialization

An accurate grid phase angle is required to determine the grid voltage phase angle and frequency in grid-connected power converters. For this case, a synchronous reference frame PLL, shown in [50], provides the continuous measure of the phase-angle and the fundamental voltage frequency. The accuracy of the PLL is crucial for implementing vector-based controllers [49].

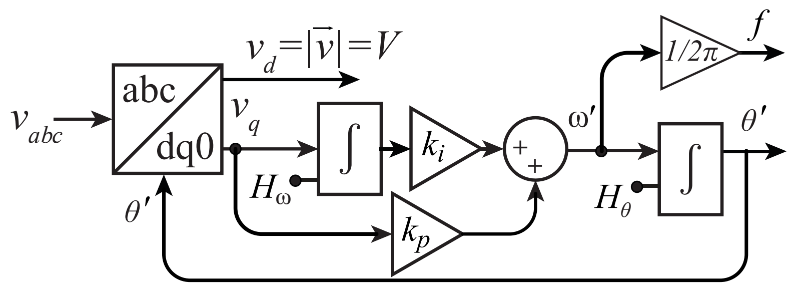

Figure 2.8 Control diagram of the PLL including initialization with history terms H_ω and H_θ .

To initialize the integrators of the PLL, the history terms of the angular frequency and the phase angle, H_ω and H_θ are calculated by

$$H_\omega = \frac{\omega}{k_i} \tag{2.9}$$

$$H_\theta = tan^{-1}\left(\frac{v_\beta}{v_\alpha}\right), \tag{2.10}$$

where ω is the nominal angular velocity, k_i the PLL integral constant magnitude, v_α and v_β are the $\alpha\beta$ -frame components of the calculated voltage.

2.3 Comparison of PV Park Initialization

This section compares the proposed FCI with the existing LFSI method. The latter use a temporary ideal source connected to the grid to emulate an ideal PV park during a simulation time until initialization transients die out. This prevents the park-internal transients from perturbing the power system and from creating undesirable control interactions with other grid-connected converters. The LFSI is complemented by initializing the PLL measurement blocks using LF results. The FCI is a comprehensive initialization of all controllers and voltage initialization of the inverter, as described in section 2.2 both initialization methods, LFSI and FCI, are compared using the AVM or the DM for the converter.

In the following, three types of power systems are simulated to verify the efficacy of the proposed initialization technique:

- Test case 1) Small-scale system, aggregated PV park model.
- Test case 2) Small-scale system, detailed PV park model.
- Test case 3) Large-scale system, 14 aggregated PV park models.

Aggregated models condense multiple PV arrays, their converters, and their collector grids into lumped components. In contrast, the detailed PV park model (test case 2) simulates each distinct PV array, their converter, and their individual collector lines. The simulations presented in the following use a time-step of 50 μs for the AVM and 1 μs for the DM to guarantee numerical convergence in the cases where CP lines where included. It will be considered in steady-state condition when the waveform variations are within a tolerance band of 1% of the convergence value. All simulations are performed in the EMTP® software [58], using an Intel i7-8550U 1.80 GHz processor.

2.3.1 Test Case 1: 120 kV System with Aggregated PV Park Model

The 120 kV/60 Hz EPRI benchmark system with one PV park is simulated to evaluate the impact of individual PV park initialization. The topology of this system is presented in Figure 2.9, including five transmission lines modelled as PI lines, two loads and a connection to an infinite bus source [68]. For this case scenario, the PV park, it is configured in PQ control mode for the LF, and both the AVM and DM representation of the converter are studied in the results.

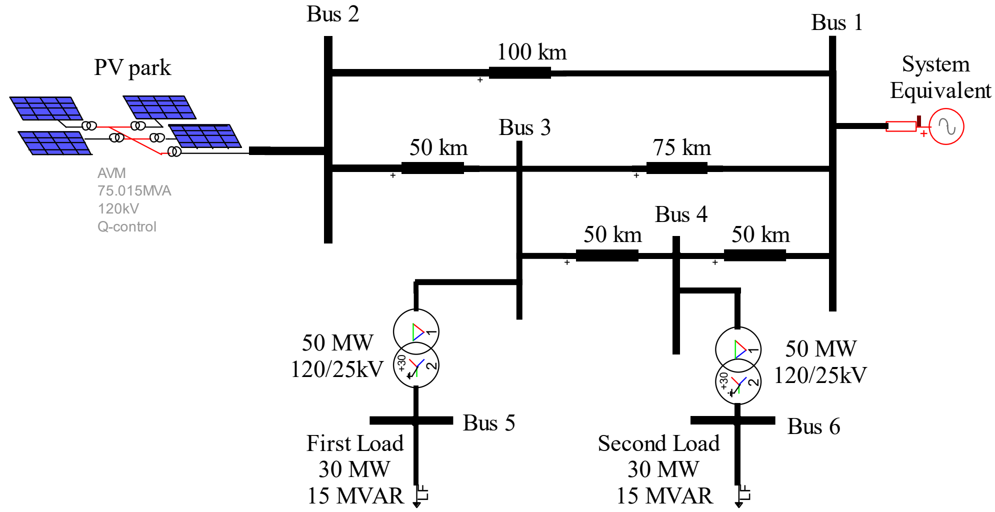

Figure 2.9 Test case 1, EPRI benchmark with aggregated PV park.

Figure 2.10 presents the active and reactive powers at the POI for the time-domain simulation of the system if no steady-state initialization is applied. The time required to reach steady-state by the AVM and DM is 0.22 s and 0.21 s, respectively. In terms of EMT simulation, this represents a long time exhibiting transient behavior in the waveforms.

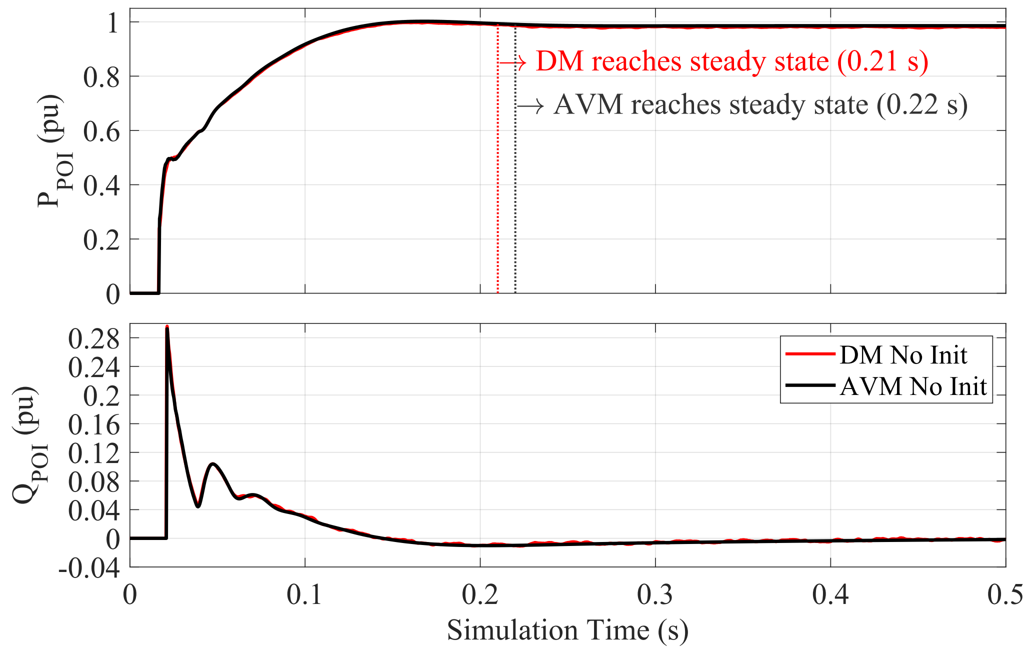

Figure 2.10 Test case 1, Average active and reactive powers at the POI for AVM and DM converters with no controllers initialization.

Figure 2.11 and Figure 2.12 present the average active and reactive powers at the POI for the time-domain initialization of the system. LFSI and FCI initialization methods are applied. The corresponding powers at the POI are presented for the AVM and DM.

Error! Reference source not found. compares the time to reach the steady-state within the simulation time window and the computation time required to reach the steady-state.

In Figure 2.11 and Figure 2.12 the LFSI internal behavior of the PV park is included for AVM and DM LFSI-PV, respectively. The switching time of the ideal source is chosen to reconnect the PV park once the transient is reduced, as can be seen at 0.12 s for test case 1. The transient associated with LFSI-PV is considerably more significant than the FCI, making the ideal source critical in maintaining the output power within the required margins. There is a small variation in the behavior of the FCI but it is maintain under the 1% limit specified as margin for consider it in steady state, this is due to the differences between the calculated value from the LF and the calculated backward propagated condition.

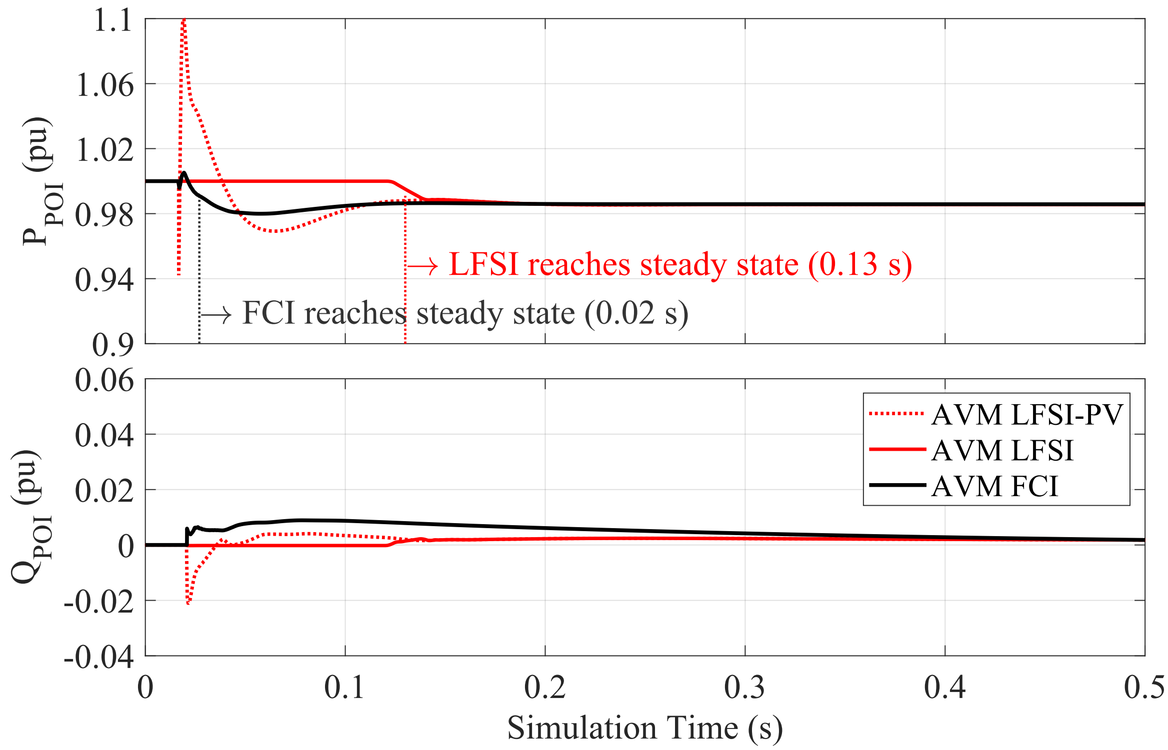

Figure 2.11 Average active and reactive powers at the POI, as given by FCI and LFSI initializations and using converter AVM for test case 1.

The results in **Error! Reference source not found.** show that, even for a comparably simple simulation case, the computational savings by the FCI approach are substantial, achieving gains of around 6 and 3 for AVM and DM, respectively. However, looking at the absolute time savings, it becomes evident that a significant benefit for AVM simulations is not achieved unless very large parametric studies are conducted. For DM simulations, the savings are notable as the reduced time step increase the computational time and the total initialization time will be more considerable. In the same manner as in the AVM model, the internal behavior of the PV park LFSI-PV is connected to the LFSI point after the transient is cleared, causing a delay to reach steady state.

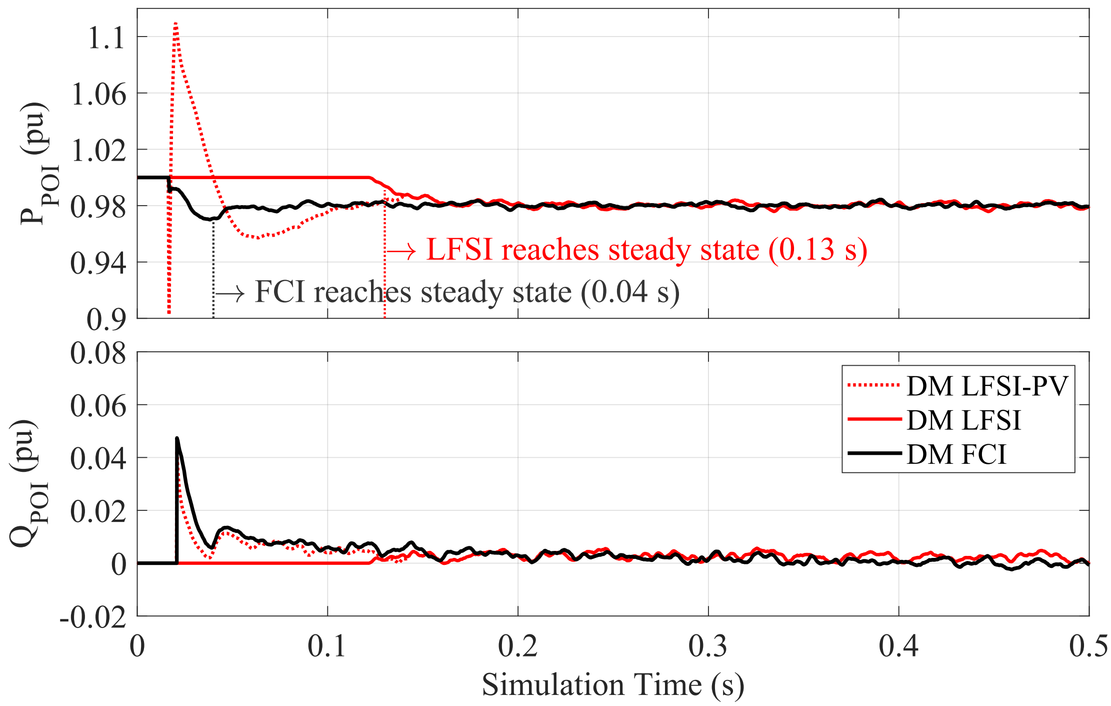

Figure 2.12 Average active and reactive powers at the POI, as given by FCI and LFSI initializations and using converter DM for test case 1.

Table 2.1 Simulation data for test case 1

Converter	Initialization method	Initialization time (s)	Computation time (s)
AVM	LFSI	0.13	1.03
	FCI	0.02	0.54
DM	LFSI	0.13	34.36
	FCI	0.04	12.53

2.3.2 Test Case 2: 120 kV System With Detailed PV Park Model

As an extension of the previous initialized case, a detailed representation of the PV park of subsection 2.3.1, is studied in this test case. The PV Park comprises 45 individual PV arrays, each connected to the transformer at a distinct distance. These PV arrays are grouped into three distinct feeders, each comprising eighteen, twelve, and fifteen PV arrays, respectively. The overall system layout is presented in Figure 2.13, while the internal connections of feeder one are showcased in

Figure 2.14. The three feeders are connected in parallel, followed by the PV park transformer. The interconnection of the PV park to the grid is the same one presented in test case 1.

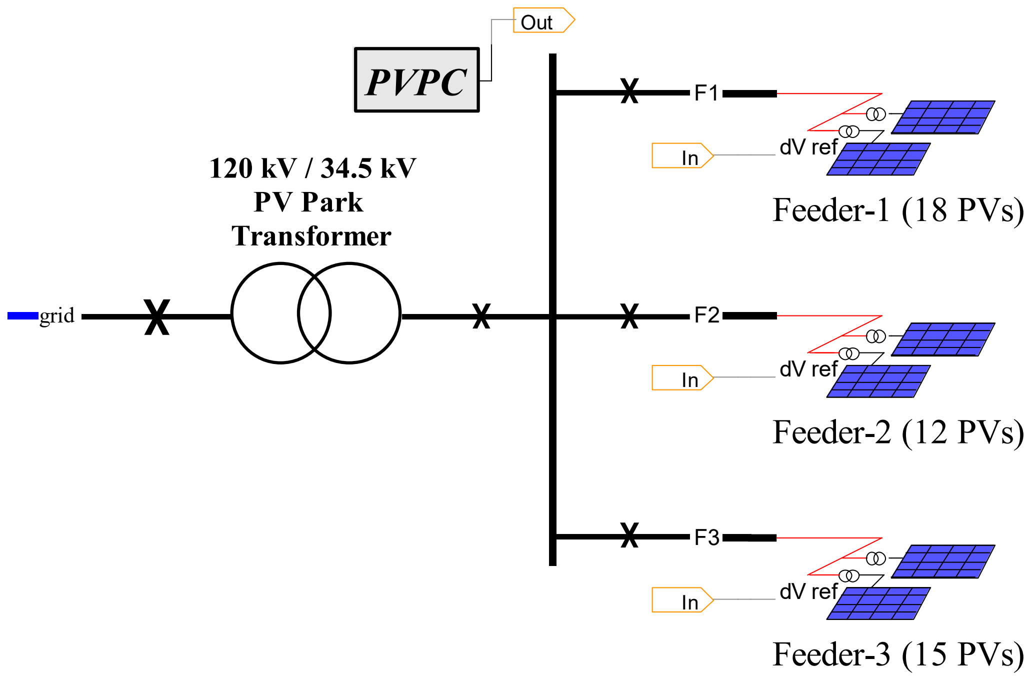

Figure 2.13 Test case 2, detailed PV park with three feeder branches.

To analyze the behavior of the PV park in more detail, the active and reactive powers are studied at the entry of each of the three feeders, as presented in Figure 2.15 and Figure 2.16.

When the ideal sources are connected in the LFSI technique, the behavior of the internal LFSI-PV does not match the grid requirements perfectly, resulting in a transient at the switching instant that can be significant for the initialization, as shown in Figure 2.15 and Figure 2.16.

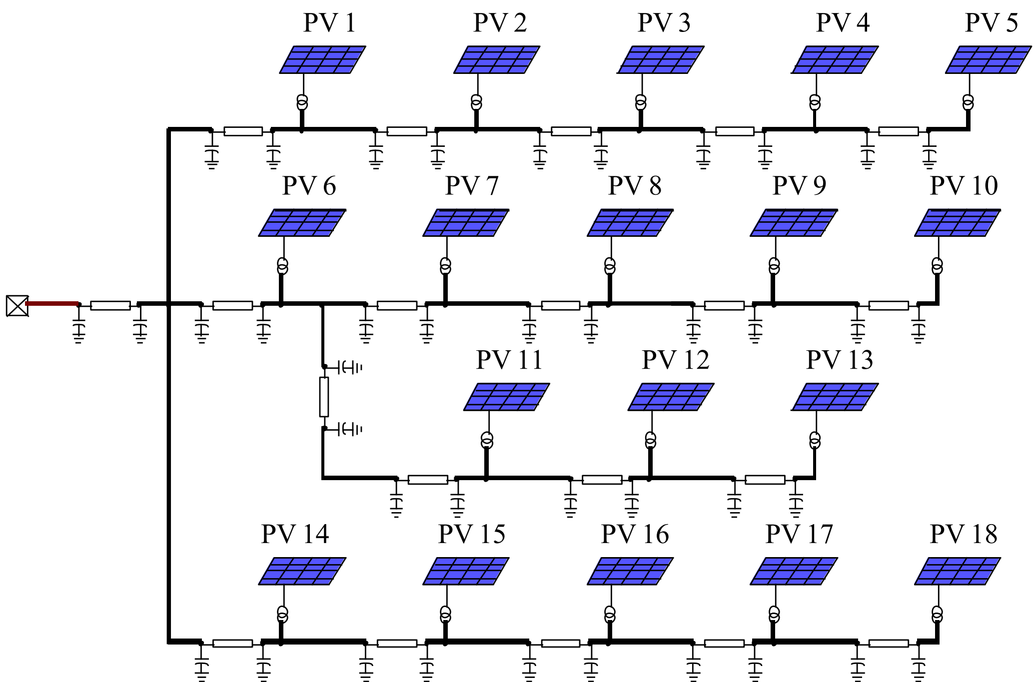

Figure 2.14 Test case 2, diagram of Feeder-1 with eighteen distinct PV arrays.

The simulation and computation times for test case 2 are listed in **Error! Reference source not found.**. These results demonstrate an increase in the simulation time to reach the steady-state, as expected.

Table 2.2 Simulation Data for Test Case 2

Converter	**Initialization method**	**Initialization time (s)**	**Computation time (s)**
AVM	LFSI	0.21	73.48
	FCI	0.02	34.13
DM	LFSI	0.21	5734.67
	FCI	0.04	1102.66

The FCI method effectively reduces the initial transients, as observed in Figure 2.15 and Figure 2.16. The results of **Error! Reference source not found.** show that the FCI method significantly reduces the initialization time. The difference in the steady-state value between AVM and DM can be attributed to the DM losses. The transient peak observed in the LFSI model is caused by the simultaneous switching of multiple independent PV array models at 0.2 seconds, which collectively delays the system from reaching steady-state. The FCI method directly resolves this issue because it does not require any switching during the initialization phase.

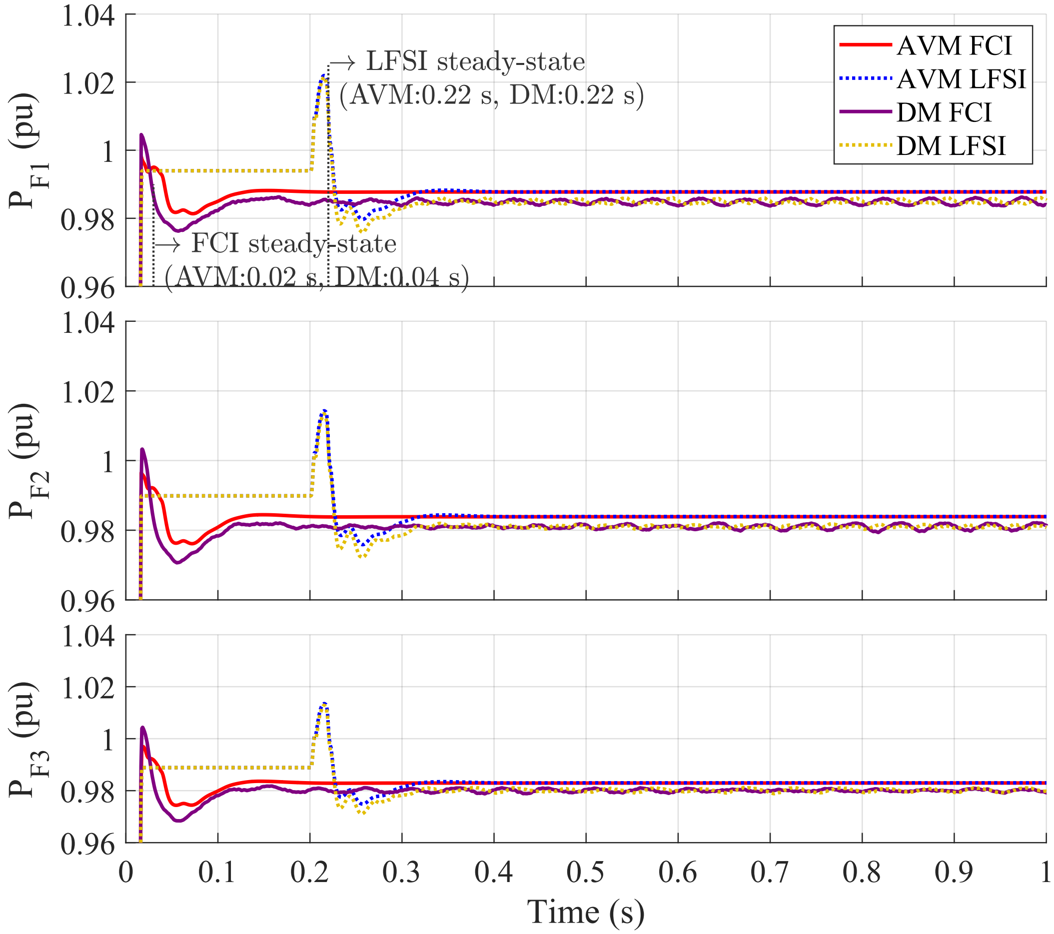

Figure 2.15 Average active power in feeder one to three (F1-F3) for test case 2.

As the LFSI model fix an initial power value with the ideal sources, any minor difference between the LF calculated value and the time-domain full internal component model cause transients that cause a delay in reaching the steady-state.

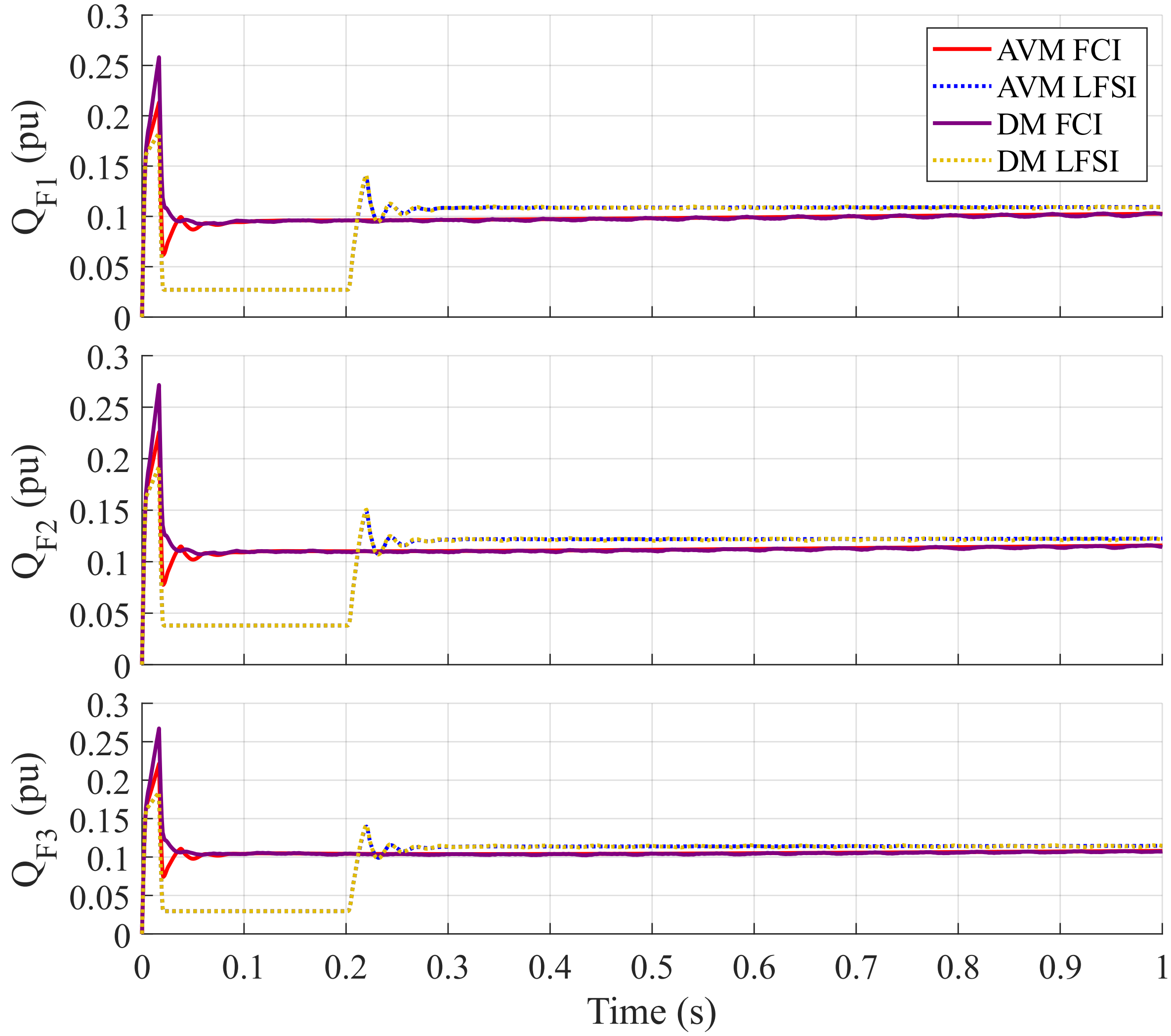

Figure 2.16 Reactive power in feeders one to three (F1-F3) for test case 2.

2.3.3 Test Case 3: IEEE 34 Bus, 24.9kV Distribution test System With 14 Aggregated PV Parks

This section presents the initialization of a computationally more challenging case, i.e., the IEEE 34-node test feeder power system, which includes fourteen PV parks [69]. The parameters of the PV parks can be found in [70]. For this test case it will be assumed an irradiance of 400 W/m^2 at 25°C for all the PV parks. All PVs operate in Q-mode with zero reactive power reference for this scenario. Figure 2.17 illustrates the single-line diagram of the 24.9 kV, 60 Hz power system. The transmission lines involved in the system are modeled with PI-liness, and the transformer saturation is considered. Constant power loads are used.

The initializations of three PV parks, located at 802-806, 836-840 and 848, are studied in detail. These three PV parks have been selected because they are located at extreme locations of the test system, as seen in Figure 2.16 and have different power generation capacities.

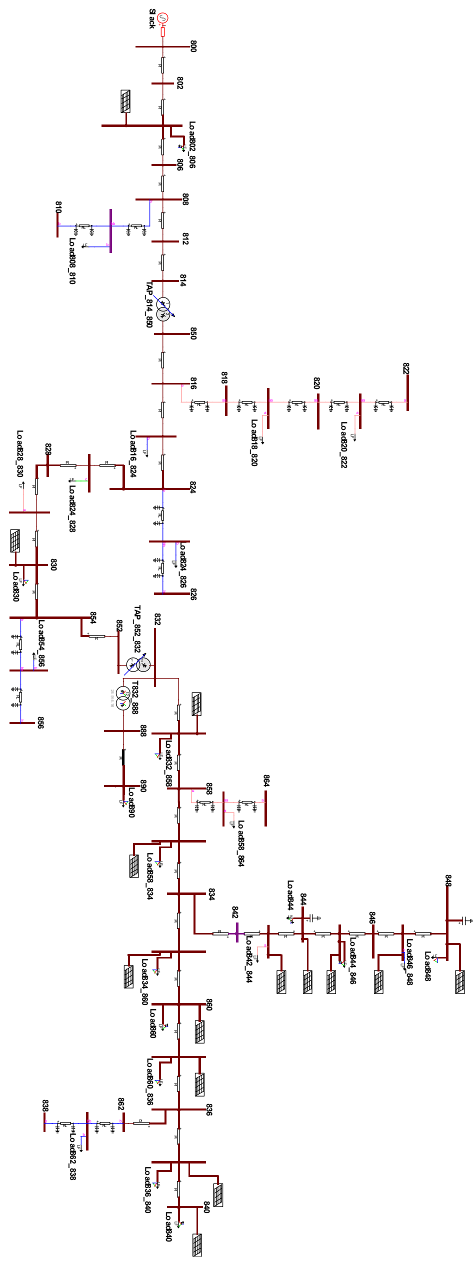

Figure 2.17 Test feeder 3, IEEE 34 node test feeder.

Figure 2.18 shows the average active and reactive powers at the POI for PV 802-806. Transients are visible for the instant of connection for the LFSI at 0.4 s. A distinct transient is visible following the instant of connection at 0.4 s, lasting until approximately 0.42 s. This disturbance is caused by the simultaneous switching of the 14 parks under the LFSI technique. Although the switching impact of a single park is minimal, the cumulative effect of connecting all units concurrently is considerable. While a staggered reconnection strategy could mitigate this cumulative transient for the LFSI approach, it would inevitably prolong the overall initialization time. The results for the remaining PV parks follow a similar trend and are summarized in **Error! Reference source not found.**. Furthermore, for the DM, the proposed method reduces the computation time by 53%, saving approximately 20 minutes for a 0.29 s simulation window. This highlights the significant computational savings achieved, which is particularly beneficial for parametric studies requiring the evaluation of multiple simulation scenarios on the same grid.

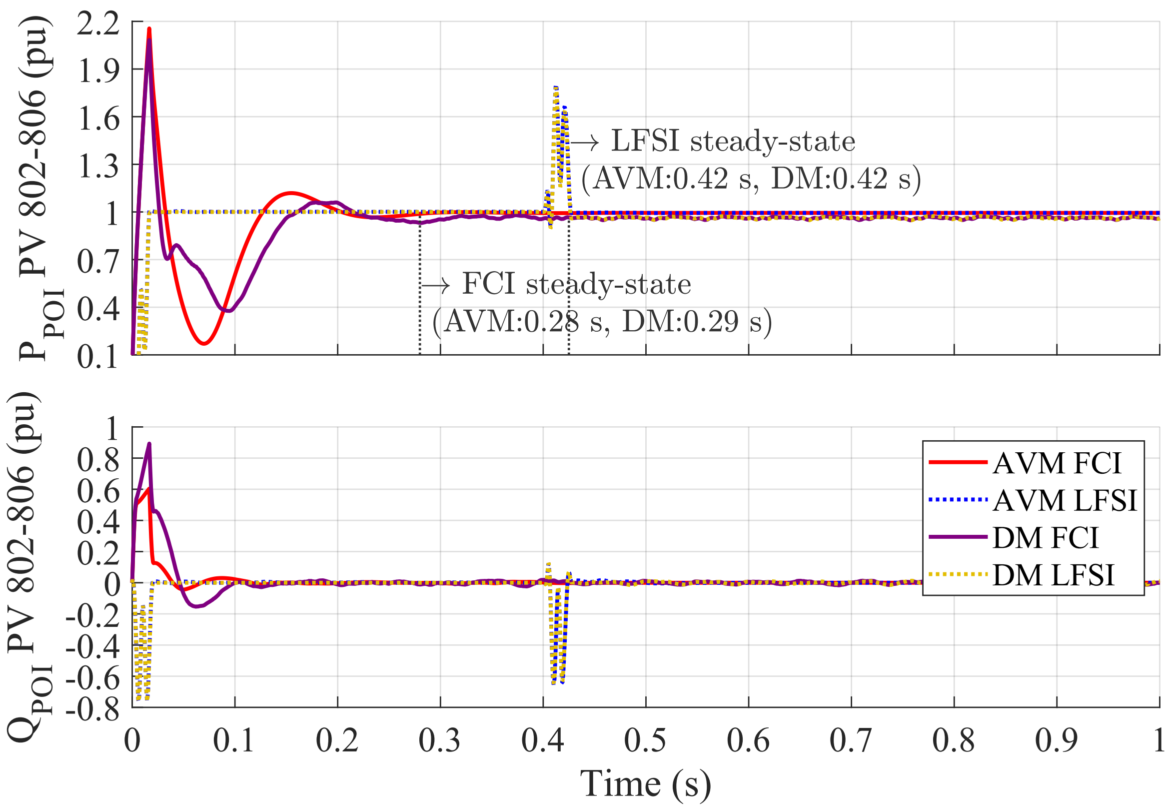

Figure 2.18 Average active and reactive power at POI for PV 802-806 for test case 3.

For PV 836-840, a 16.41 kW PV system is employed. The AVM simulation with LFSI requires 0.42 s to reach a steady-state with a corresponding computational time of 58.21 s. FCI permits to reach a steady-state at 0.22 s with a computational time of 27.31 s. As for the DM, LFSI requires 0.42 s with a computational time of 2340.66 s, while FCI requires 0.24 s and 985.25 s computational time, respectively. The comparison of the average active and reactive powers at the POI is shown in Figure 2.19.

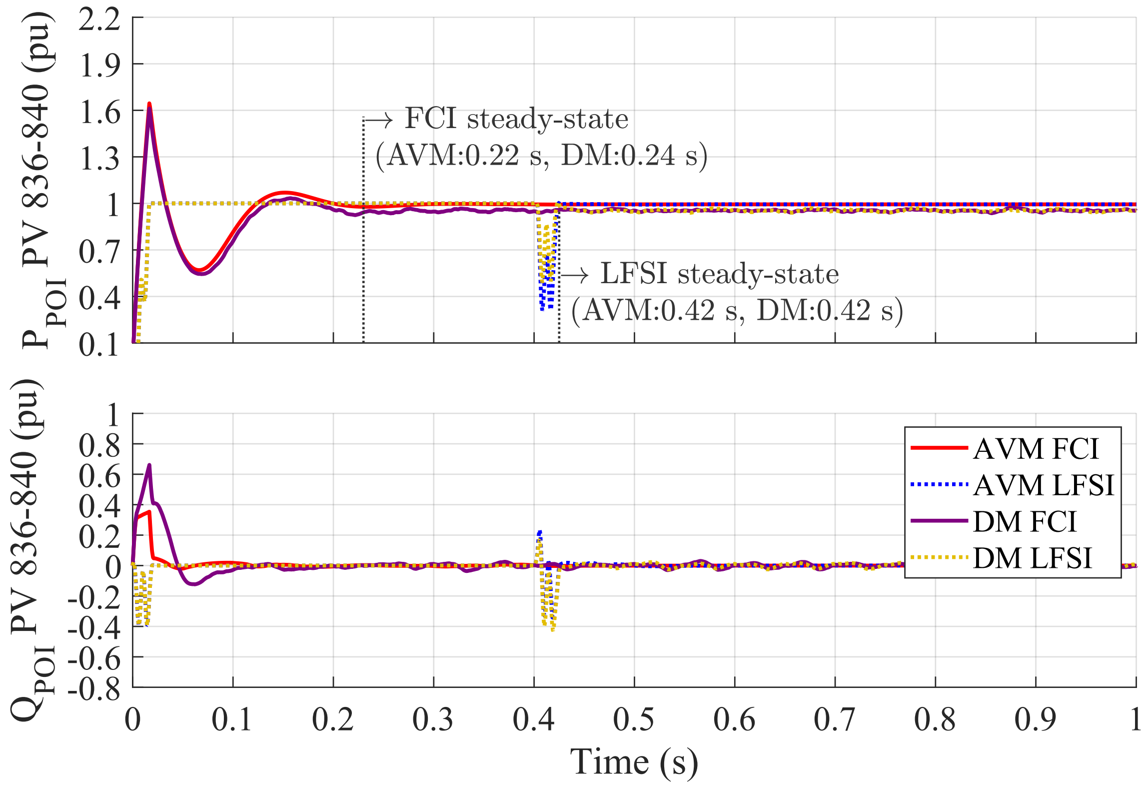

Figure 2.19 Average active and reactive power at POI for PV 836-840 for test case 3.

For the PV 848, a 23.44 kW PV system is employed. The AVM with LFSI takes 0.42 s to reach steady-state with a computation time of 58.21 s. In contrast, the FCI method attains a steady-state in just 0.11 s, corresponding to 17.44 s of computation time. For the DM, the LFSI method exhibits identical performance, with a steady-state time of 0.42 s and 2340.66 s of computation time and for the FCI, 0.11 s and 650.38 s, respectively, the power waveforms are shown in Figure 2.20.

Finally, **Error! Reference source not found.** shows the initialization time required for all fourteen PV Parks of test case 3, complementing the results presented in the previous figures and emphasizing the effectiveness of the proposed initialization method.

The most considerable initialization time for the LFSI corresponds to PV 802-806. This is due to the proximity of this PV to the infinite bus, where the current of the slack bus has a more critical role.

For the AVM, the required simulation time and computation time are reduced by a factor of 1.5 and 1.9, respectively, when comparing FCI to LFSI. For the DM, the required simulation time and computation time are reduced by a factor of 1.4 and 3.6, respectively.

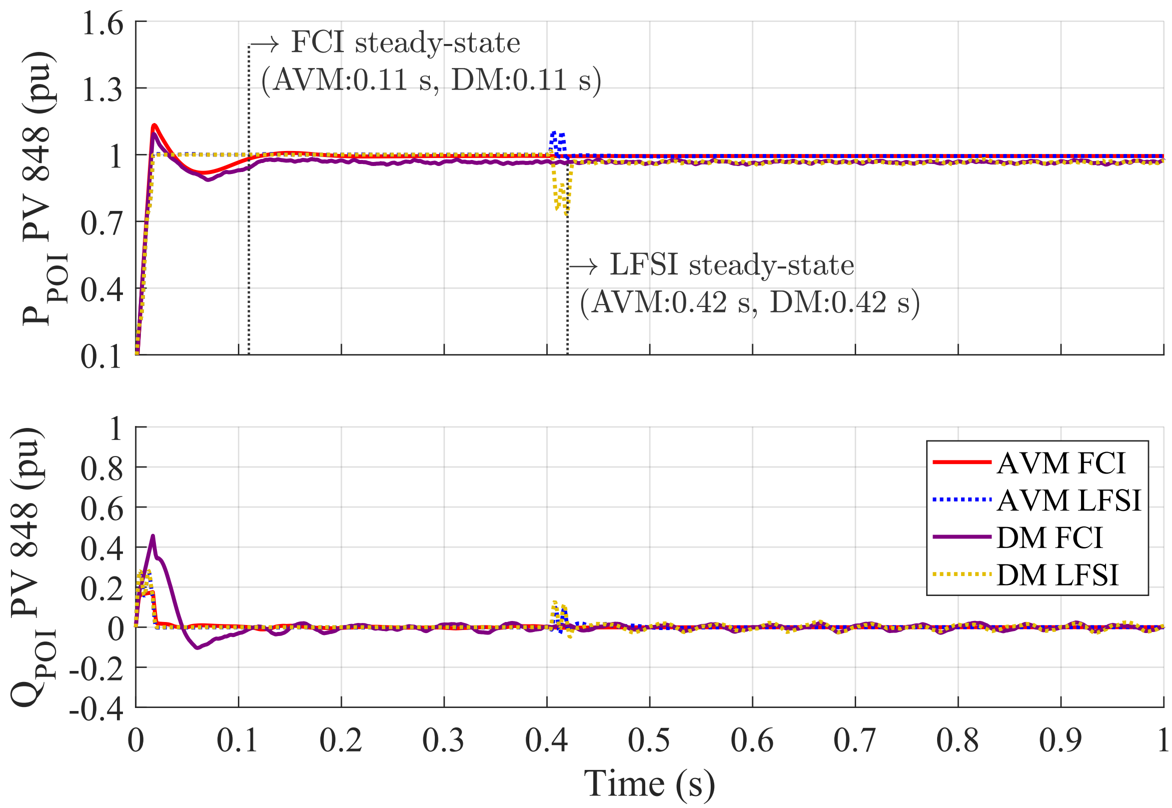

Figure 2.20 Average active and reactive power at POI for PV 848 for test case 3.

Table 2.3 Initialization time of pv parks for test case 3

PV Park	Active power PVs	AVM		DM	
		LFSI	FCI	LFSI	FCI
802-806*	21.89 kW	0.42 s	0.28 s	0.42 s	0.29 s
830	17.58 kW	0.42 s	0.28 s	0.42 s	0.28 s
832-858	5.86 kW	0.42 s	0.25 s	0.42 s	0.21 s
834-860	53.14 kW	0.42 s	0.17 s	0.42 s	0.15 s
836-840	16.41 kW	0.42 s	0.24 s	0.42 s	0.22 s

840	10.55 kW	0.41 s	0.11 s	0.41 s	0.02 s
842-844	3.75 kW	0.43 s	0.27 s	0.43 s	0.21 s
844	158.24 kW	0.41 s	0.05 s	0.42 s	0.03 s
844-846	17.58 kW	0.42 s	0.25 s	0.42 s	0.19 s
846-848	89.87 kW	0.42 s	0.07 s	0.42 s	0.05 s
848	23.44 kW	0.42 s	0.11 s	0.42 s	0.11 s
858-834	12.50 kW	0.42 s	0.12 s	0.42 s	0.12 s
860	23.44 kW	0.41 s	0.08 s	0.41 s	0.06 s
860-836	32.04 kW	0.42 s	0.10 s	0.42 s	0.16 s
Computation time		58.21 s	30.25 s	2340.66 s	650.38 s

2.4 Conclusion

This chapter proposes an enhanced steady-state initialization method, FCI, for PV park EMT models. It is based on calculating initial control variables via backward propagation of the PV park model controllers, measurement blocks, and the converter bridge. The contributions of this work include the following.

- Development of the FCI method based on calculating initial control variables via backward propagation and initial condition definition of PV park model controllers, measurement blocks, and the converter bridge.
- Demonstration of computational savings with the FCI method compared to existing initialization methods.
- Demonstrations that the benefits of the FCI method are expected to increase with the size of the power system model.
- The technique's adaptability to other PV control models, as it is based on the PI controller's initialization, making it general and replicable.
- A detailed description of each controller component and its initialization procedure has been given, where the initialization values are generated from the PV model parameters and the LF solution. For the computationally most demanding scenario, the computation time to reach steady-state is reduced by a factor of 1.92 for the converter AVM and 2.2 for the

converter DM. It can be expected that the benefits will increase for power system models of larger size.

CHAPTER 3 FULL-SCALE CONVERTER WIND PARK INITIALIZATION

Building upon the PV park initialization framework developed in Chapter 2, this chapter extends the three-stage initialization methodology to FSC wind park models. While both systems are converter-interfaced and share a similar control hierarchy, the initialization of wind parks introduces additional challenges related to the electromechanical coupling between the turbine, generator, and converter, and the multi-level coordination between the turbine and park controllers.

In contrast to PV systems, in which the primary source is static and determined by irradiance, wind turbines comprise a dynamic mechanical subsystem with variable aerodynamic torque and rotational speed. The initialization must therefore ensure proper initialization of the mechanical model, electrical components, and control setpoints. Furthermore, the FSC architecture, in which the entire generated power passes through the converter, requires that both the machine and converter states be initialized coherently to maintain power balance and grid synchronization.

As described in the previous chapter the LFSI approach, have proven effective for PV parks but remain sub-optimal for wind parks. This technique requires a short time-domain run-up to settle converter and machine variables, introducing unwanted transients and increasing computation time. Moreover, this method do not explicitly address the initialization of mechanical torque, rotational speed, or turbine-side controllers, all of which influence the steady-state operation of FSC wind parks.

To overcome these limitations, this chapter develops a FCI procedure adapted to FSC wind parks. The proposed method reconstructs steady-state conditions across all subsystems, including the turbine, machine, converter, and control layers, using backward propagation from the load-flow solution, without requiring time-domain pre-initialization. This enables EMT simulations to start directly from the desired operating point, ensuring dynamic consistency, faster convergence, and minimal initialization transients.

The following sections of this chapter present the detailed FSC wind park model and control structure, describe the adaptation of the FCI method, and validate its performance against LFSI through case studies of increasing complexity.

3.1 Full-Scale Converter Wind Park Model

The generic EMT-model of FSC WP [71], depicted in Figure 3.1, is adopted as a reference in this chapter. It uses an aggregated representation, i.e. all WTs in the park are considered by one single model, and the filters and the collector grid are averaged and scaled to fit the WP rating. The model consists of the:

- mechanical model of the wind turbine
- PMSM
- ac-dc-ac converter, consisting of the machine-side converter (MSC) and the GSC using the AVM,
- filter and the collector grid [62], [72] and
- pitch control, described in [73], [74],
- inner and outer control of MSC and GSC,
- central WPC.

The WPC is responsible for reactive power output regulation at the POI. It can be configured in either voltage-V, reactive power-Q, power factor-PF or Q-V curve control, depending on the requirements of the grid [23], [24]. The requirement will result in a reference of reactive power Q'_{POI} for the WPC, which is used to provide a reference for voltage v' for the WTC. The voltage and the frequency are monitored by the WPC using a PLL.

The WTC, which comprises outer and inner control loops for the MSC and the GSC, is implemented as vector control. The MSC controls the PMSM speed to reduce mechanical wear and regulates active power in response to wind speed. In the GSC vector control scheme, the q- frame handles the regulation of reactive power or grid voltage [71], whereas the d-frame ensures the stability of the DC-link voltage.

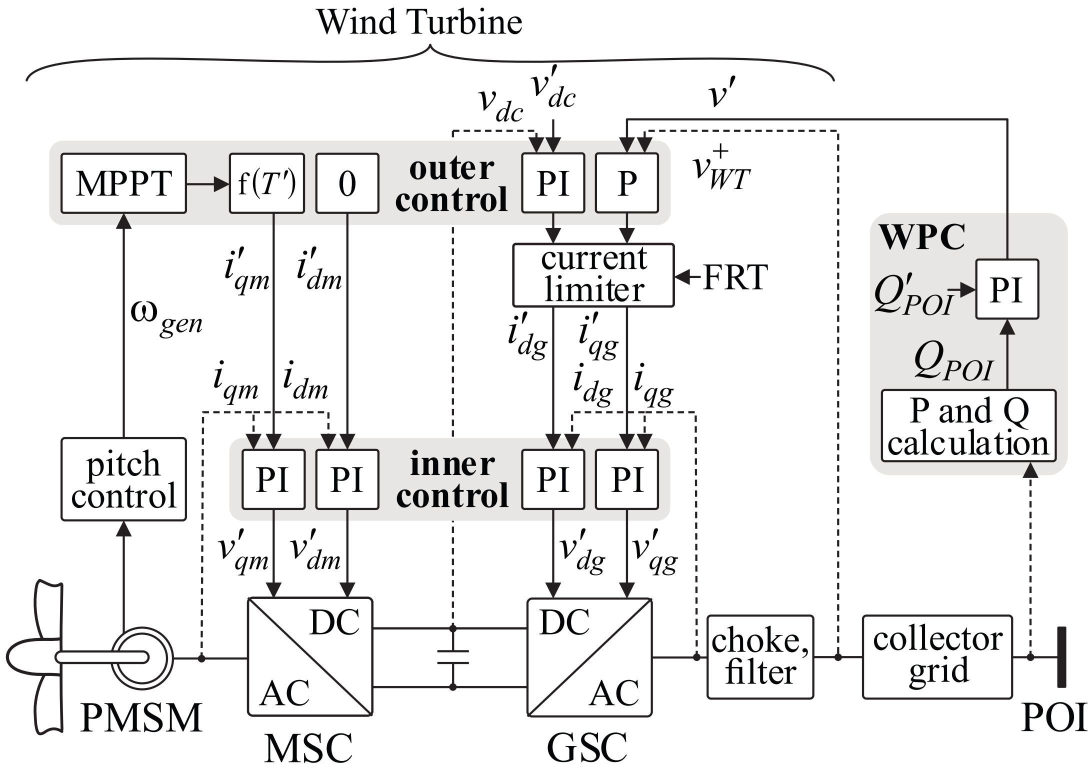

Figure 3.1 FSC WP model (frame transformations of signals are omitted).

3.2 Wind Park Initialization

The initialization can be divided into three stages, as presented in Figure 3.2.

- Stage I performs the LF solution, determining the steady-state operating conditions of the grid and the WP. The LF results provide the required phasors everywhere in the studied system. The WPs and other active sources are modeled as LF constraints.
- Stage II uses the results from the LF solution to perform a steady-state solution where the LF constraints are replaced by lumped models. The WPs are modeled as ideal voltage sources and some other sources (synchronous machines, for example) are given their equivalent steady-state models. At this stage all passive components are initialized. The control systems are initialized according to required steady-state conditions. Initialization is performed by setting all history terms in models for their following time-domain equivalents.

- Stage III performs the time-domain simulation to achieve the system's steady-state response as soon as possible. The computed steady-state voltage and power values are used to determine the converter currents in different axes (dq decomposition), which are then used for initializing the WP controls.

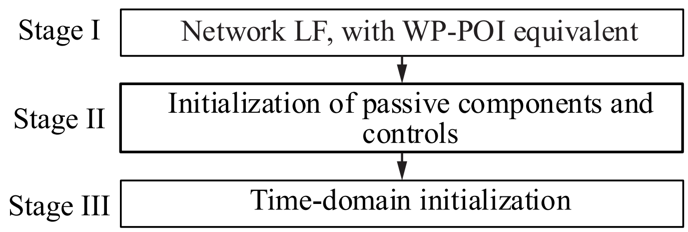

Figure 3.2 Wind Park initialization procedure.

In both initialization methods presented in this chapter, all initial values are derived from a LF solution. As the LF method is not the subject of this work, further details can be found in [42]-[44]. The LF solution provides the voltage, active and reactive powers at POI without the internal components of the wind park model that are disconnected from the system before the time-domain simulation, which enables the computation of the converter currents in the different axes. Then these values are used to initialize controls.

The challenge in initializing controllers arises from the time required for the integrators to reach a steady-state value, which is at least one period. However, this usually requires significantly more time in practice since erroneous initial conditions (setting initial integrator values to zero, for example) immediately affect MSC and GSC. Therefore, even if electrical components are initialized correctly, the control action will deviate from the LF initialization values. The integrators should be initialized at their steady-state values to avoid this condition. The initial value for the integrator is called history term H, and can be calculated using the backward propagation method [75].

Another challenge is initializing the mechanical system and the PMSM. Because the internal variables of PMSM models and other machine models in EMT-type simulation tools are inaccessible, initialization requires a time-domain stage.

Two methods are described below. The first method is the previously presented LFSI and is currently used to initialize FSC WPs in EMTP® [58], and the FCI method is the main new contribution in this chapter, as explained below.

3.2.1 LF and source initialization (LFSI)

In the LFSI method [9], during the initialization, the WP is disconnected from the power grid and temporarily connected to an ideal voltage source for a time t_{init2}, with magnitude and angle values found from the LF solution. The general scheme for the LFSI is presented in Figure 3.3. The voltage source connected to the power system prevents the transients from the WP from propagating to the power system.

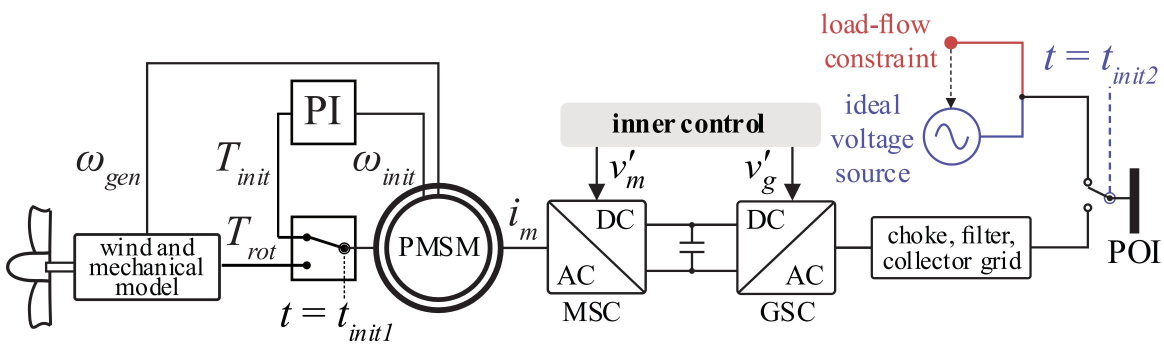

Figure 3.3 LF and source initialization for the LFSI technique.

Firstly, in stage II, the initialization of grid-side control systems, including the PLL, is performed. Since the system is assumed to be in steady-state at the beginning of the time-domain simulation, all time derivatives in the control equation are set to zero [76]. The history terms are initialized as further described in subsections 3.2.1.1 to 3.2.1.4.

In stage III, as it is not possible to impose a current value on the internal variables of the PMSM black box model, the PMSM rotor is initialized via an auxiliary PI controller loop, as shown in Figure 3.3. The initial torque, T_{init}, applied to the generator is calculated from an initial nominal speed, ω_{init} based on the characteristics of the WT parameters and the wind speed, as explained in [77]. The auxiliary PI controller is active for the predefined time, $t < t_{init1}$, and at t_{init1} the mechanical system is connected to the PMSM rotor. This procedure minimizes the transients due to the mechanical system's connection to the PMSM.

The last step for this method is the WP reconnection to the power system at t_{init2} by switching from the ideal voltage source. At this point, the variables are closer to their steady-state values, and minimal transients are observed due to reconnection. The delays t_{init1} and t_{init2} are typically defined as 300 ms and 400 ms, respectively. It is important to note that the GSC and the PLL control systems are initialized in stage II of Figure 3.2, as described below.

3.2.1.1 WPC initialization

The WPC primary purpose is to control the WP reactive power. This control is performed by a PI controller, which provides the reference voltage variation $\Delta v'$ of the q-frame GSC component to the outer control layer of the WT. The WPC controller configuration and its WTC connection are presented in Figure 3.4. In steady-state condition, the output signal from the proportional term is zero, and a history term should be included in the integrator of the PI-controller. The history term is calculated using backward propagation from the WTC outer control. First, the output of the WPC PI regulator ($\Delta v'$) is calculated by:

$$\Delta v' = \left(\frac{i'_{qg}}{k_p} \right) + v^{+}_{WT} - 1 \tag{3.1}$$

where the reference current i'_{qg} is equal to the calculated current using the LF solution at the converter terminals, and the positive sequence wind turbine voltage v^{+}_{WT} is equal to the steady-state voltage at the harmonic filter terminals.

Then, the history term $H_{v'}$ is calculated as follows:

$$H_{v'} = \frac{\Delta v'}{k_i} \tag{3.2}$$

where k_i in the integrator gain of the WPC PI is presented in Figure 3.4.

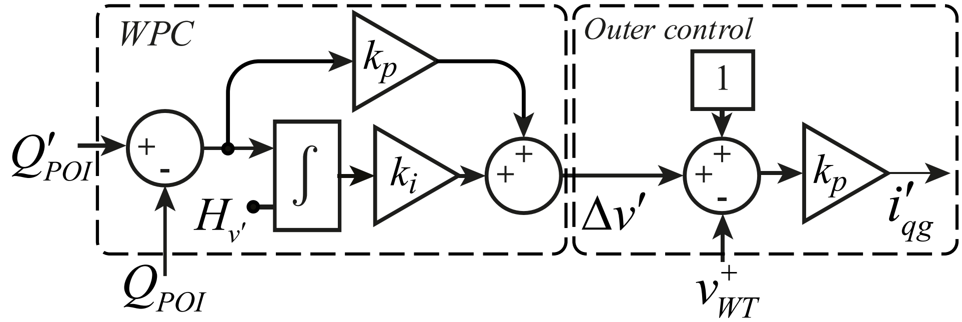

Figure 3.4 Control diagram of WPC with history term $H_{v'}$ and outer control layer of the WTC.

3.2.1.2 GSC outer V_{dc} control initialization

In steady-state conditions, the generated WP power is equal to the power transferred to the grid, and the DC-link voltage is equal to its nominal value. Thus, the integrator history term in the PI-controller can be calculated from the *d*-frame transformed three-phase currents (i_{dg}) at the GSC side, assuming $i_{dg} = i'_{dg}$. Figure 3.5 illustrates the detailed block diagram of the v_{dc} outer control loop and the d-axis inner control loop. This control configuration will maintain the dc bus voltage at its nominal value. The history term of the outer v_{dc} control loop $H_{v_{dc}}$ is calculated using

$$H_{v_{dc}} = \frac{i'_{dg}}{k_i}, \tag{3.3}$$

where the parameter k_i is defined in [71].

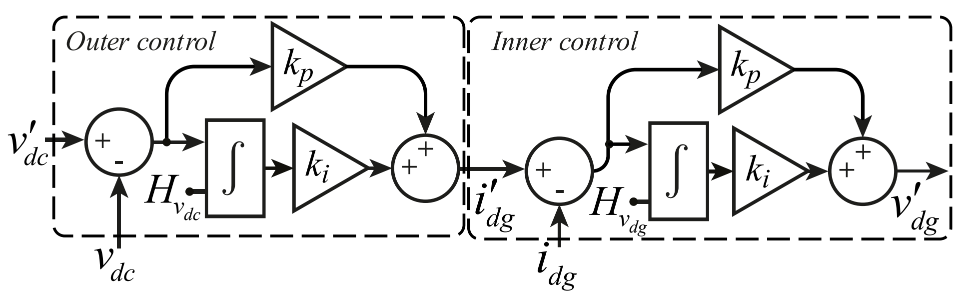

Figure 3.5 Control diagram of the GSC *d*-axis, including initialization with history terms $H_{v_{dc}}$ and $H_{v_{dg}}$.

3.2.1.3 GSC Inner current control initialization

As shown in Figure 3.6, the inner current control system provides the VSC dq-frame voltage signals. For the GSC, the history terms for the PI-controller of the *d*-axis and *q*-axis inner control loop are calculated as follows:

$$H_{v_{dg}} = v'_{dg} / k_i \tag{3.4}$$

$$H_{v_{qg}} = v'_{qg} / k_i \tag{3.5}$$

$$v'_{dg} = v_{d-choke} + \omega L_{choke} i_{qg} - v_{d-ref} \tag{3.6}$$

$$v'_{qg} = v_{q-choke} - \omega L_{choke} i_{dg} - v_{q-ref} \tag{3.7}$$

where $v_{dq-choke}$ and i_{dqg} are the *dq*-frame steady-state voltage and current, respectively, calculated at the choke terminals based on the LF results. L_{choke} is the inductance of the choke filter, ω is the nominal angular frequency, and v_{dq-ref} is the dq-frame reference voltage obtained from the LF solution.

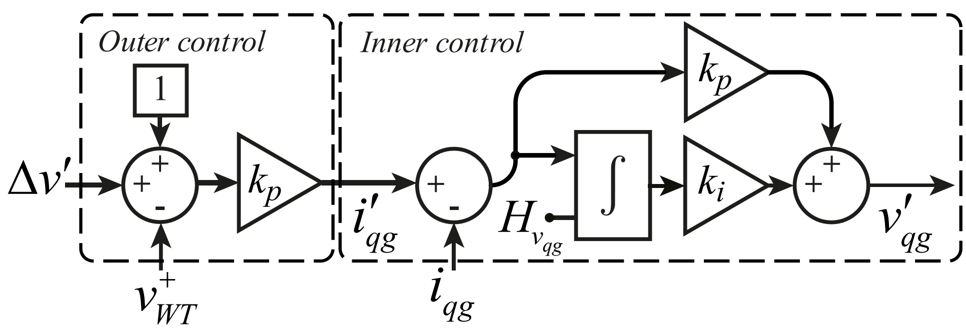

Figure 3.6 Control diagram of the GSC q-axis, including initialization with history term $H_{v_{qg}}$.

3.2.1.4 Phase-Locked Loop initialization

The phase angle and frequency of the voltage in grid-connected converters are calculated from the LF solution. In EMT simulations, a synchronous reference frame PLL continuously evaluates such phase angle and fundamental voltage frequency. To initialize the integrators of the PLL, the angular velocity and phase angle are calculated based on the nominal angular velocity and the $\alpha\beta$ -frame components of the calculated LF voltage [49], as explained in detail in the section 2.2.4.

3.2.2 Full Control Initialization (FCI)

The proposed FCI method for FSC-WP is based on the initialization of all control systems and on a specific scheme in the time-domain simulation stage to initialize the converters and the PMSM. The main scheme of the method is presented in Figure 3.7. As can be seen, in FCI, the auxiliary voltage source is moved inside the converter model during the initialization process, and the auxiliary PI controller of the PMSM is eliminated.

All control systems, including the mechanical system, are initialized in Stage II, as further detailed in this section. However, even though all the control systems are correctly initialized in Stage II, the measured quantities used as a reference to the controllers are null at $t = 0$. These transients, resulting from the controller initialization, can propagate through other elements, i.e., choke, filter, and collector grid models, increasing the delay to reach steady-state conditions. Thus, a specific scheme is proposed in the time-domain simulation, stage III, to initialize the MSC, GSC, and PMSM, as illustrated in Figure 3.7.

An AC current (I_{in-g}) source is connected in series to the GSC, as shown in blue in Figure 3.7. The current source provides the steady-state current required for grid-side elements, *i.e.*, choke, filter, and collector grid. On the other side it sets the GSC voltage. This is necessary to set the initial voltage output of the dependent source $v_{g,x}$ (x is a, b or c for the phase character). The LF solution at the POI provides the voltage phasor at the POI. The choke, filter and collector grid are then solved in steady-state to find the phasor I_{in-g}.

The initialization of the MSC must include the PMSM. The MSC should impose a current $i_{m,x}$ on the PMSM terminals, with the magnitude and angle computed from the LF solution to force a fast time-domain initialization. This current is applied by using a voltage source V_{in-m} and a dummy inductance L_{in-m} (with initialized current, initial condition) in series with the converter, for setting the initial voltage at $v_{m,x}$, as illustrated in Figure 3.7. The value of L_{in-m} is selected as 1/10th of the PMSM stator inductance to guarantee that it does not affect its time-domain behavior. The magnitude for the voltage source V_{in-m} is the nominal voltage of the system with an angle 0. The dummy inductance in this case is defined as $L_{in-m} = 57$ *nH*. This initialization approach is used to accommodate a black-box type PMSM model for the generic case. In reality, it is possible also to initialize PMSM equations automatically in EMTP®.

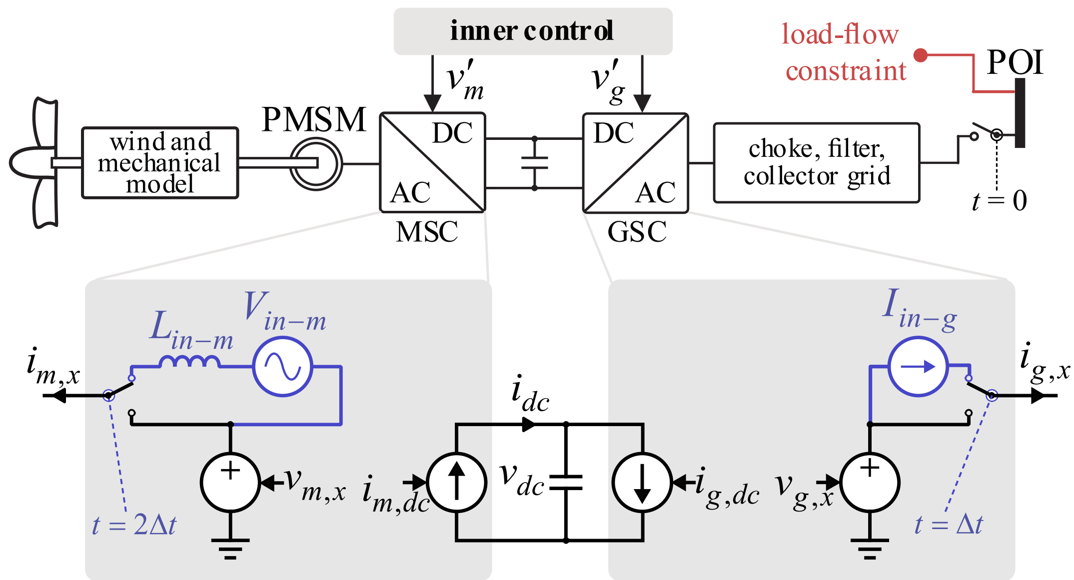

Figure 3.7 Initialization during Stage I (red) using LF constraint, and initialization of MSC and GSC during Stage III (blue), FCI method.

As a result, the following steps are required for the time-domain stage of the FCI, with numerical integration time-step Δt:

$t = 0$: The PMSM model initializes with zero current. MSC and GSC are initialized with the voltage and current sources, as illustrated in Figure 3.7.

$t = \Delta t$: The PMSM current adjusts precisely to the MSC current $i_{m,x}$. The GSC current source is disconnected from the converter (see switch at $t = \Delta t$ in Figure 3.7).

$t = 2\Delta t$: The auxiliary elements connected to the MSC are switched to regular operation (see switch at $t = 2\Delta t$ in Figure 3.7).

This interval of $2\Delta t$ is required to maintain/force the L_{in-m} currents (initial conditions on phases a, b and c) for at least one time-step (Δt), since otherwise it will drop to zero and have no impact on the PMSM initialization.

The v_{dc} voltage is initialized to its nominal value. The dc currents $i_{m,dc}$ and $i_{g,dc}$ are not initialized.

Thus, the steps needed to set the converter to the correct initial values are completed in the first two time-steps. In addition to the control systems initialized at Stage II for the LFSI method, in the FCI method, the system controls of the mechanical model and MSC are also initialized as presented.

3.2.2.1 MSC inner current control initialization

For the MSC, only the inner controllers need to be initialized. For the outer control, the *d*-axis is set to zero, while the *q*-axis depends on the mechanical model and the MPPT function and is calculated as discussed in [71]. Figure 3.8 shows the *d* and *q* branches of the MSC. The main difference compared to the GSC is the inclusion of the decoupling factors for the two branches. The history terms are given by

$$H_{v_{dm}} = \frac{\omega_{rot} X_{qm} i_{qm} - v_{dm}}{k_i}, \tag{3.8}$$

$$H_{vqm} = \frac{-\omega_{rot} X_{dm} i_{dm} - v_{qm} - \omega_{rot} \psi_m}{k_i} \tag{3.9}$$

where v_{dqm} and i_{dqm} are the calculated voltages and currents of the machine, X_{dqm} is the machine inductance, ψ_m is the mutual flux, and ω_{rot} is the angular rotor frequency.

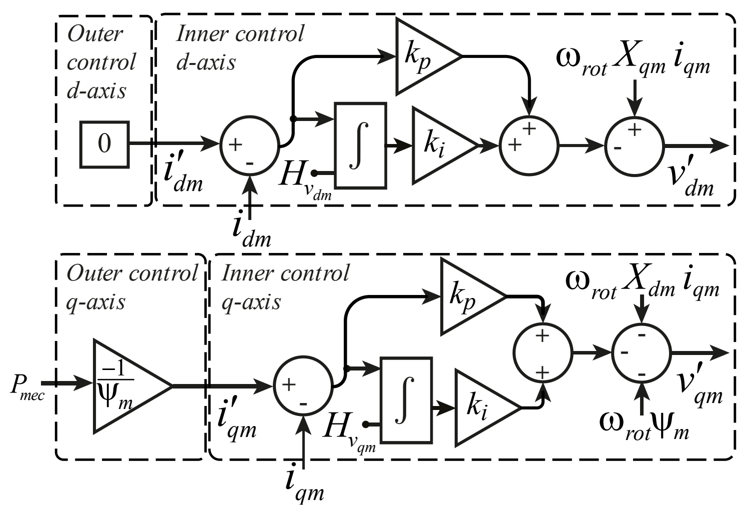

Figure 3.8 Control diagram of the outer and inner MSC, including the initialization with the history terms $H_{v_{dm}}$ and $H_{v_{qm}}$.

3.2.2.2 Mechanical Model Initialization

The diagram of the mechanical model is shown in Figure 3.9. The history terms for the turbine speed and torque, $H_{\omega_{turb}}$ and $H_{T_{rot}}$, are calculated by

$$H_{\omega_{turb}} = \frac{v_{wind}\lambda_{init}}{k_{speed}} \tag{3.10}$$

$$H_{T_{rot}} = \frac{P_{mec}}{H_{\omega_{turb}}} \tag{3.11}$$

where v_{wind} is the initial output of the wind model, λ_{init} is the tip-speed, k_{speed} is the coefficient of the gear box and the tip-speed, and P_{mec} is the mechanical power. The mechanical model, including the constants k_1, k_2 and k_3, is also explained in section 1.1.3 [62].

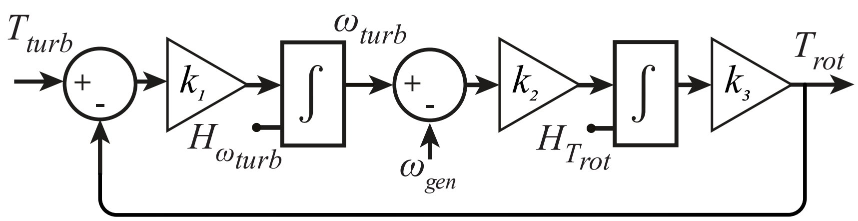

Figure 3.9 Mechanical model (two-mass model) of the WT.

3.3 Simulation Results

In this section, the performances of the FCI and LFSI methods are compared. The case without controller's initialization (no-initialization, NI) is also presented. The initialization methods are compared regarding their time-domain power waveforms at the POI, simulation time needed to reach steady-state in the time-domain, and computing times for reaching steady-state. For this purpose, a WP is considered in a steady-state when the active and reactive powers at the POI are within a range of $\pm 1\%$ of the calculated steady-state value. The measurements require one fundamental cycle to compute the active and reactive powers. All currents and voltages, however, are fully initialized for $t \geq 2\Delta t$.

Three different test cases are used for demonstration:

- Test case 1: Small system with an aggregated WP model.
- Test case 2: A small offshore system with a detailed WP consisting of 45 distinct WT models.

- Test case 3: Large-scale system with 22 sub-transmission networks, 10 aggregated FSC WPs, and 16 power plants with 35 synchronous generators.

In all WPs, the converters are modelled by AVMs and the WPC is included. The use of detailed converter models is described in [78]. It does not affect the performance of the initialization method presented in this chapter. The numerical integration time-step is 50 µs. All simulations are performed in the EMTP® software [58], and an Intel i7-8550U 1.80 GHz processor.

3.3.1 Test-case-1: System with aggregated WP

Figure 3.10 depicts the 120 kV, 60 Hz EPRI benchmark system [68]. A WP with a nominal power of 75 MW is connected to a system with two loads, and five transmission lines modelled as constant parameters (CP) lines. The WP model is aggregated, and the system's characteristics are detailed in [68].

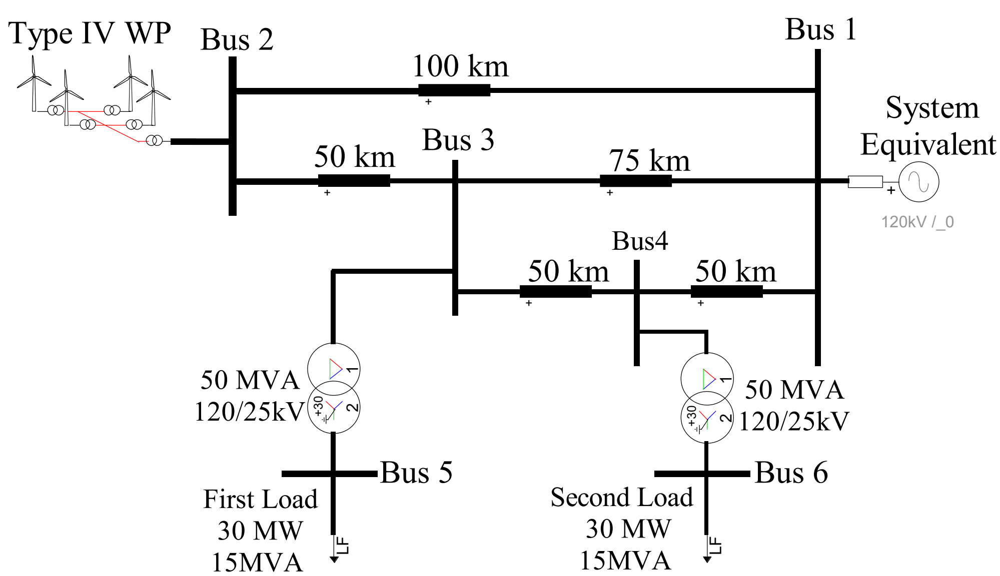

Figure 3.10 Test-case-1, EPRI benchmark with aggregated WP model.

Figure 3.11 presents the active and reactive powers at the POI for Test-case-1 for NI simulation. The NI simulation exhibits multiple cycles of power reversals, activating limiter blocks and reaching steady-state conditions at 8.57 s. Since it is evident that NI simulations demonstrate unsuitable behavior, only the time required to reach a steady-state solution with NI will be included in the tables for the subsequent test cases.

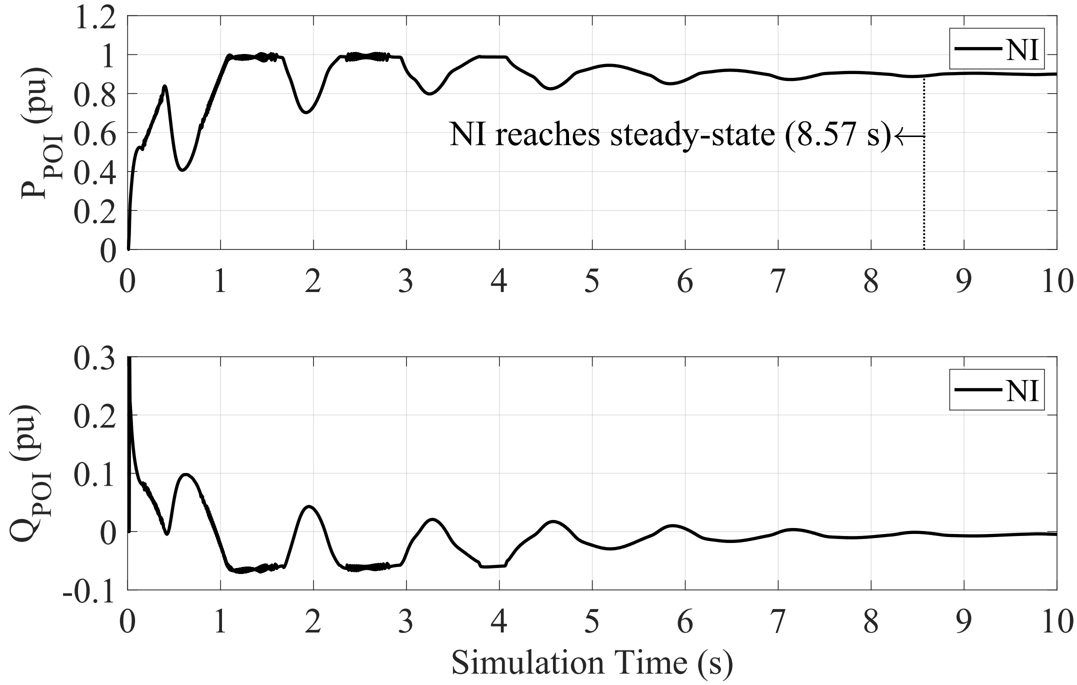

Figure 3.11 Active and Reactive powers at the POI for NI Test-case-1.

The simulation results for LFSI and FCI are shown in Figure 3.12, where the active and reactive powers at the POI are compared. For the LFSI method, the power at the WP is also included, which differs from power at the POI until the WP is reconnected to the grid. Both methods substantially improve initialization relative to the NI simulation. For the LFSI, a power variation is observed at 0.4 s when the WP is reconnected to the power system. The steady-state is reached at 1.54 s. The FCI method was able to reach steady-state at 0.22 s. Additionally, by comparing the WP power for the LFSI with the results for the FCI, it is evident that the FCI method is more effective in initializing the converters and machine.

Error! Reference source not found. compares the simulation and computing times required to reach steady-state, and the instances where the models reach the steady-state margin are highlighted in the figures. The computational cost of FCI is reduced by shortening the transient period required to achieve steady-state.

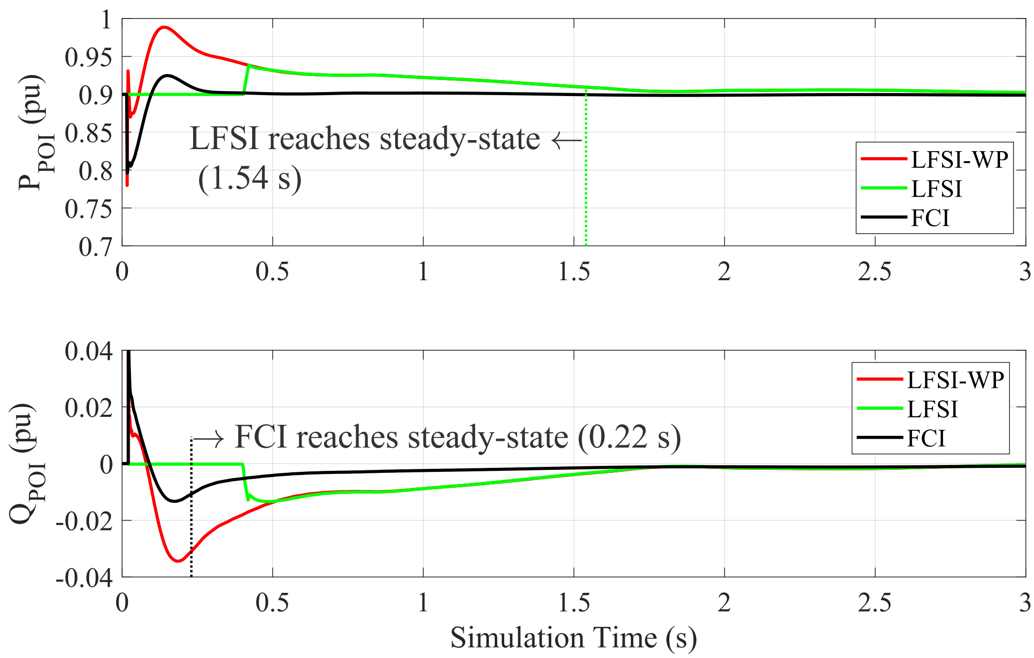

Figure 3.12 Active and reactive powers at the POI for Test-case-1

Table 3.1 Time until steady-state for test-case-1

Initialization method	Initialization time (s)	Computation time (s)
NI	8.57	62.06
LFSI	1.54	7.51
FCI	0.22	0.87

3.3.2 Test-case-2: System with detailed WP model

This case aims to demonstrate the effectiveness of the proposed FCI method for individual and unbalanced WT initialization. The WP model of Test-case-1 is now replaced with an offshore WP of 75 MW consisting of 45 individually modelled WTs, connected to the same test system of case 3.3.1. The WTs are grouped in three feeders, with eighteen (30 MVA), twelve (20 MVA), and fifteen turbines (25 MVA), as shown in Figure 3.13. A WPC is used to dispatch control references to the wind turbines shown in Figure 3.14. The WPC sets the reactive power control to zero at the POI in time-domain simulations.

Each WT is initialized starting from a PQ constraint (LF solution) with reactive power b54.6eing zero.

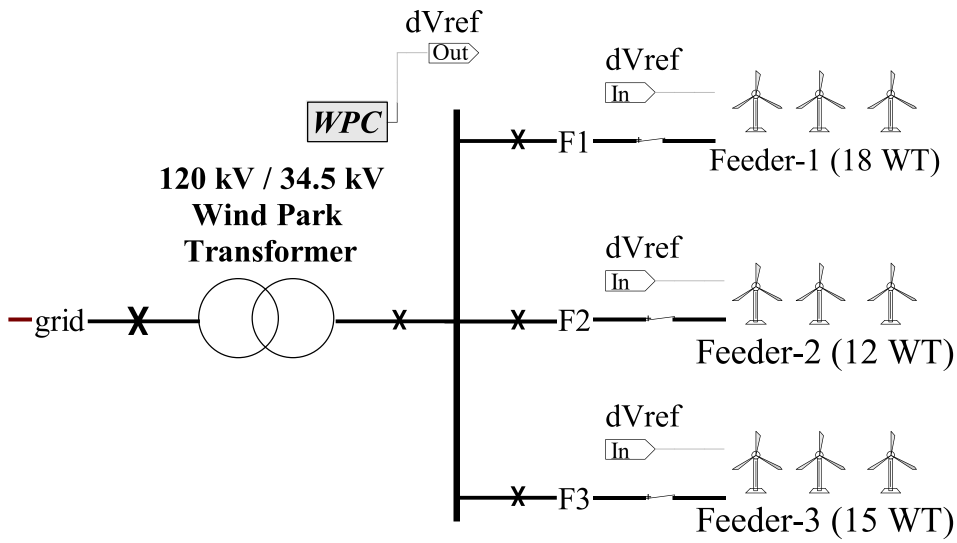

Figure 3.13 EPRI test feeder with distributed WP benchmark, Test-case-2.

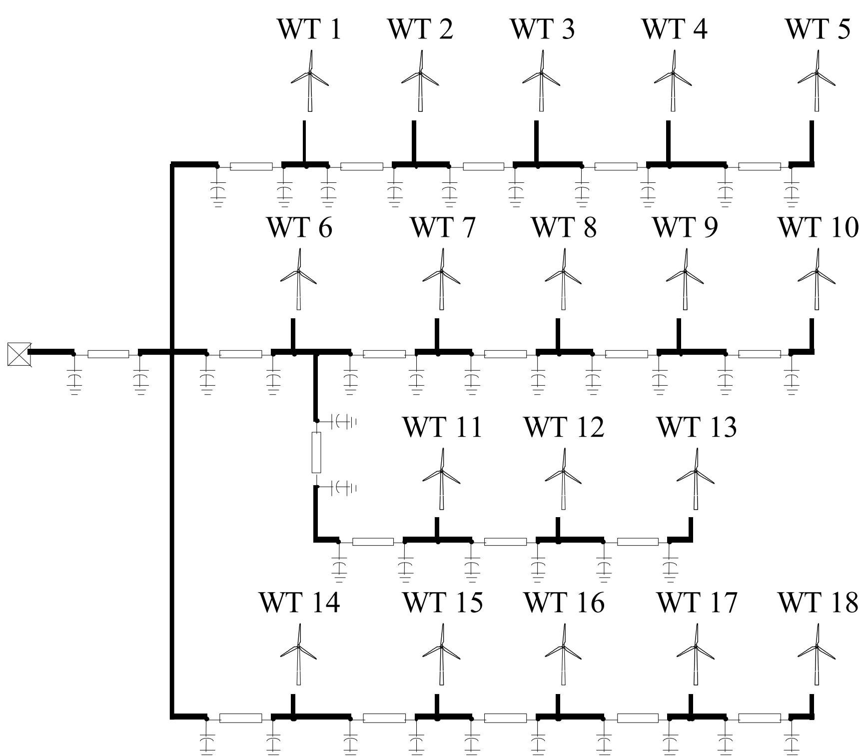

Figure 3.14 Test-case-2, detailed WP model of the EPRI benchmark with 18 independent WTs.

The collector grid is modeled in detail using PI-section submarine cable models. The cable's cross-section is shown in Figure 3.15. All data on this XLPE cable is available in the Appendix I. The cable manufacturer is [79]. The soil modeling data is also given in the Appendix I. The network beyond the POI remains the same as in test case 1.

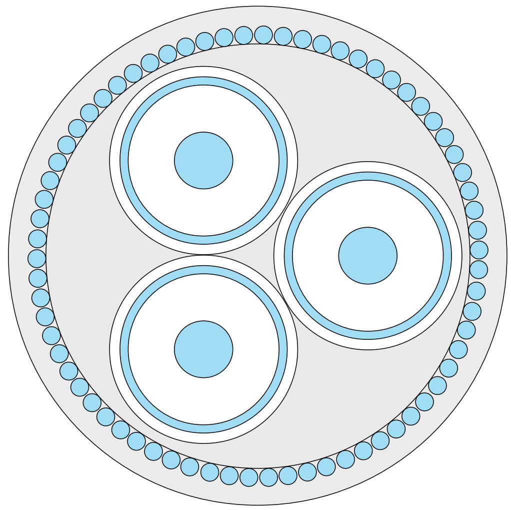

Figure 3.15 Cross-section 35kV, 3-core submarine cable.

Figure 3.16 and Figure 3.17 present the active and reactive powers of the three feeders, respectively. The measurements are performed at the points F1, F2 and F3 of Figure 3.13. The initialization and computing times are given in **Error! Reference source not found.**.

Table 3.2 Time until steady-state for test-case-2

Initialization Method	Initialization time (s)	Computation time (s)
NI	9.83	5725.14
LFSI	1.36	1107.95
FCI	0.24	104.95

As shown in **Error! Reference source not found.**, the simulation of the detailed WP model requires a longer computation time for initialization compared to the previous case. As observed the NI method now requires much more computing time than for the case of aggregated WP (Test-case-1) due to the number of WTs. The LFSI gains by 5.16 times, whereas FCI achieves a much more significant gain of 54.6.

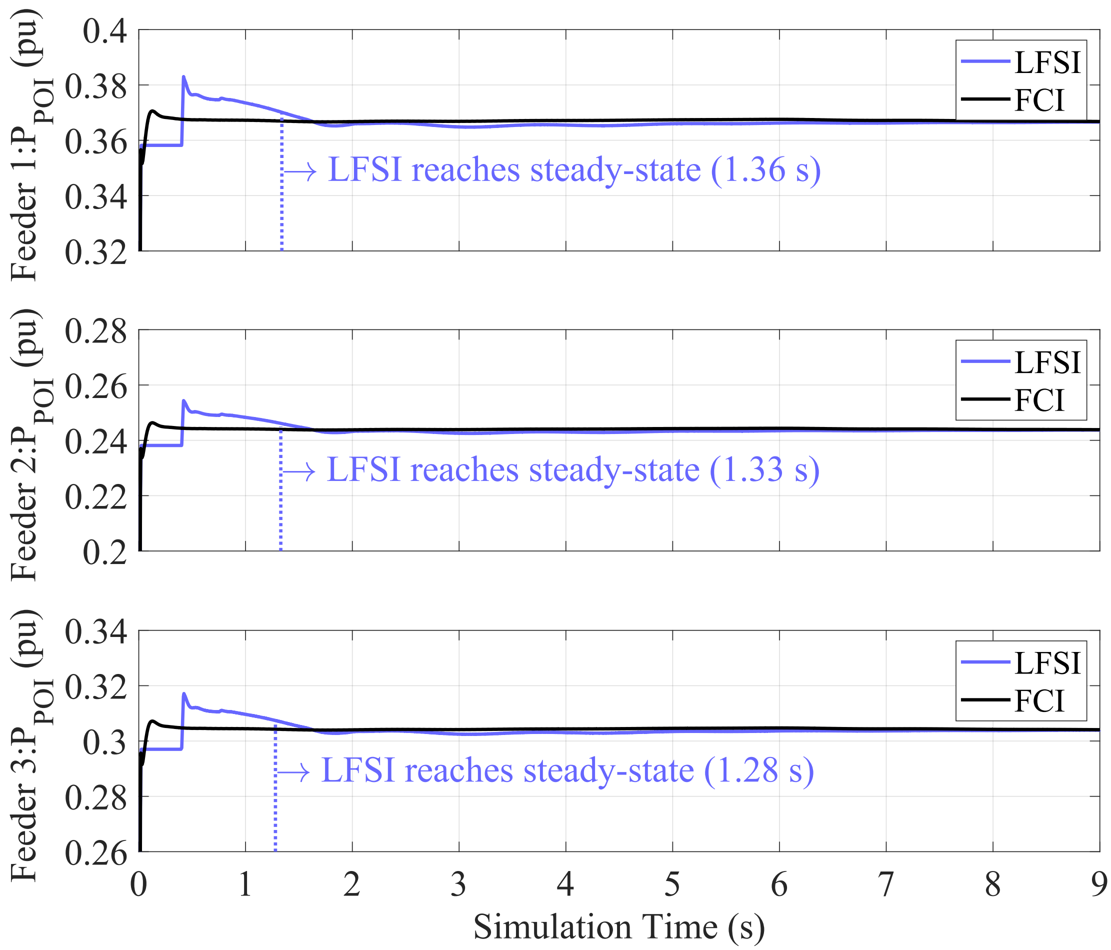

Figure 3.16 Active power profiles for Feeders 1, 2, and 3 in Test Case 2, normalized against the total WP active power.

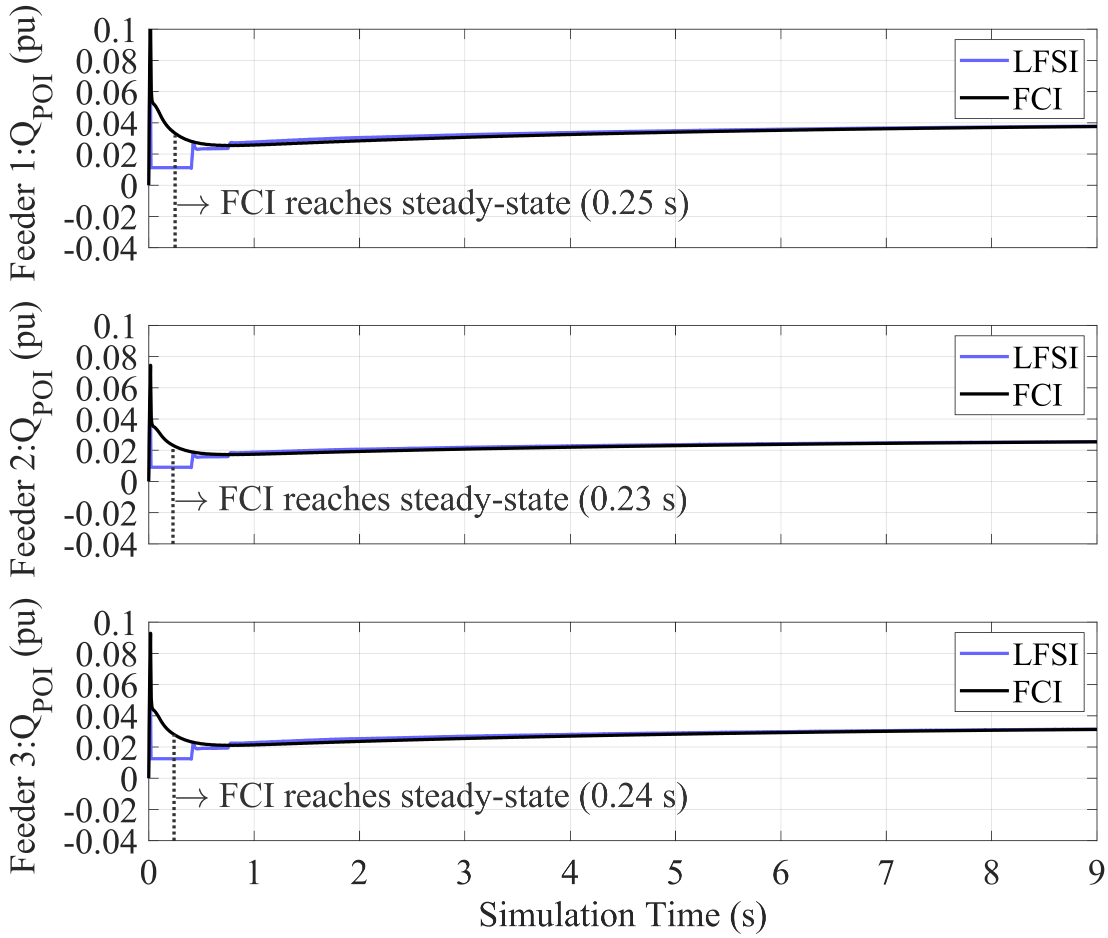

Figure 3.17 Reactive power profiles for Feeders 1, 2, and 3 in Test Case 2, normalized against the total wind park active power.

3.3.3 Test-case-3: 400/154 kV Large-scale system

The T0-benchmark power system model, described in [80], is selected as the most complex test system used here. The single-line diagram of the system is shown in Figure 3.18. It comprises a 400/154 kV system operating at 50 Hz. It includes two types of WPs, seven WPs with 35 WTs and three WPs with 50 WTs, all operating in Q-mode with zero reactive power reference. The synchronous machine models include control systems (exciters and governors), as documented in [80]. The transmission system lines are constant-parameter (CP) models, whereas the lines in the sub-transmission networks are PI-section models. Furthermore, transformer and synchronous machine saturation is considered.

In this case, two aggregated WPs are selected for detailed study: WP-A (35 WTs) and WP-B (50 WTs) due to their differing power-generation levels. The results for the other WPs, which are modelled in the same way as WP-1 and WP-2, do not provide additional insights and are, therefore, not presented in detail. However, a summary of initialization times for all WPs is given in **Error! Reference source not found.**.

The NI method presented problems in converging to a steady-state solution. As both the active and reactive powers could not reach steady-state, this case is classified as non-convergent.

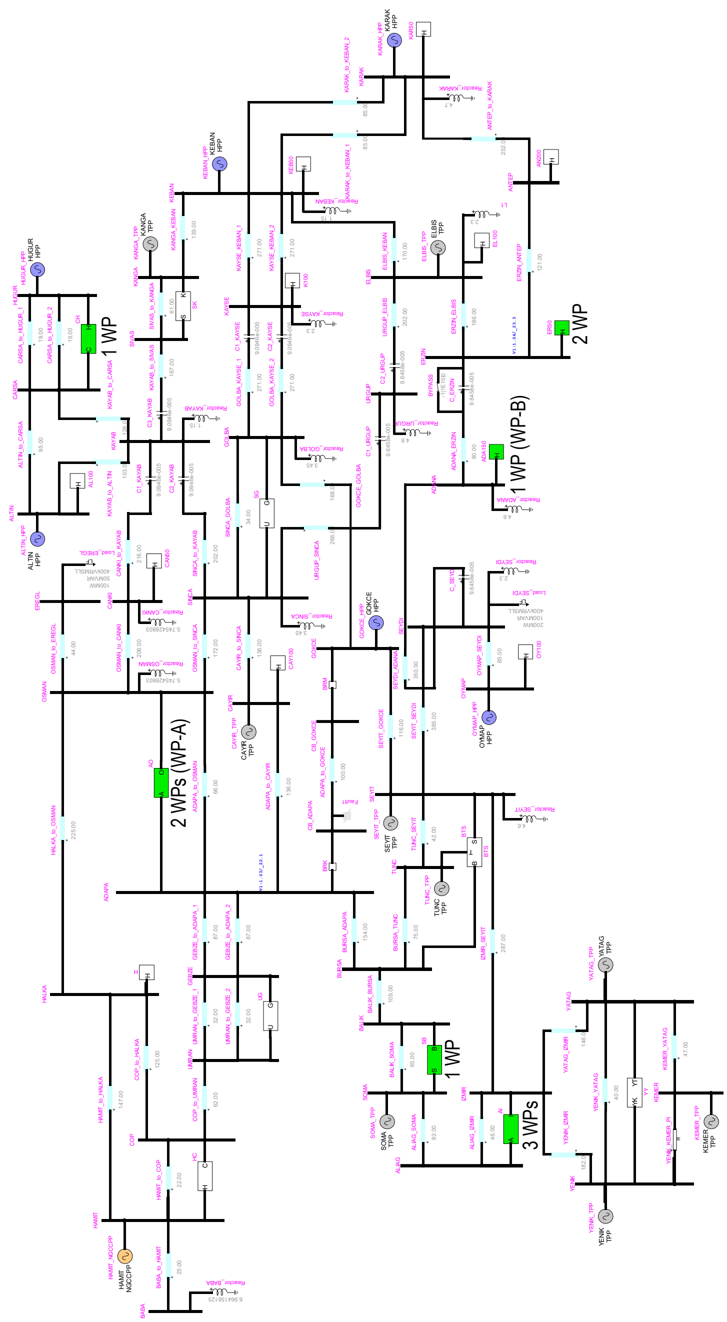

Figure 3.18 Test-case-3, single line diagram.

Figure 3.19 presents the active and reactive powers at the POI of WP-A. The initialization time for WP-A using LFSI is 1.41 s. With FCI, this is reduced to 0.15 s.

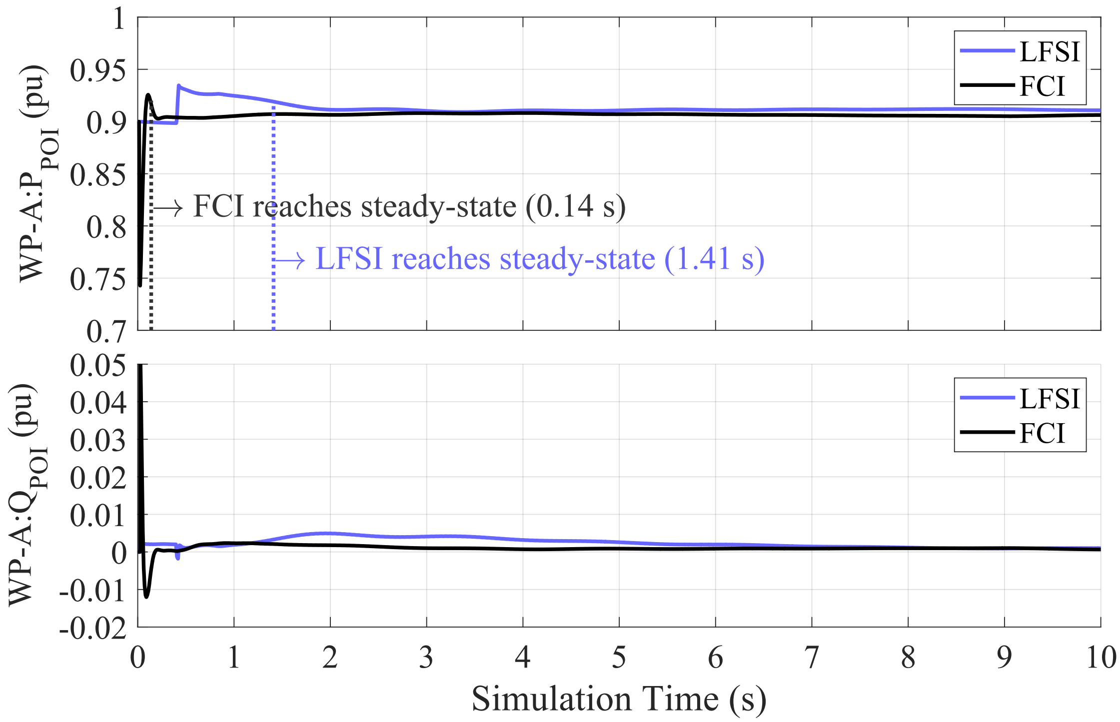

Figure 3.19 WP-A: active and reactive power at the POI.

WP-B exhibits a similar behavior, as shown in Figure 3.20. The simulation with LFSI has an initialization time of 1.40 s. In comparison, the FCI results in a reduction of the initialization time to 0.15 seconds.

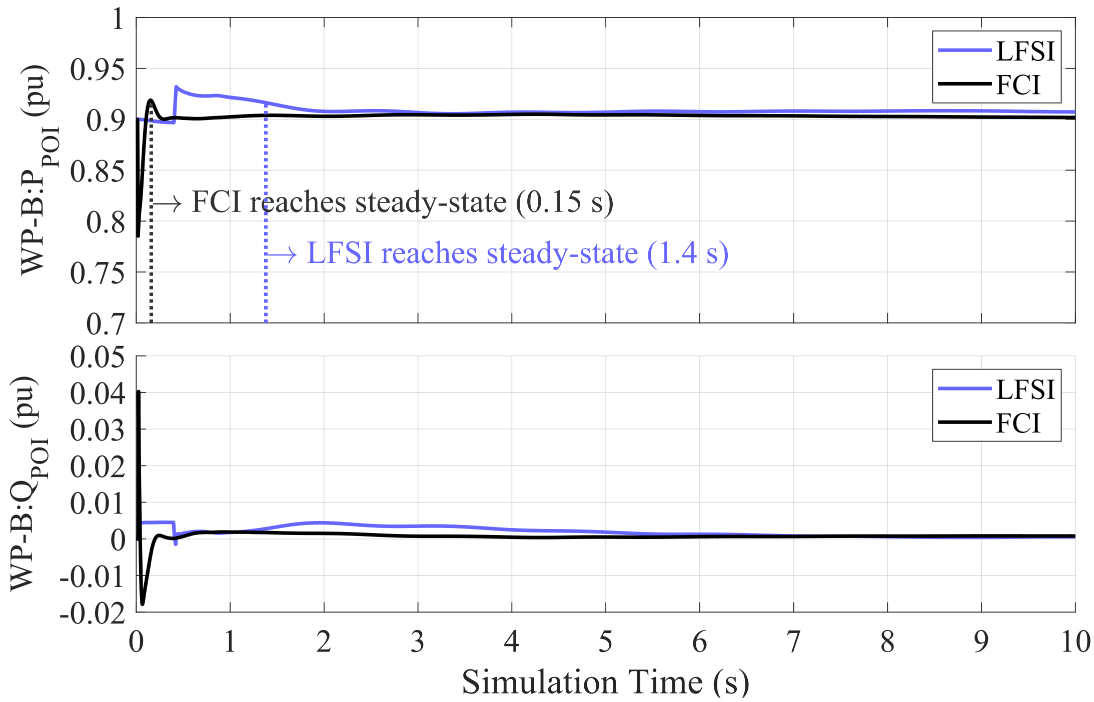

Figure 3.20 WP-B active and reactive power at the POI.

Table 3.3 Initialization and computation times for the wps, test-case-3

Wind Park Location	No. of WTs	LFSI (s)	FCI (s)
AO 1 (WP-A)	35 WT/ 75MW	1.41	0.14
ADA150 (WP-B)	50 WT/ 100MW	1.40	0.15
AI 1	35 WT/ 75MW	1.42	0.11
AI 2	35 WT/ 75MW	1.40	0.13
AI 3	35 WT/ 75MW	1.41	0.14
AO 2	35 WT/ 75MW	1.43	0.13
CH 1	35 WT/ 75MW	1.42	0.12
SB 1	35 WT/ 75MW	1.44	0.09
ER50 1	50 WT/ 100MW	1.47	0.07
ER50 2	50 WT/ 100MW	1.46	0.08
Computation time *		380.30	36.65

*2559.3 at 13 s simulation time for NI

Error! Reference source not found. shows the initialization times for all ten WPs of Test-case-3. The computation times are 380.3 s and 36.65 s for LFSI and FCI, respectively, corresponding to a reduction of 90%. The computation time is measured when all WPs reach steady-state, i.e. at a simulation time of 1.47 s for LFSI and a simulation time of 0.15 s for FCI.

3.4 Conclusion

This chapter proposes a practical and effective method for fast initialization of full-scale converter WP EMT generic models. The method uses the load-flow solution and backward propagation to initialize passive components and control systems. Furthermore, a specific scheme is proposed to initialize the converters and the PMSM. The proposed method is designed for any generic model of FSC WP as long as the control parameters are available to be set with an initial condition, making it a practical solution for models in commercially available EMT-simulation tools.

The effectiveness of the proposed method is demonstrated using three power system models of different scales and complexity, including both balanced and unbalanced systems. The solution is then compared to an existing initialization method. In all cases, the proposed method demonstrates superior performance, reducing computation time by 90%. For the computationally intensive case of a detailed WP with distinct WT models, the proposed technique reduces the simulation time for initialization transients from 95 minutes (non-initialized) to over 18 minutes (existing LFSI) to under 2 minutes when a tolerance of one percent is considered.

CHAPTER 4 DFIG WIND PARK INITIALIZATION

Existing initialization methods for DFIG wind parks can be broadly categorized into three main groups [59]. The first two, phasor-based [76] and EMT-based techniques [54]-[57] present notable limitations that limit their effectiveness in modern power system studies. Phasor-based solutions are primarily designed to determine nominal frequency steady-states; however, they inherently struggle to represent non-linear converter behavior and high-frequency control interactions. While EMT-based approaches offer higher fidelity, they are often constrained by prohibitive simulation times, convergence instability, and, in many instances, inaccuracies in achieving steady-state. Historically, these techniques have relied on simplifying the mechanical models, the internal behavior of the wind park, and its hierarchical controllers to reduce computational overhead. Such simplifications are increasingly inadequate for modern EMT simulations, where high-fidelity representations of the mechanical drivetrain, induction generators, and fast-acting power electronics are crucial for capturing the precise operational behavior required for rapid, accurate initialization.

Furthermore, these methodologies are generally restricted to simple, idealized grid configurations. Most existing frameworks operate under the assumption of perfectly balanced conditions and are limited to positive-sequence analysis, which fails to account for the complexities of modern, asymmetrical, or weak-grid real scenarios. By focusing on these simplified mathematical domains, current research overlooks the impact of unbalanced conditions on the initialization process. Consequently, there is a distinct lack of comprehensive solutions capable of addressing the multi-physics challenges of DFIG systems, specifically the simultaneous requirement for detailed mechanical-electrical coupling, unbalanced condition handling, and computational efficiency. The methodology proposed in this work fills this critical gap, providing a robust initialization framework that remains accurate where existing positive-sequence and phasor-based methods fail.

The third category relies on LF algorithms, which generally initialize state variables for various grid components more reliably [81]. However, applying traditional LF methods to DFIG wind parks often requires significant time to reach steady-state for the dynamic components, as the interactions between the generator and the converter are complex to include in the LF simulations. To tackle this problem, certain papers have proposed different initialization techniques. In [29] a simplified model of the wind turbine (WT) controllers, without WP controller is considered. In

[82] only the DFIG parameters based on LF conditions are calculated, but no time-domain initialization of the control is considered. Finally, [83] does not consider the mechanical model, PLL, and WP controls.

Multiple studies have advanced LF-based initialization of IBR by integrating a comprehensive steady-state analysis of power and control equations, allowing for complete initialization of all model components. For instance, [14] presented this technique for Modular Multilevel Converters (MMCs), [78] applied it to PV parks, and [84] extended it to full-scale converter-based WPs, but none consider the complexities of the DFIG.

Compared to wind parks with full-scale converters, DFIG-based wind parks present significant modeling challenges. Because the converter bridge is directly coupled to the induction machine, a joint representation of both components is required. The strong coupling among electrical, mechanical, and control subsystems makes the model highly sensitive to initialization: even slight inaccuracies in the initial conditions can propagate throughout the system, producing undesirable transient disturbances.

To address these limitations, this chapter introduces a comprehensive FCI method designed explicitly for DFIG wind parks. The proposed approach reconstructs the steady-state conditions of the mechanical model, the induction machine, the converter, and all associated controllers within a unified framework. By aligning each subsystem with the load-flow operating point prior to the EMT simulation, the method significantly reduces initialization transients and improves numerical robustness. Due to the technical constraints of other existing techniques as previously mentioned, which lack the capacity to handle the full representation of the DFIG wind park model, including its complex mechanical and control subsystems, the performance of the proposed FCI method is validated through a series of case studies and comparative evaluations exclusively against the LFSI initialization technique.

4.1 DFIG Wind Park Model

This chapter is based on the DFIG WP model for EMT simulations depicted in Figure 4.1. The WP model uses an aggregated modeling approach, as described in [58], [78] and [84], where a single equivalent DFIG WT represents the entire park capacity, with the collector grid (CG) and filters scaled accordingly.

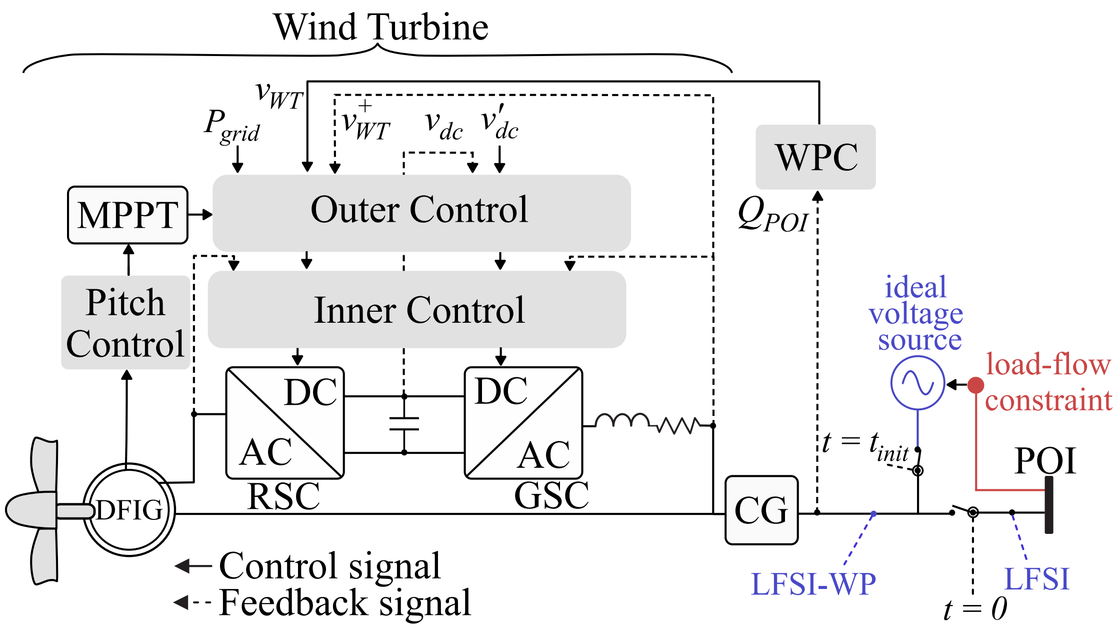

Figure 4.1 DFIG wind park model with LF initialization.

Figure 4.1 illustrates the generic DFIG WP configuration: a wind turbine with an aerodynamic model (including pitch control) and a two-mass model of the mechanical part, an induction generator (IG) whose stator is connected directly to the collector grid, while the rotor is interfaced to the grid through back-to-back converters. The RSC and the GSC share a dc link. A choke filter is included on the GSC output to meet harmonic standards. A WPC supervises the entire WP, regulating reactive power or voltage at the POI via an outer control loop for the WP [18]. The WPC monitors the POI voltage and frequency via a PLL and can operate in voltage-control, reactive-power, power-factor, or Q–V droop modes, depending on user requirements.

The DFIG IG is modeled in a stator-flux-oriented reference frame for control purposes. Under steady-state conditions, the stator feeds power to the grid at the grid frequency. At the same time, the rotor is excited at slip frequency through the RSC, enabling variable-speed operation around synchronous speed. The model includes a crowbar and a DC-chopper to protect the RSC and dc link, respectively, but under normal operation, they remain inactive.

The DFIG control is implemented as a two-level vector control for both RSC and GSC. The RSC's outer controllers regulate generator active power from the MPPT and determine the reference power at the POI to match the grid active power P_{grid}. They either set the stator voltage or the reactive power through the reference voltage v_{WT} of the WPC. The GSC's outer loop regulates the dc-link voltage v_{dc}, and can manage reactive power exchange with the grid. Both converters use fast inner current PI controllers to set the reference rotor voltages v'_{dr}, v'_{qr} and GSC voltages v'_{dg}, v'_{qg} and slower outer controllers, with limiters and fault ride-through (FRT) logic to set the reference currents from the rotor i'_{dr}, i'_{qr} and GSC currents i'_{dg}, i'_{qg}. The WPC coordinates the wind park behavior based on the reactive power at the POI Q_{POI}. This aggregated generic DFIG model captures key nonlinear dynamics and control features, enabling accurate EMT simulations. The components in blue and red are related to the initialization procedure and will be explained in detail in the section 4.3.

4.2 Proposed DFIG Initialization Procedure

The proposed initialization process for DFIG wind parks consists of three stages [84], as illustrated in Figure 4.2.

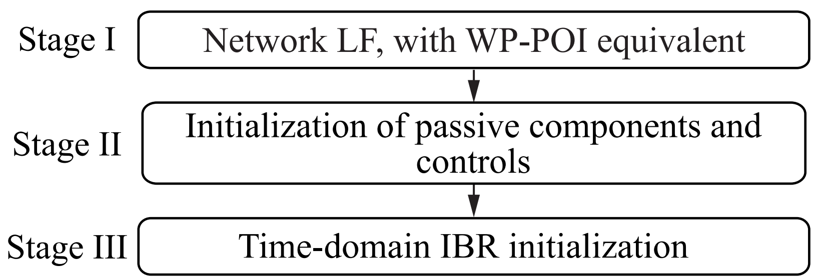

Figure 4.2 Initialization process for DFIG WP.

4.2.1 Stage I - LF Solution:

The initial step in initialization involves identifying the system's steady-state operating point by applying an LF solution, while accounting for the controlled bus constraints within the grid. This process sets the steady-state conditions for voltage, current, and power across the system, including the configurations at the POI of the DFIG wind park model. This phase will not be elaborated on in this thesis, but it is extensively discussed and examined in other sources including [41]-[44].

4.2.2 Stage II - Initialization of the passive components and controls:

Once the LF results are obtained, the steady-state solution uses lumped models to determine the initial current and voltage values across all non-inverter-based component resources at $t = 0$. This includes the internal settings for rotating machines and passive components like lines, cables, and transformers. To reach the steady-state solution, history terms within the steady state simulation are replaced by parameters calculated from the LF results. This algorithmic approach follows the methodology described in [58].

4.2.3 Stage III - Time-Domain Initialization:

The final step involves initializing the most complex components of the DFIG model. In this stage, the initial conditions for the back-to-back bridge controllers, mechanical system, induction machine, and electric converter components are calculated.

To account for all the complexities of the DFIG, it is necessary to align all subsystems with the LF setpoints, reducing settling time and avoiding convergence issues. Since the procedure involves non-linear component calculations and multiple steps, the entire sequence is summarized in the following list, which is implemented within the WP model (Figure 4.3) as the final step in the initialization process. The following steps are further explained in section 4.3 and referred to as initialization algorithm (IA).

- Acquire network operating point from the LF at the POI:
- Acquire voltage and current at the POI (V_{POI} and I_{POI})
- Back-propagate V_{POI} and I_{POI} through transformers and impedances to obtain the WT voltage V_{WT} and current I_{WT}.
- Calculate the induction machine steady-state solution:
- Choose frame alignment in *dq*-frame $V_{ds} = 0$, $V_{qs} = V_{WT}$.
- Fix reactive power by setting $I_{ds} = Q'_{POI} / V_{qs}$. A unity PF is assumed for GSC.
- Calculate I_{qs}.
- Initialize the machine state variables:
- Calculate the flux linkages for the stator λ_s, and rotor λ_r in the *dq*-frame.

- Calculate the rotor currents and voltages: I_{dr}, I_{qr}, V_{dr}, V_{qr}.
- Calculate the stator powers: P_s and Q_s.
- Calculate the GSC powers: $Q_{gsc} = 0$ and $P_{gsc} = -P_r$.
- Compute I_{dg}, I_{qg}, V_{dg}, and V_{qg} via choke (R_{choke}, L_{choke}).
- Initialize controllers and hardware:
- Compute the initial condition of the PLL following the technique proposed in [71].
- Calculate the initial conditions of the WPC $H_{v'}$, dc bridge $H_{v_{dc}}$, powers H_P and H_Q, the voltage of the rotor H_{v_r} and stator H_{v_g} in the *dq*-frame, and the electric torque T_e.
- Set GSC/RSC three-phase initial voltage magnitudes and angles (V_{in-g}, V_{in-r}).
- Compute induction machine rotor currents I_{ar}, I_{br}, I_{cr}.

The proposed method employs a backward propagation technique to set the DFIG wind park controller components into their steady-state operating points, which are computed from the steady-state solution. During this period, the LF voltage and current are used to calculate the internal electrical parameters of the GSC and RSC, which match the required active and reactive power setpoints derived from the LF analysis. Additionally, the initial calculation of the mechanical operation point is performed based on the electric power and wind parameters. This modular initialization ensures that internal transients are minimized, allowing the system to reach its steady-state without significant delays. The next section covers the calculation of various other components in detail.

4.3 Initialization of Controls

The proposed FCI provides an alternative to the LFSI method described in [84]. The LFSI technique is depicted in Figure 4.1. An ideal voltage source, shown in blue, is imposed at the POI, and an initialization of the PLL controller is also included. During the initialization process, any transient behavior is confined within the WP. During the LF solution shown in red in Figure 4.1, the WP is disconnected from the grid. The LF solution provides the voltage value used by the ideal voltage source shown in blue in this figure. At t_{init}, the ideal voltage is disconnected. A comparison of the powers LFSI at the POI and the LFSI-WP point is shown in Figure 4.10.

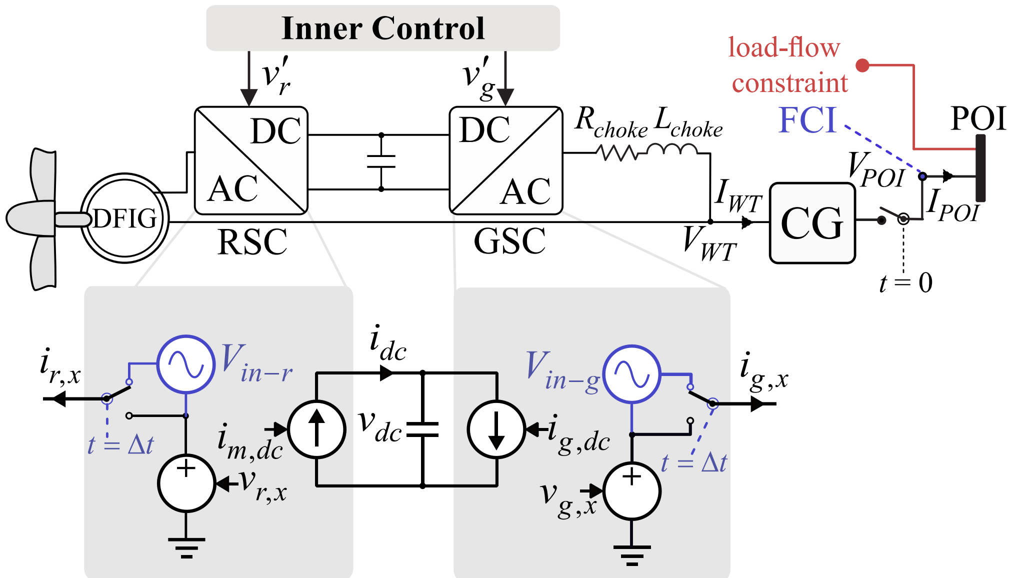

Figure 4.3 Back-to-back converter initialization.

The proposed FCI is presented in Figure 4.3. The ideal sources V_{in-r} and V_{in-g}, remain connected only for the first simulation time-point, which is Δt (numerical integration time-step). This method sets the converter voltage, preventing startup control transients and stabilizing the steady-state condition within the WP's internal components, thereby reducing initialization time. The following subsections provide a detailed breakdown of the initialization of all WP components. The x subindex in Figure 4.3 magnitudes denotes the different phases (a, b, c) for the voltage v_r, v_g and currents i_r, i_g of the converter.

4.3.1 Mechanical model initialization

The mechanical model follows the same principle of the FSC model, represented by a two-mass model, connected by a flexible shaft. The aerodynamic power P_m is converted to mechanical torque T_m. The torque transmitted through the flexible shaft, T_{sh}, is governed by the shaft stiffness K_{sh}, and the damping coefficient D_{sh}, and it represents the dynamic coupling between the turbine and generator, controlled by the turbine and generator inertia H_t, and H_g respectively.

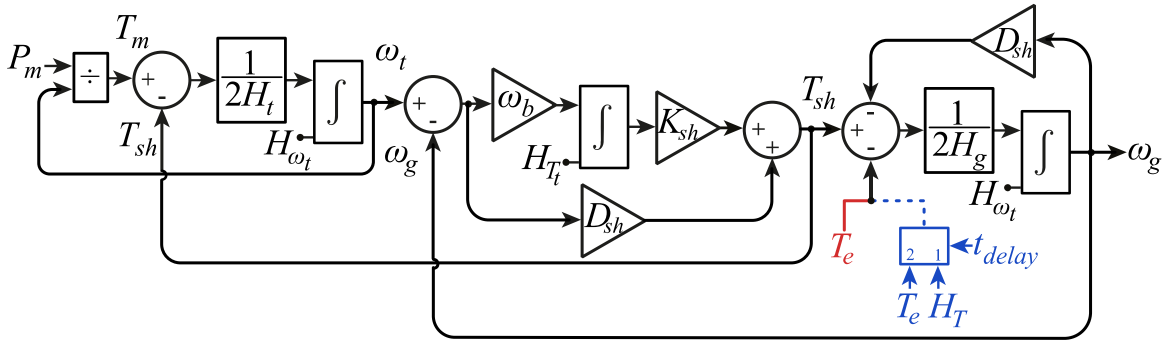

Figure 4.4 Mechanical model initialization.

To initialize the mechanical model, three variables need to be set: the torque of the shaft T_{sh}, the turbine angular velocity ω_t and the generator angular velocity ω_g, to do so, the velocity history term H_{ω_t} and the turbine torque history term H_{T_t} are determined by the initial wind speed condition and the wind park's MPPT operating point. For the LFSI technique, a constant initial torque H_T is applied while the DFIG approaches a steady-state condition. After a predefined time delay t_{delay} the initial constant torque is replaced by the electric torque T_e. In contrast, for the FCI method, the initial H_T is not needed since the DFIG parameters are set to their operational point at the first instant of time, thereby directly setting T_e to its steady-state operating point.

Both methods are illustrated in Figure 4.4, with the LFSI method indicated in a blue dotted line, and the FCI by a red line. A detailed explanation of their calculations and interactions can be found in [9].

4.3.2 Induction Machine Initialization

The initial voltages and currents in the induction machine are determined once the *dq*-frame of the machine voltage is aligned with the *q*-axis (step □ in IA), and the stator voltages are expressed as:

$$V_{ds} = 0, \tag{4.1}$$

$$V_{qs} = |V_s| = V_{WT}, \tag{4.2}$$

The initial machine conditions are calculated under steady-state assumptions, where the reference current is set equal to the actual rotor q-axis current and the stator current is defined as:

$$I_{ds} = \frac{Q'_{POI}}{V_{qs}}, \tag{4.3}$$

The stator I_{qs} current is computed using a Newton method, since it is a nonlinear function of I_{ds} due to the stator–rotor coupling and air-gap flux dependence. Once the stator currents are calculated, the machine initialization process starts in IA step □. The flux linkages for the stator can be derived from the synchronous speed ω_s and the stator resistance R_s :

$$\lambda_{ds} = \frac{V_{qs} - R_s I_{qs}}{\omega_s}, \tag{4.4}$$

$$\lambda_{qs} = \frac{R_s I_{ds} - V_{ds}}{\omega_s}, \tag{4.5}$$

with the stator flux known, the rotor currents can be calculated with the inductance of the magnetization branch L_m and stator L_s :

$$I_{dr} = \frac{\lambda_{ds} - L_s I_{ds}}{L_m}, \tag{4.6}$$

$$I_{qr} = \frac{\lambda_{qs} - L_s I_{qs}}{L_m}. \tag{4.7}$$

The rotor flux linkages are calculated as:

$$\lambda_{dr} = L_r I_{dr} + L_m I_{ds}, \tag{4.8}$$

$$\lambda_{qr} = L_r I_{qr} + L_m I_{qs}, \tag{4.9}$$

where L_r represents the rotor inductance.

Once the rotor and stator currents are determined, the stator and rotor voltages can be calculated. Afterwards, the reference frame is adjusted to establish the sources for converter initialization, and the rotor voltages can be calculated as:

$$V_{dr} = R_r I_{dr} - \omega_{sl} \lambda_{qr}, \tag{4.10}$$

$$V_{qr} = R_r I_{qr} + \omega_{sl} \lambda_{dr}, \tag{4.11}$$

where the slip angular frequency ω_{sl} is defined by,

$$\omega_{sl} = slip\ \omega_s. \tag{4.12}$$

Finally, the active power injected by the rotor side of the machine can be expressed as:

$$P_r = -V_{qr} I_{qr}. \tag{4.13}$$

4.3.3 Converter DC Bridge Initialization

Given all induction machine parameters, the only remaining parameter to determine the initial condition of the back-to-back converter is the GSC voltage, which is determined by the power transferred through it. Given the unity power factor condition of the converter, the active power balance requires:

$$P_{gsc} = -\mathrm{P}_r, \tag{4.14}$$

$$Q_{gsc} = 0, \tag{4.15}$$

the currents of the grid-side converter are thus calculated as:

$$I_{dg} = \frac{2}{3} \frac{P_{gsc} V_{ds} - Q_{gsc} V_{qs}}{V_{ds}^2 + V_{qs}^2}, \tag{4.16}$$

$$I_{qg} = \frac{2}{3} \frac{P_{gsc} V_{qs} + Q_{gsc} V_{ds}}{V_{ds}^2 + V_{qs}^2}. \tag{4.17}$$

Finally, the voltages of the grid-side converter are computed using:

$$V_{dg} = V_{ds} + R_{choke} I_{dg} - \omega_s L_{choke} I_{qg}, \tag{4.18}$$

$$V_{qg} = V_{qs} + R_{choke} I_{qg} + \omega_s L_{choke} I_{dg}. \tag{4.19}$$

The FCI method sets the initial voltages in the RSC V_{in-r} and GSC V_{in-g}, following the same principle proposed in [78], [84] and illustrated in Figure 4.3. The initialization sources, indicated by the blue line, are connected for the first time-point solution to set the initial voltage and phase magnitudes at the rotor and stator of the generator. After this, the dependent voltage sources $v_{r,x}$ and $v_{g,x}$ control the behavior of the wind turbine. For $v_{r,x}$ and $v_{g,x}$, x represents phases a, b, and c, derived from the reference rotor voltage v_r' and stator voltage v_s', which are obtained by transforming the vector domain references calculated by the control system into the phasor domain.

4.3.4 Controller Initialization

Since the voltages and currents of the induction machine have already been calculated, it is only necessary to configure the PI controllers using the backward propagation technique as proposed in

[14]. Each controller is assessed in the following subsections and represents the last subsection of the IA code, starting in section 4.

4.3.4.1 WPC initialization

The WPC's primary purpose is to control the WP's reactive power. This control is performed by a PI controller, which provides the reference voltage variation $\Delta v'$ of the q-frame GSC component to the outer control layer of the WT. The WPC controller configuration and its WTC connection are presented in Figure 4.1. In steady-state conditions, the output signal from the proportional term is zero, and a history term should be included in the integrator of the PI controller. The history term is calculated using backward propagation from the WTC outer control. First, the output of the WPC PI regulator ($\Delta v'$) is calculated by:

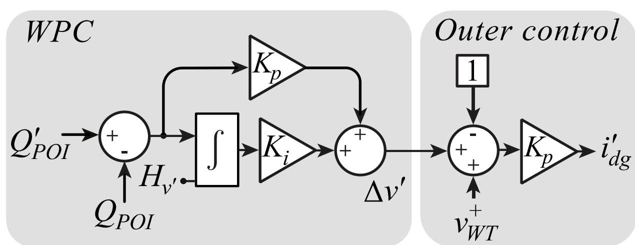

Figure 4.5 Wind park control initialization.

$$H_{v'} = \frac{\Delta v'}{k_i} \quad (4.20)$$

where $\Delta v'$ is calculated based on the measured voltage and the proportional constant of the voltage control.

$$\Delta v' = \left(\frac{i'_{qg}}{K_p} \right) - v^+_{WT} + 1 \quad (4.21)$$

4.3.4.2 GSC initialization

In steady-state conditions, the WP power generated matches the power supplied to the grid, resulting in the DC-link voltage achieving its nominal value. Consequently, the PI-controller integrator history term can be derived from the d-frame transformed three-phase current (i_{dg}) at the GSC side, assuming $i_{dg} = i'_{dg}$. Figure 4.6 illustrates the detailed block diagram of the v_{dc} outer control loop and the d-axis inner control loop. This control configuration ensures the dc bus voltage is set to its nominal value. The history term of the outer v_{dc} control loop $H_{v_{dc}}$ is calculated using (4.22). For the outer control, the q-axis is set to zero.

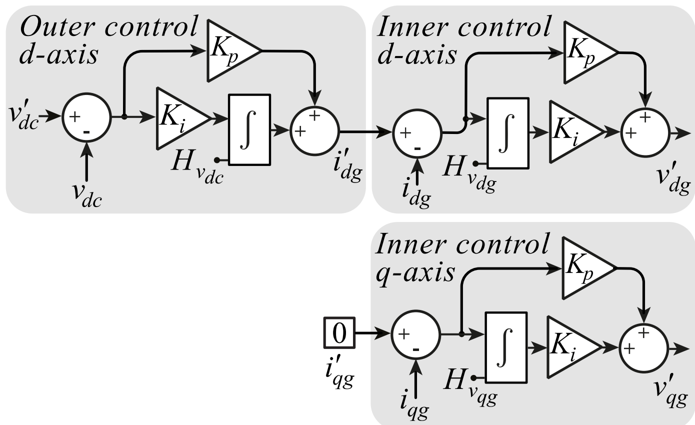

Figure 4.6 Grid side controller initialization.

Finally, the historical value of the three controllers can be calculated as:

$$H_{v_{dc}} = i'_{dg} \tag{4.22}$$

$$H_{v_{dg}} = v'_{dg} / K_i \tag{4.23}$$

$$H_{v_{qg}} = v'_{qg} / K_i \tag{4.24}$$

4.3.4.3 RSC initialization

For the RSC, the two-layer controllers need to be initialized. For the outer control, the d-axis is set to zero, while the q-axis depends on the mechanical model and the MPPT function and is calculated as discussed in [71]. Figure 4.7 shows the *d* and *q* branches of the MSC.

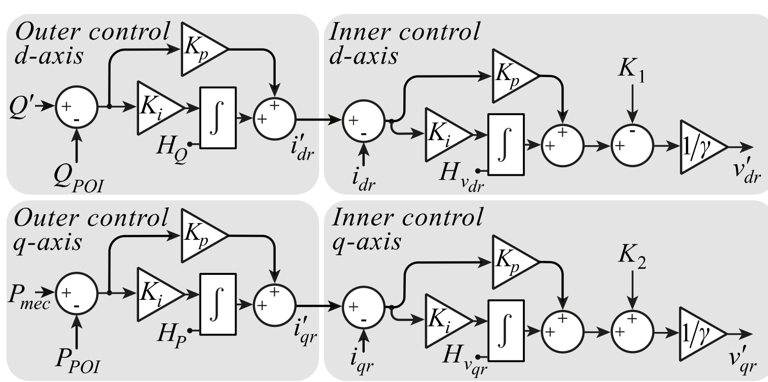

Figure 4.7 Rotor side controller initialization.

For the controller's external layer, the historical values are computed following the same criteria used for the GSC, using the estimated parameters obtained in the previous section of this chapter:

$$H_Q = i'_{dr} \tag{4.25}$$

$$H_P = i'_{qr} \tag{4.26}$$

In the case of the inner layer, the main difference compared to the GSC is the decoupling factors for the two branches. The history terms are given by

$$H_{v_{dr}} = \gamma v'_{dr} + K_1 \tag{4.27}$$

$$K_1 = s \times L_r \times i'_{qr} \tag{4.28}$$

$$H_{v_{qr}} = \gamma v'_{qr} + K_2 \tag{4.29}$$

$$K_2 = -s\left[\left(L_r + L_m\right)i'_{dr} + L_m i'_{dg}\right] \tag{4.30}$$

4.4 Comparison of methods for DFIG Park Initialization

This section presents a comparison of the proposed FCI method and the existing LFSI method.

To verify the effectiveness of the proposed FCI method, three power systems are simulated, each representing a different scenario of wind park integration:

- Test case 1: A small-scale system with one WP.
- Test case 2: A medium-scale system comprising ten WP models.
- Test case 3: A large-scale system includes 14 WPs and 19 PV models.

The simulations use a time-step of 50 µs for the AVM and 10 µs for the DM, as the DM includes the complete representation of the IGBT-bridge [9]. A system is considered to have reached steady-state when the P and Q waveform variations remain within a 1% tolerance band of the convergence value. All simulations are performed using EMTP® software [58] on an Intel i7-13800U 2.50 GHz processor. It is noted that the proposed method FCI is applicable to any other EMT-type software, where base conditions obtained from LF are known, and where the same control topology is open to be controlled.

4.4.1 Test case 1: 120 kV system with aggregated DFIG park model

The 120 kV/60 Hz EPRI benchmark system [68], which includes one WP, is simulated to evaluate the impact of individual DFIG park initialization. The topology of this system is depicted in Figure 4.8

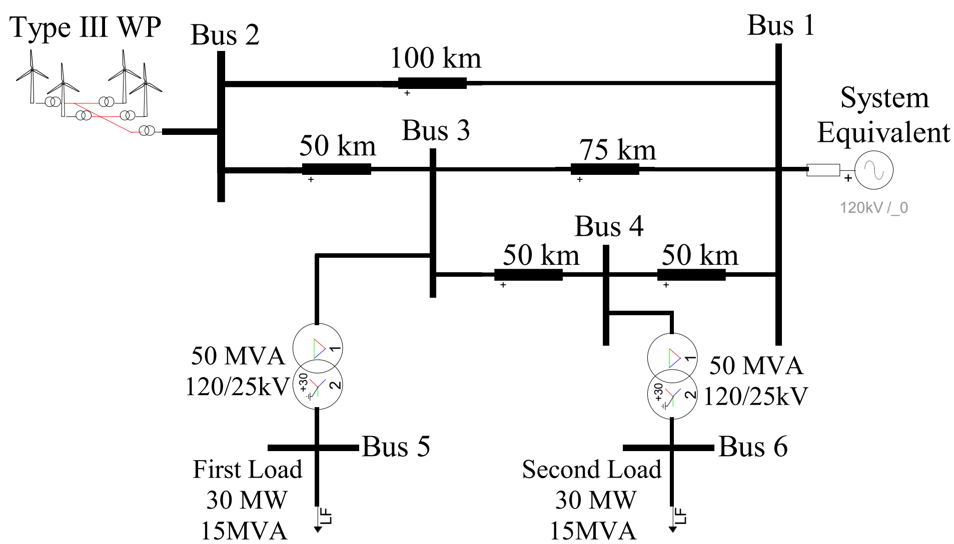

Figure 4.8 Test case 1: EPRI benchmark with aggregated WP.

As a baseline for comparison, the scenario with minimal initialization of the PLL and no controller initialization (NI) is illustrated in Figure 4.9. In this case, the required time to reach steady-state corresponds to 2.49 s for DM and 2.51 s for AVM. This time window is long, resulting in prolonged transient behaviors and increased computational cost. If the PLL is not initialized, the system will not be able to converge to a steady-state.

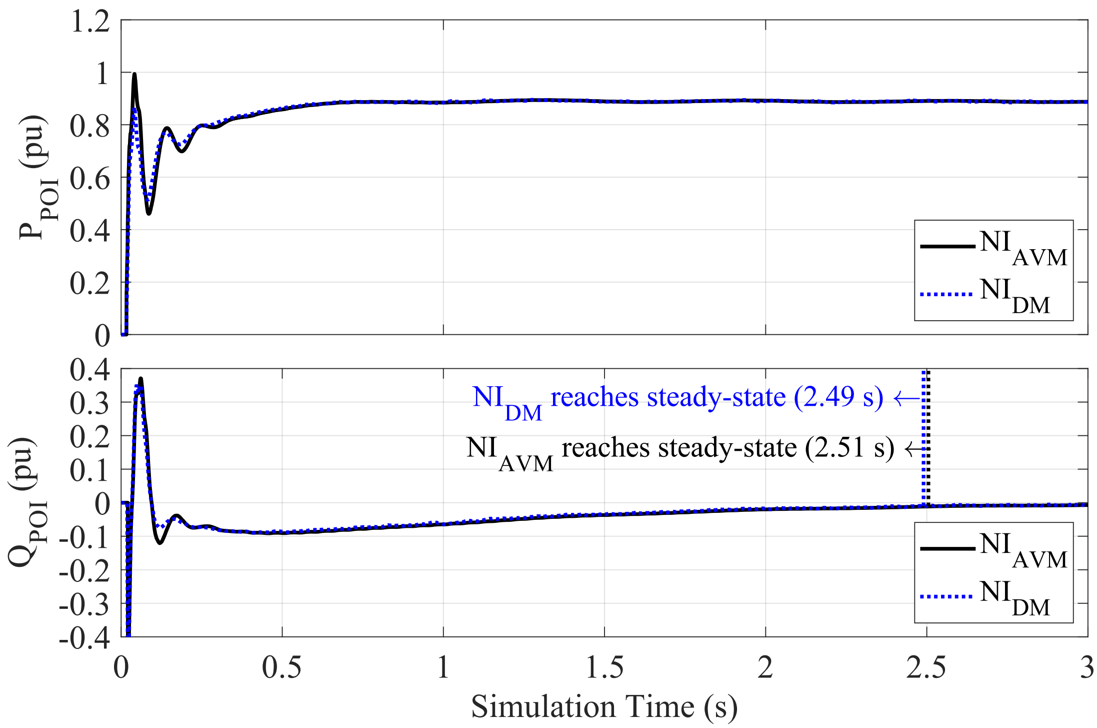

Figure 4.9 Test case 1, Average active and reactive powers at the POI for AVM and DM converters with no initialization.

Figure 4.10 present the average active and reactive power at the POI during the system's time-domain initialization, comparing the LFSI and DI methods.

Error! Reference source not found. compares the simulation time required to reach steady-state, along with the associated computation time.

In Figure 4.10, the internal behavior of the WP during LFSI initialization is presented for AVM models. The switching time of the ideal source is selected to reconnect the WP once the transient phenomena have sufficiently reduced, as observed at 0.5 s in test-case-1. The transient effect associated with LFSI-DFIG is notably larger than the DI, making the ideal source fundamental to maintaining the output power within the required margins.

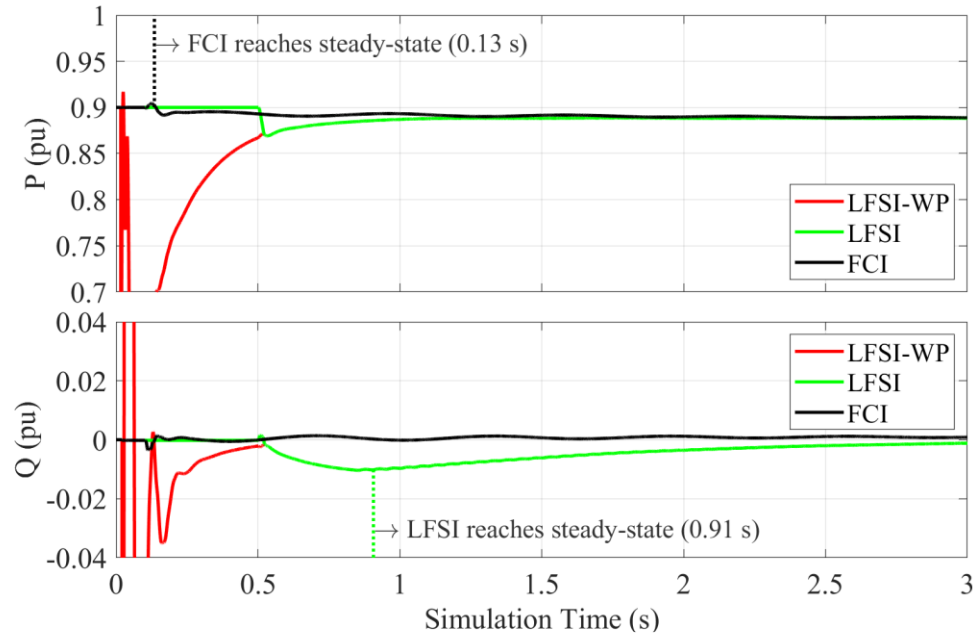

Figure 4.10 Average active and reactive powers measured at the POI of Figure 4.1, as given by the FCI and LFSI and using converter AVM for test case 1.

Table 4.1 Simulation data for test-case-1

Converter model	Initialization method	Initialization time (s)	Computation time (s)
AVM	NI	2.51	19.20
	LFSI	0.91	7.25
	FCI	0.13	1.80
DM	NI	2.49	94.77
	LFSI	0.91	34.99
	FCI	0.13	6.03

The results in **Error! Reference source not found.** show that, even for a comparably simple simulation case, the computational savings by the FCI approach are substantial, achieving gains of around 10 and 42 times for AVM and DM, respectively. However, looking at the absolute time savings, it becomes evident that a significant benefit for AVM simulations is not achieved unless very large parametric studies are conducted. For DM simulations, the savings are notable.

4.4.2 Test case 2: 400/154 kV system with multiple DFIG WPs

This test case is presented in [68]. Its single-line diagram is illustrated in Figure 4.11. The model represents a 400/154 kV network operating at 50 Hz and includes two configurations of WPs: 7 WPs each containing 35 WTs, and 3 WPs each with 50 WTs. All WPs operate in Q-mode with the reactive power reference set to zero.

The synchronous machine models incorporate control systems, including exciters and governors, as specified in [67]. Transmission lines are modeled using constant-parameter (CP) representations, while the sub-transmission network lines use PI-section models. Additionally, magnetic saturation in both transformers and synchronous machines is considered.

For detailed analysis, two aggregated wind parks, WP-A (35 WTs) and WP-B (50 WTs), are selected due to their different power generation capacities. The remaining WPs are modeled identically to WP-A and WP-B and do not offer further relevant insights; thus, their results are not discussed in detail. **Error! Reference source not found.** summarizes the initialization times for all WPs, where the maximum initialization time is used to calculate the computation time.

The NI method encountered convergence issues, failing to achieve steady-state values for both active and reactive powers. Figure 4.12 and Figure 4.13 show the active and reactive power profiles at the POI for WP-A and WP-B. The initialization time for WP-A using the LFSI method is 0.52 s, while the FCI method reduces it significantly to 0.21 s.

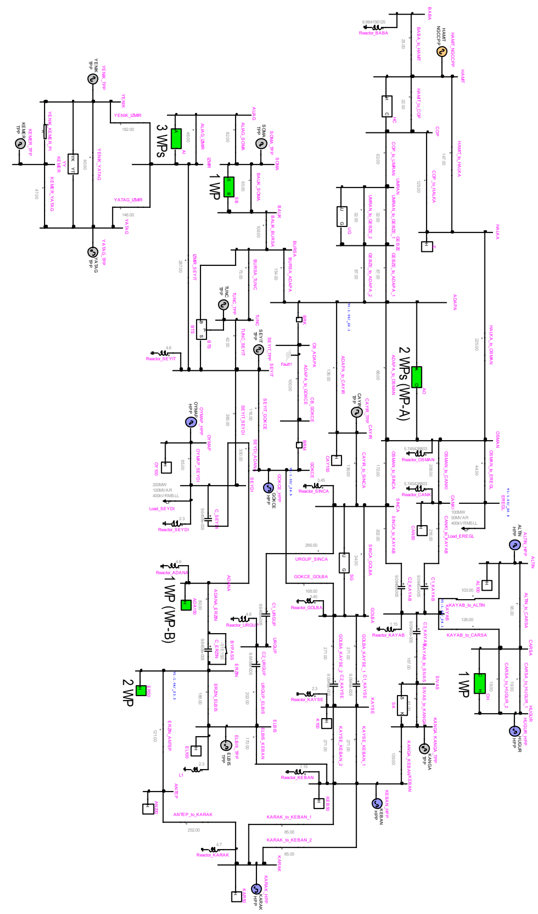

Figure 4.11 Test-case-2, single line diagram.

Table 4.2 Initialization time of wp for test-case-2

Wind Park Location	AVM		DM	
	LFSI	FCI	LFSI	FCI
ADA 150	0.53 s	0.18 s	0.5 s	0.20 s
AI 1	0.52 s	0.14 s	0.52 s	0.23 s
AI 2	0.52 s	0.24 s	0.52 s	0.21 s
AI 3	0.52 s	0.17 s	0.52 s	0.15 s
AO 1 (WP-A)	0.52 s	0.21 s	0.52 s	0.22 s
AO 2	0.57 s	0.13 s	0.52 s	0.02 s
CH 1	0.57 s	0.25 s	0.52 s	0.21 s
SB 1	0.57 s	0.19 s	0.52 s	0.03 s
ER50 1 (WP-B)	0.57 s	0.13 s	0.57 s	0.19 s
ER50 2	0.57 s	0.10 s	0.57 s	0.16 s
Computation time	61.93 s	20.42 s	2340.66 s	650.38 s

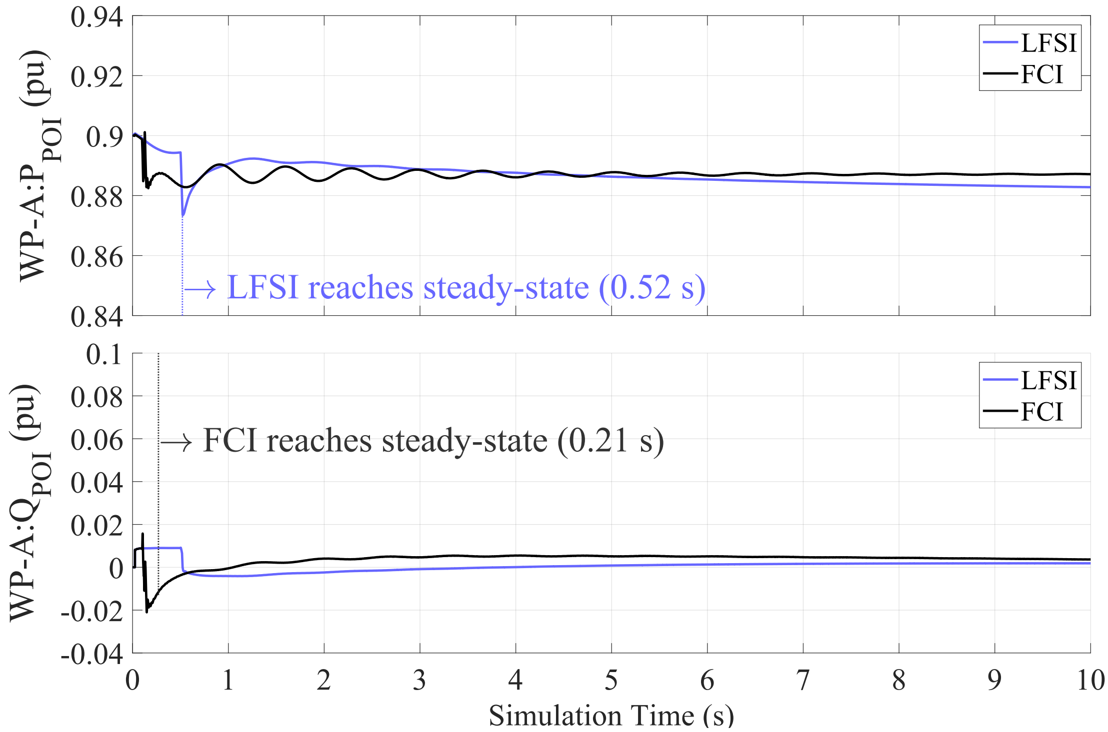

Figure 4.12 Average power in WP-A for test case 2.

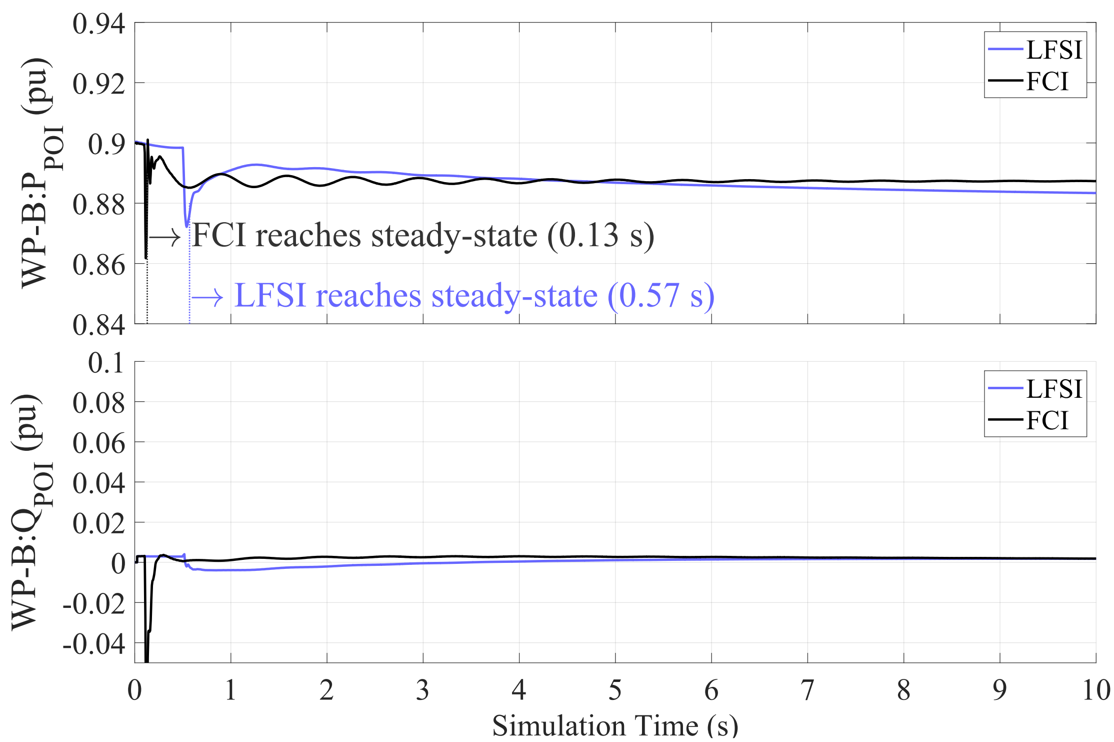

Figure 4.13 Average power in WP-B for test case 2.

4.4.3 Test case 3: WECC-240 test system

This system [85] is shown in Figure 4.14 and includes fourteen DFIG-based WPs and nineteen PV parks. In the version tested in this paper, the network incorporates PI-section transmission line models, synchronous machine exciters and governors, and transformer magnetic saturation, with all loads modeled as constant power. All simulations were performed on a single-core computational setup. In this paper, all models of the WPs are enhanced to include a full representation of the WT controllers with added WPC. Each WP operates at a distinct operating point, and the corresponding results are summarized in **Error! Reference source not found.**.

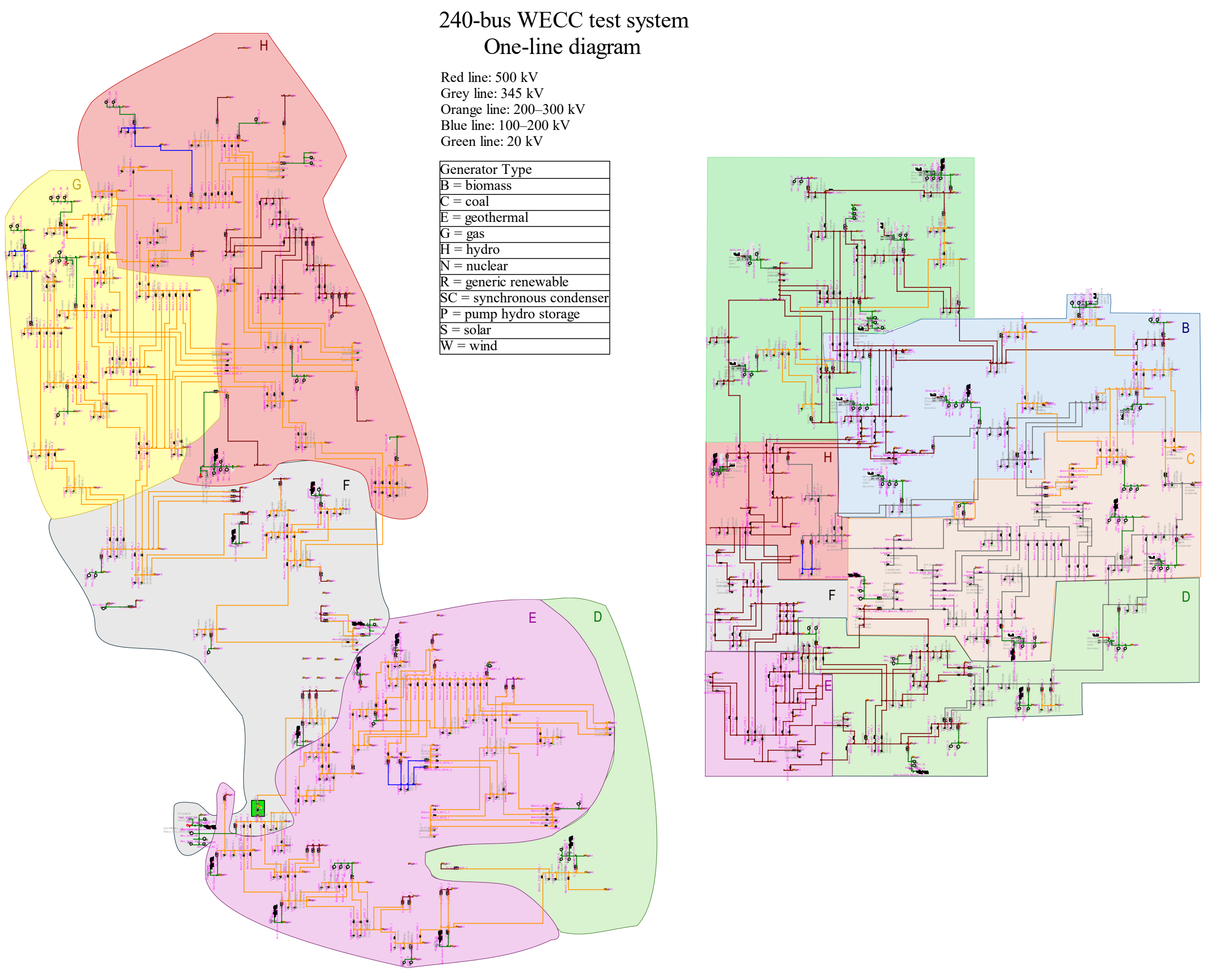

Figure 4.14 Test case 3, WECC-240 system schematic.

Table 4.3 Initialization time of wps parks for test case 3

Wind Park	AVM		DM	
	LFSI	FCI	LFSI	FCI
1034	0.52 s	0.19 s	0.52 s	0.29 s
4031 (WP-A)	0.52 s	0.18 s	0.52 s	0.28 s
4035	0.52 s	0.23 s	0.52 s	0.21 s
4039	0.52 s	0.21 s	0.52 s	0.15 s
4131	0.52 s	0.16 s	0.52 s	0.22 s
4132	0.51 s	0.11 s	0.51 s	0.02 s
4232	0.53 s	0.19 s	0.53 s	0.21 s
5032 (WP-B)	0.51 s	0.20 s	0.52 s	0.03 s
6132	0.52 s	0.25 s	0.52 s	0.19 s
6235	0.52 s	0.19 s	0.52 s	0.05 s
6333	0.52 s	0.16 s	0.52 s	0.11 s
6433	0.52 s	0.18 s	0.52 s	0.12 s
6533 (WP-C)	0.51 s	0.23 s	0.51 s	0.06 s
7031	0.52 s	0.22 s	0.52 s	0.16 s
Computation time	79.41 s	46.81 s	2340.66 s	650.38 s

Transmission lines are modeled using PI-section representations. The system also incorporates models for synchronous machine exciters, transformer magnetic saturation, and PV and WP full-control converters, which were included to improve the existing test case. All loads in the system are modeled as constant power loads.

The initializations of three WP, located at node 4031, 5032 and 6533, are studied in detail. These three WPs have been selected for their different power generation configurations. The results obtained from its simulation can be seen in Figure 4.15, Figure 4.16 and Figure 4.17. As the LFSI technique considers an ideal source during the first 0.5 s of simulation, the system transient behavior is dictated by the interaction of the ideal source with the surrounding components in the grid, as the sources are disconnected the real behavior of the DFIG is included, and that cause the jump in the curve at 0.52 s and the jump in the reactive power curve for all three studied WPs.

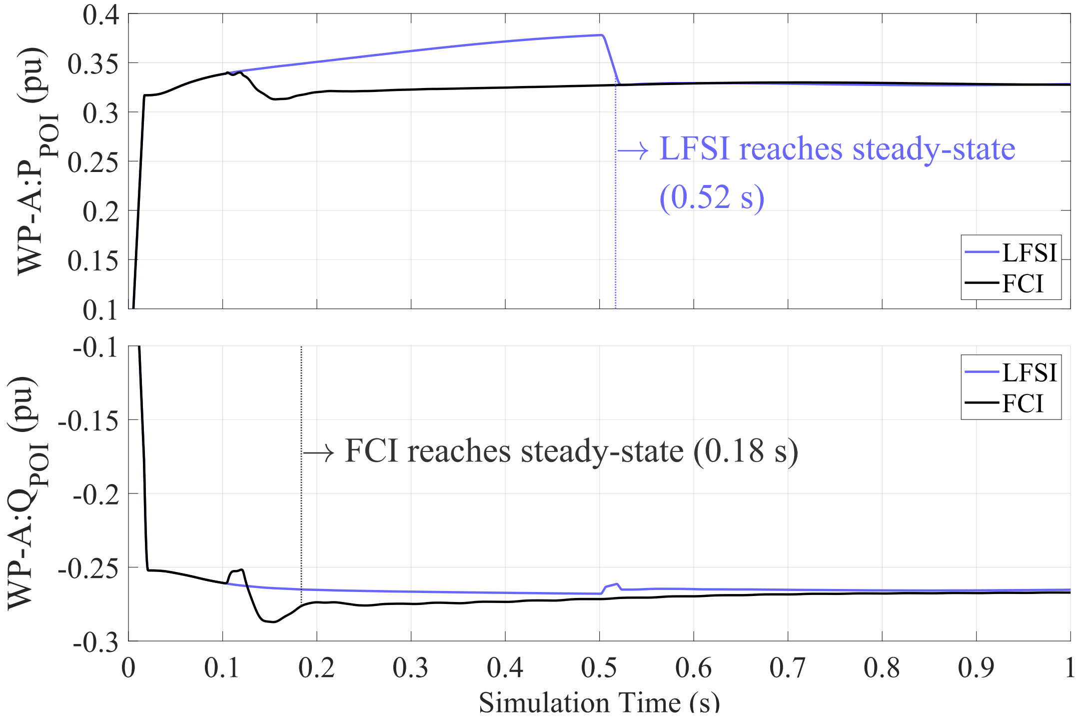

Figure 4.15 Average active and reactive powers at POI for WP 4031 for test case 3.

For WP-A, a 16.41 kW WP system is employed. The AVM simulation with LFSI requires 0.52 s to reach a steady-state with a corresponding computational time of 58.21 s. FCI permits to reach a steady-state at 0.18 s with a computational time of 27.31 s. As for the DM, LFSI requires 0.52 s with a computational time of 2340.66 s, while FCI requires 0.18 s and 985.25 s computational time, respectively. The comparison of the average active and reactive powers at the POIthe is shown in Figure 4.15.

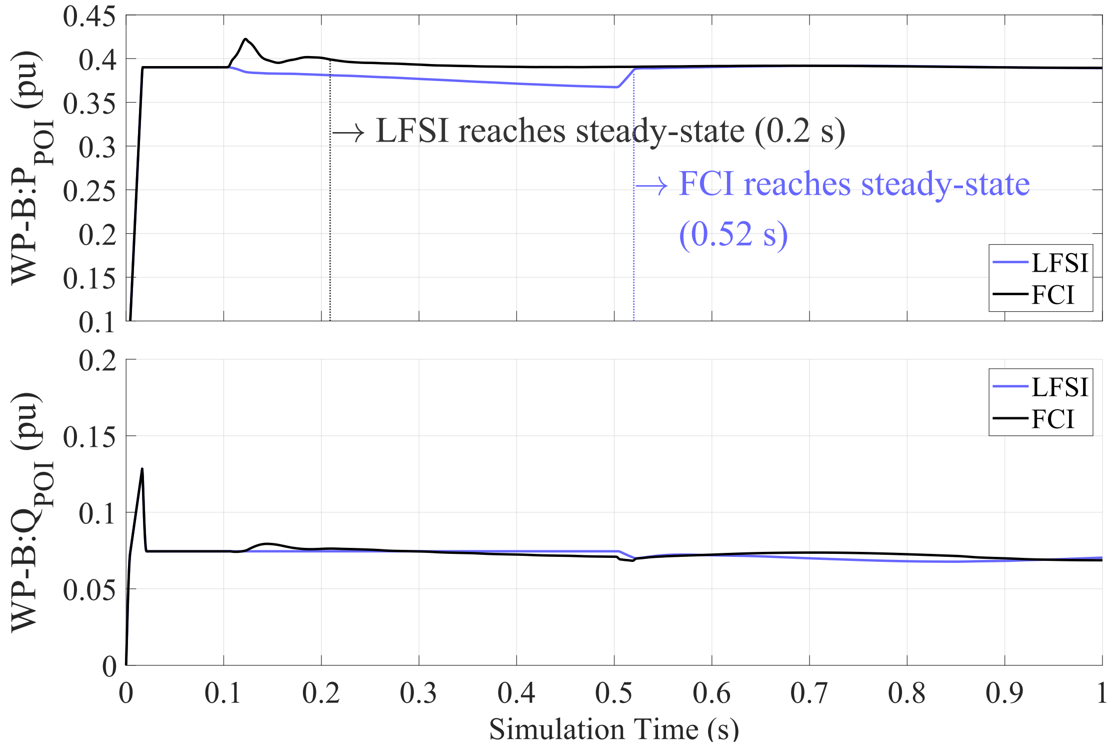

Figure 4.16 Average active and reactive powers at POI for WP 5032 for test case 3.

For the WP-B, a 23.44 kW WP system is employed. The AVM with LFSI takes 0.52 s to reach steady-state with a computation time of 58.21 s. In contrast, the FCI method attains a steady-state in just 0.2 s, corresponding to 17.44 s of computation time. For the DM, the LFSI method exhibits identical performance, with a steady-state time of 0.52 s and 2340.66 s of computation time and for the FCI, 0.2 s and 650.38 s, respectively, the power waveforms are shown in Figure 4.16.

Finally, Figure 4.17 shows the initialization time required for all fourteen WPs of test case 3, complementing the results presented in the previous figures and emphasizing the effectiveness of the proposed initialization method.

The largest initialization time for the LFSI occurs with WP-C. This is due to the interactions with the multiple synchonous generators.

For the AVM, the required simulation time and computation time are reduced by a factor of 1.5 and 1.9, respectively, when comparing FCI to LFSI. For the DM, the required simulation time and computation time are reduced by a factor of 1.4 and 3.6, respectively.

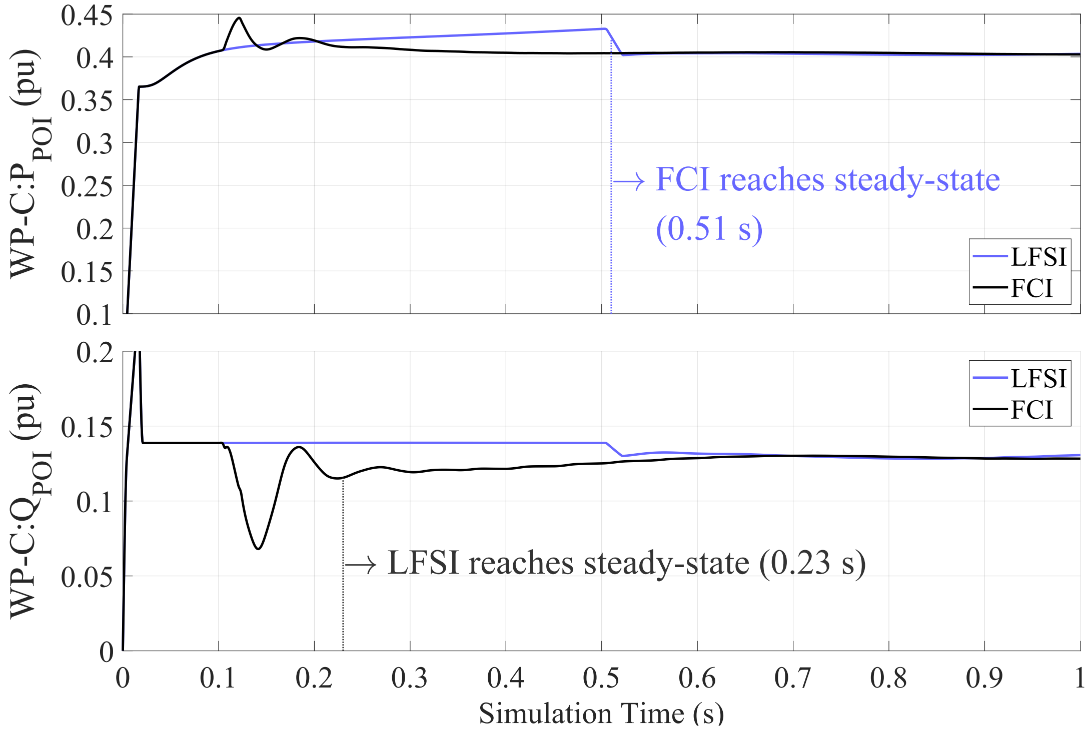

Figure 4.17 Average active and reactive power at POI for WP 6533 for test case 3.

4.5 Conclusion

This chapter proposes an enhanced steady-state initialization method named FCI for wind park EMT models. It is based on calculating initial control variables via backward propagation of the WP model controllers, measurement blocks, and the converter bridge. A detailed description of each controller component and its initialization procedure is provided, where the initialization values are generated from the WP model parameters and the load-flow solution. The proposed FCI method has demonstrated significant computational savings compared to an existing initialization method. It can be implemented in any EMT-type software where the same control topology is implemented and the LF constraints are calculated previous to the initialization process.

CHAPTER 5 INITIALIZATION OF PROPRIETARY IBR MODELS: GREY- AND BLACK-BOX APPLICATIONS

The initialization methods developed in the previous chapters rely on full access to the internal structure and parameters of the IBR. This level of transparency characterizes "white-box" models, where all mathematical equations, control topologies, and component parameters are fully visible to the user. While this assumption holds for open or generic models, it is not valid for manufacturer-provided equipment. To protect intellectual property, commercial wind and PV models are typically delivered as "grey-box" or "black-box" representations. A grey-box model provides partial visibility, where the general electrical and control topology might be known but specific controller gains or proprietary algorithms remain hidden. In a more drastic case, a black-box model completely obscures the internal structure, often delivering the device as compiled code where only the external terminals and reference setpoints are accessible. Because the internal equations, machine variables, and state information are partially or completely hidden in these proprietary models, the techniques presented earlier, which are based on the explicit reconstruction of internal steady-state conditions, cannot be applied directly.

In such proprietary models, the lack of visibility into internal states makes it impossible to compute steady-state currents, fluxes, mechanical variables, or controller integrator values from load-flow results. This often forces users to rely on time-domain run-up strategies, which are slow, may generate large artificial transients, and do not guarantee convergence to the intended operating point. The inability to efficiently initialize these models has become a major barrier to conducting EMT studies involving manufacturer-provided IBR.

To overcome these limitations, this chapter introduces a general initialization framework for grey- and black-box IBR models. The approach is based on a decoupling-style initialization philosophy combined with targeted external control guidance, allowing the device to settle naturally to its correct steady-state using only terminal-level quantities. This methodology requires no internal model access and is therefore applicable to a wide range of proprietary converter-interfaced resources.

The remainder of this chapter describes the structure of typical grey- or black-box models, presents the proposed initialization method, and demonstrates its effectiveness through case studies that compare its performance with existing initialization techniques.

5.1 Greybox and Blackbox Initialization Scheme

The proposed initialization technique follows the same general strategy as the FCI method, which was illustrated in Figure 5.1(a) and detailed in previous sections. However, in this proposed approach, the time-domain initialization is decomposed into multiple substages. The system is partitioned into independent components that are solved separately until their results converge, after which the complete system is reconnected, as depicted in Figure 5.1(b). A detailed description of the different stages of the time-domain initialization will be done in section 5.1.2.

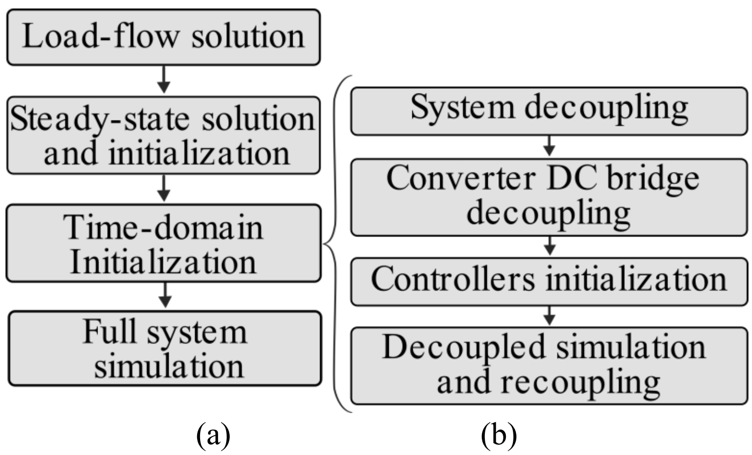

Figure 5.1 LF-based initialization steps: (a) the global procedure, (b) the proposed hybrid DI technique steps.

5.1.1 Overview of initialization burden in DFIG models

Although the structure of the DFIG wind park model has been previously described, the main objective of this section is to explore ways to simplify this structure. The goal is to initialize the minimum number of components necessary, thereby reducing the overall number of controlled variables.

The turbine mass model [65] is the slowest among the three, as it represents the mechanical dynamics of the generator. Its correct initialization is essential; errors can lead to torque-speed mismatch, prolonged transients, or even simulation failure. Fortunately, this loop is relatively straightforward. and is typically initialized reliably using steady-state (LF) values during Stage II.

The WPC governs the reactive power or voltage at the PCC. Acting as the master control loop of the WP, it defines the reactive power reference for the converter bridge controllers. Due to its supervisory role, the WPC has extremely slow dynamics and is often left uninitialized in stage II. Instead, it converges gradually during stage III through time-domain simulation. While this strategy is sufficient for small-scale or simplified systems, it often results in prolonged convergence times or instability in large-scale or detailed EMT models.

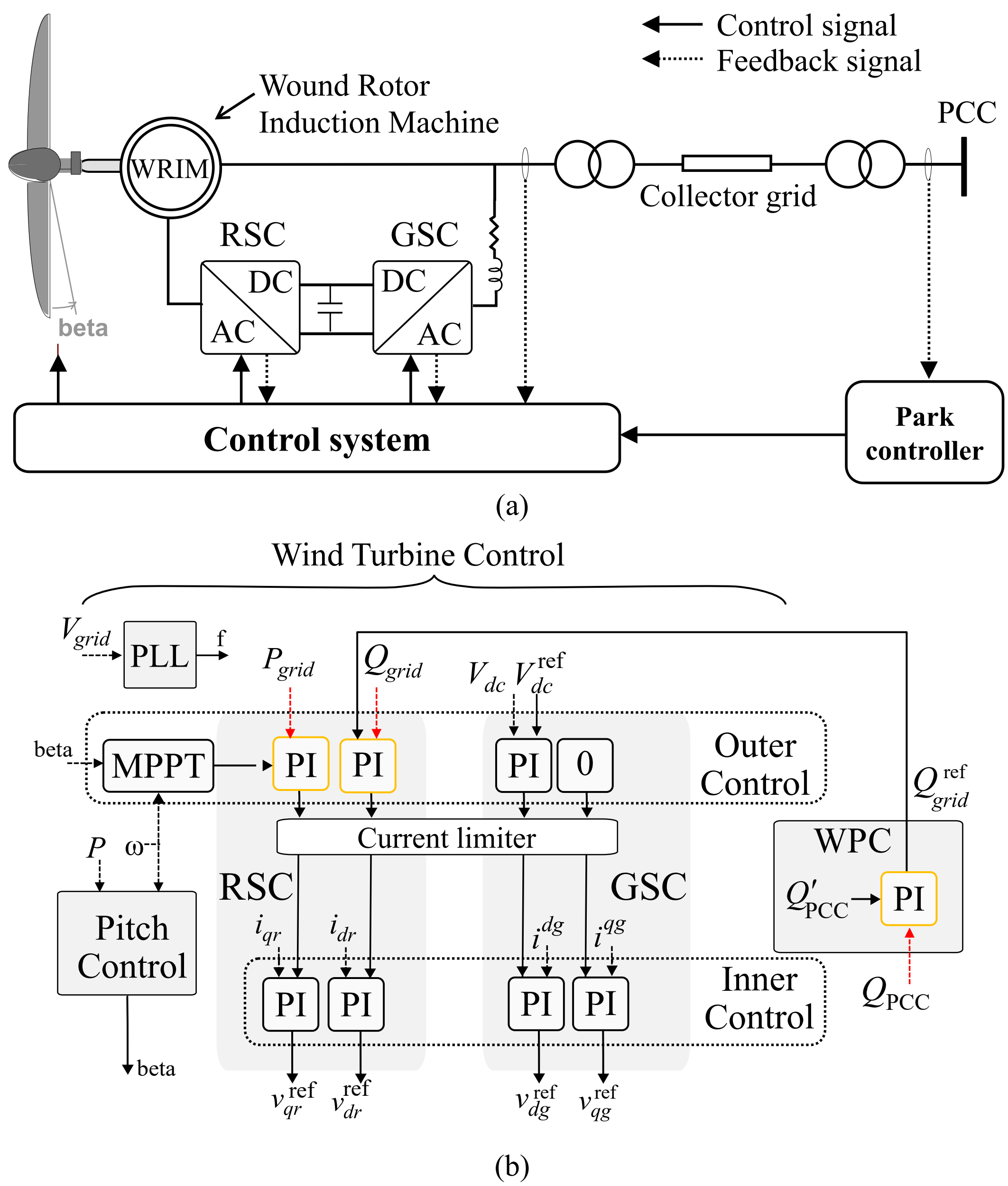

Figure 5.2 Aggregated DFIG WP model: (a) power system layout, (b) control system architecture.

The converter bridge control, comprising the RSC and GSC, poses the most significant initialization challenge. These controllers typically implement cascaded control loops, as shown in Figure 5.2 (b), each with different time constants:

- Inner current control loops (fastest),
- Outer loops for DC voltage, active power, or reactive power (intermediate),
- Synchronization modules, such as PLLs.

Precise coordination among these loops is essential for stable operation. As demonstrated later in this section, the proposed hybrid initialization approach mitigates this issue by eliminating the need to initialize each controller loop individually. Instead, it strategically combines partial steady-state initialization with selective decoupling, enabling a fast and stable startup even in detailed EMT models.

5.1.2 The proposed hybrid decoupling Interface (HDI) method

The proposed method consists of two main steps. First, the decoupled initialization (DI) technique presented in [86] is applied internally within the wind turbine model at selected locations. This technique creates independent subsystems that can reach steady-state independently and at an accelerated rate, utilizing a stable initial connection. When fully initialized, these subsystems are recoupled to ensure matching connection conditions. Second, a targeted steady-state initialization is performed for key control components to prevent incorrect behavior during startup; this process is presented in the following section.

5.1.2.1 Wind-turbine decoupling

As previously discussed, the converter bridge control is composed of multiple cascaded control loops (Figure 5.2 (b)), each with distinct time constants. These dynamic layers create significant challenges during initialization, particularly when interacting with the machine model.

To mitigate initialization transients, the DI method [86] is applied internally within the DFIG schematics. The proposed method employs a two-spot decoupling strategy to target the primary sources of interaction during startup.

- Spot 1 – AC-side decoupling at location A (Figure 5.3): The machine–converter block is first isolated from the rest of the power system by inserting a DI block at location A. At this point, an AC DI block is used with P and Q constraints, as described in [86]. This confines the initialization process to a localized segment, preventing dynamic interaction between the machine–converter set and the external grid.

- Spot 2 – (Optional) DC-side decoupling at location B (not used in this work): The coupling between the machine and the converter bridge is the second source of transients. A DI decoupling is inserted at location B, applied across the DC link to address this. In this setup, the RSC and GSC are treated as two separate converters, one constrained with P_{dc} and the other with V_{dc}. Each converter is decoupled using a standard DI block, as outlined in [86]. This can be used in cases where The internal behavior of the machine is causing initialization problems. In cases where the DI at the point of connection is enough to guarantee steady-state this can be avoided to reduce complexity in the initialization process.

In this specific configuration (special case), the two DC DI blocks are directly connected, without any intervening lines or components. Thus, the dependent sources mimic the behavior of the independent ones. To simplify the setup, the dependent sources can be removed entirely and replaced with independent ones. This yields a simplified schematic, as shown in Figure 5.4, which is applicable in this special case. By decoupling at location B, the RSC is seen as part of the rotor, while the GSC can be seen as a shunt-connected converter.

However, according to the test cases, both the RSC and GSC were fast enough that decoupling at location B had no measurable impact. Thus, decoupling at location B is offered as an optional step for systems where the RSC or GSC exhibits slow dynamics. This methodology is not employed in the current work to maintain simplicity.

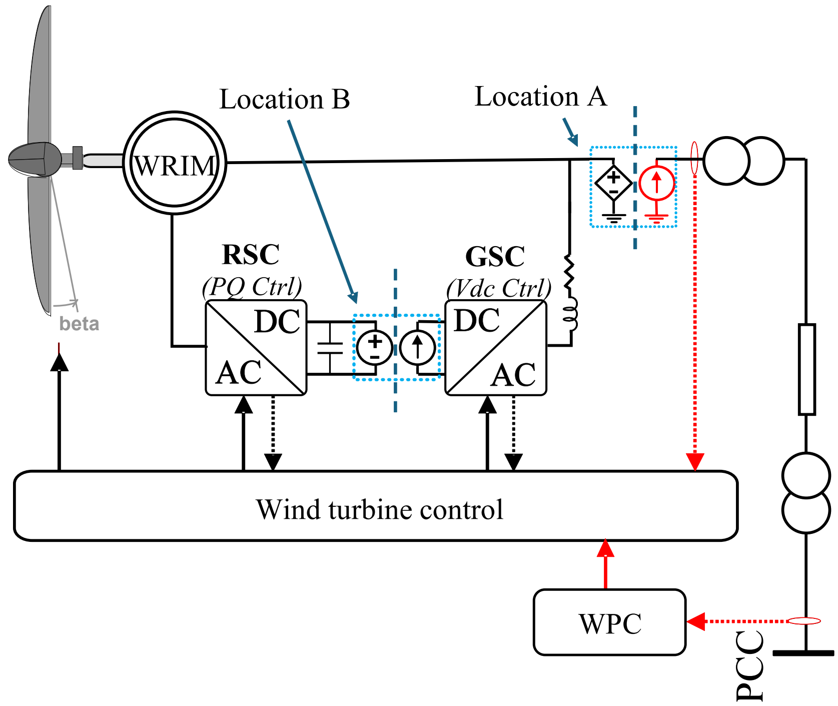

Figure 5.3 The proposed decoupling locations within the DFIG model.

5.1.2.2 Other considerations

Applying the DI technique internally, as described above, effectively suppresses sources of initialization transients. However, the DI method was originally designed for black-box models, where it is typically applied only at the PCC. This restriction stems from the requirement that the entire control system must remain within the initialization framework, referred to as the Time-Domain Initialized Subsystem (TDIS) in [86].

If control elements are located within the initialized part of the DI block, called the Initialized Subsystem (ISS) [86], a critical limitation arises. Specifically, when a controller's feedback signal is sourced from within the ISS, it becomes identical to its setpoint, resulting in a zero-error signal. This condition effectively "freezes" the controller output at an incorrect value, preventing the control loop from functioning as intended [86].

In our case, internal application of the DI method results in some feedback signals falling within the ISS, as illustrated in Figure 5.3. In particular, at location A, the initialized region includes feedback paths (highlighted in red) that belong to active control loops. Their presence within the ISS corrupts the initialization of the associated controllers. Figure 5.2 (b) highlights the three affected PI controllers, which are:

- The WPC,
- The outer active power controller of the RSC
- The outer reactive power controller of the RSC.

These controllers rely on fixed feedback signals during initialization, preventing them from responding as intended. In other words, this setup disables both the WPC and the outer loops of the RSC controller during the initialization phase.

To overcome this issue, we propose a hybrid DI approach that incorporates a partial steady-state calculation to support the correct initialization of these vulnerable controllers. This method restores proper control behavior without requiring full time-domain convergence. The technical details of this hybrid strategy are presented in the following section.

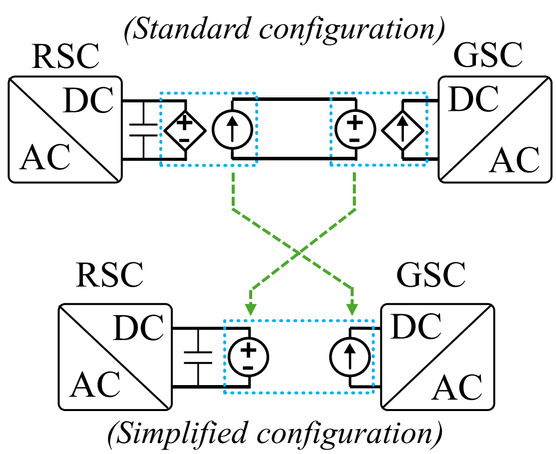

Figure 5.4 Simplifying the DI's decoupling configuration in the DFIG converter bridge.

5.1.3 Partial steady-state control initialization

This section presents simplified initial condition calculations for selected controllers. Here, the focus is on simplified and approximated initialization, as any small discrepancies are expected to be corrected during the subsequent time-domain simulation.

The targeted control modules are the controllers whose feedback signals reside within the Initialized Subsystem (ISS) and are thus prone to freezing when the DI method is applied internally. In this work, only three controllers meet this criterion: the WP controller and the RSC's outer active and reactive power controllers, since the steady-state initialization is applied only to a subset of the WP controller loops.

5.1.3.1 WPC

The WPC, shown in Figure 5.2 (b), requires explicit initialization, as it receives Q_{PCC} as a feedback signal from the PCC. By inserting a decoupling interface at location A in Figure 5.2.(a), the PCC becomes part of the ISS created by the red current source.

The WPC regulates the reactive power exchanged at the PCC by computing a reactive power reference for the stator side of each DFIG unit. To initialize this controller, the reference output must be set to match the stator's steady-state reactive power, which is derived from the LF solution:

$$H_{WP} = Qs \tag{5.1}$$

Where the stator's reactive power is directly retrieved from the LF solution.

5.1.3.2 RSC outer control *q*-axis channel

The q-axis of the RSC controller, shown in Figure 5.2 (b), regulates the grid-side active power (P_{grid}) by computing the reference value of the rotor q-axis current (I_{qR}^{ref}). Consequently, this PI controller can be initialized by determining the steady-state value of I_{qR}^{ref} .

Since the control is based on vector-oriented principles, the active power injected by the rotor side of the machine (P_R) can be written as:

$$P_R = -V_{qR} I_{qR} \tag{5.2}$$

All quantities are expressed hereafter in per-unit (pu). Under steady-state conditions, the reference current can be set equal to the actual rotor q-axis current:

$$I_{qR}^{ref} = I_{qR} = -\frac{P_R}{V_{qR}} \tag{5.3}$$

Using the generic DFIG relationships from [87], the rotor active power can be expressed as a function of the grid-side power P_{grid} :

$$P_R = -sP_s \tag{5.4}$$

where s denotes the machine's slip. The stator-side active power is expressed as:

$$P_s = \frac{P_{grid}}{1-s} \tag{5.5}$$

Substituting (5.4) and (5.5) into (5.3) gives:

$$P_R = \frac{-sP_{grid}}{1-s} \tag{5.6}$$

To simplify the expression, we approximate $V_{qR} \approx sV_s$ in steady-state, valid when rotor quantities are referred to the stator side. Then (5.3) can be substituted in (5.6) and rewritten in terms of I_{qR}^{ref} as:

$$H_{RSCq} = I_{qR}^{ref} = \frac{P_{grid}}{V_s\left(1-s\right)} \tag{5.7}$$

Where H_{RSCq} represents the initial value that should be set to the PI controller. Note that this approximation assumes all rotor quantities are referred to the stator side.

5.1.3.3 RSC outer control *d*-axis channel

The d-channel of the RSC controls the reactive power at the grid side (Q_{grid}). The outer control of this channel finds the reference value of the rotor d-axis current (I_{dR}^{ref}). Consequently, this PI controller can be initialized by determining the steady-state value of I_{dR}^{ref} .This formula is derived in [65] as

$$Q_s = \left(\frac{\omega\lambda_{ds}}{L_{ls}+L_M}\right)\left(\lambda_{ds} - L_m I_{dR}\right) \tag{5.8}$$

In steady-state, all machine variables in this formula are time-invariant [65] and can be written as:

$$Q_s = K_1 + K_2 I_{dR}^{ref} \tag{5.9}$$

where K_1 and K_2 are constants. More details can be found in [65]. Finally, the initial condition of the PI controller can be written as:

$$H_{RSCd} = I_{dR}^{ref} = K_3 + K_4 Q_s \tag{5.10}$$

These machine constants can be either calculated using (5.8) or can be obtained practically by a simple test.

5.1.4 Performance evaluation

This section evaluates the performance of the proposed initialization method by comparing it to a conventional LF-based initialization approach used as a baseline. The comparison focuses on two key aspects:

- The time required to reach steady-state convergence,
- The total simulation runtime.

To assess the effectiveness of the proposed method, two test cases were considered based on the EPRI system previously presented in Figure 3.10:

- Test case 1: A simplified WP system using an aggregated DFIG model.
- Test case 2: A large-scale WP composed of 45 individual DFIG units grouped into three feeders.

Table 5.1 Simulation and model details for test cases 1 and 2

Simulation detail/ model	**Test case 1**	**Test case 2**
WP model	Aggregated WP	Detailed WP
Control structure	Detailed controller for aggregated turbine	Individual control system per wind turbine
Collector system	Aggregated equivalent PI-line	detailed system using PI-lines (Figure 5.6)
Simulation nodes	12	122
Control devices	122	12121
Time-step (µs)	50	
Electrical source model	Voltage sources with impedance	
Transmission line model	Wideband [88]	
Simulation interval	Until steady-state is reached (1% criteria)	

In both cases, the simulations are conducted using the EMTP® software [58], with an AVM for converters. The simulations use a 50 µs time-step, and a steady-state condition is defined as the point at which waveform variations remain within 1% of the LF reference values. All cases are executed on an Intel(R) Core(TM) i7-13800H processor, ensuring consistent computational conditions for performance comparison.

Further simulation and modeling details, including the number of nodes, control devices, and model configurations, are summarized in **Error! Reference source not found.**.

5.1.4.1 Test case 1: 120 kV system with aggregated DFIG park model

The 120 kV/60 Hz EPRI benchmark system, using an aggregated DFIG WP model, is simulated to study the independent impact of initialization strategies on simplified models. Its topology is shown in Figure 3.10. In the baseline LFSI method, an auxiliary source is connected at the PCC during the early stage of simulation and disconnected at t = 0.5 s. In contrast, all auxiliary sources are removed earlier in the proposed HDI method, with the recoupling process triggered at t = 0.15 s.

Figure 5.5 presents the active and reactive power at the POI under both initialization strategies. For LFSI, with the same measurement points shown in Figure 4.1, two curves are shown:

- LFSI_External: the power measured at the POI (including the auxiliary injection),
- LFSI_WP Internal: the internal power collected by the DFIG model itself.

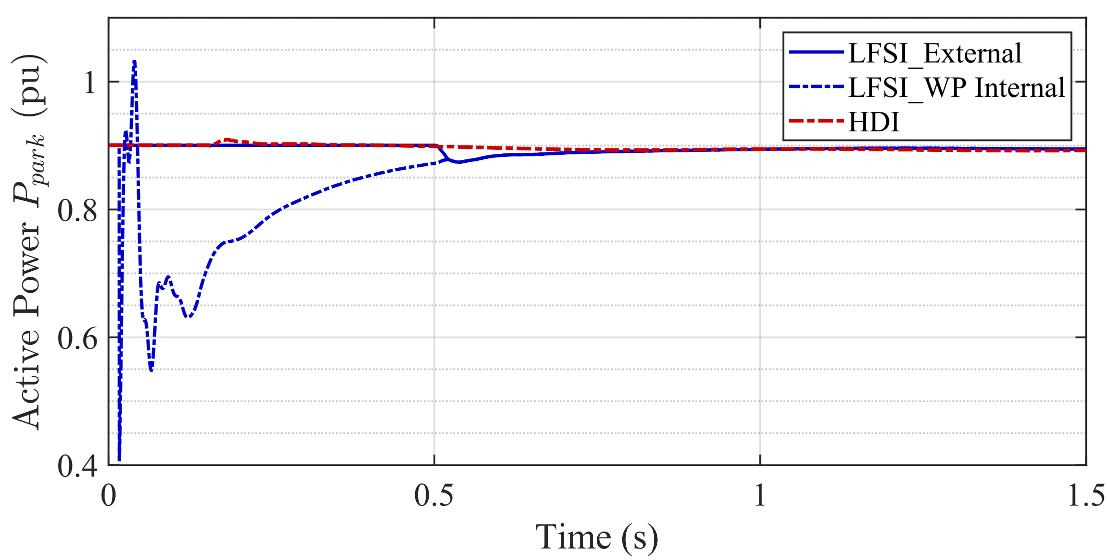

(a)

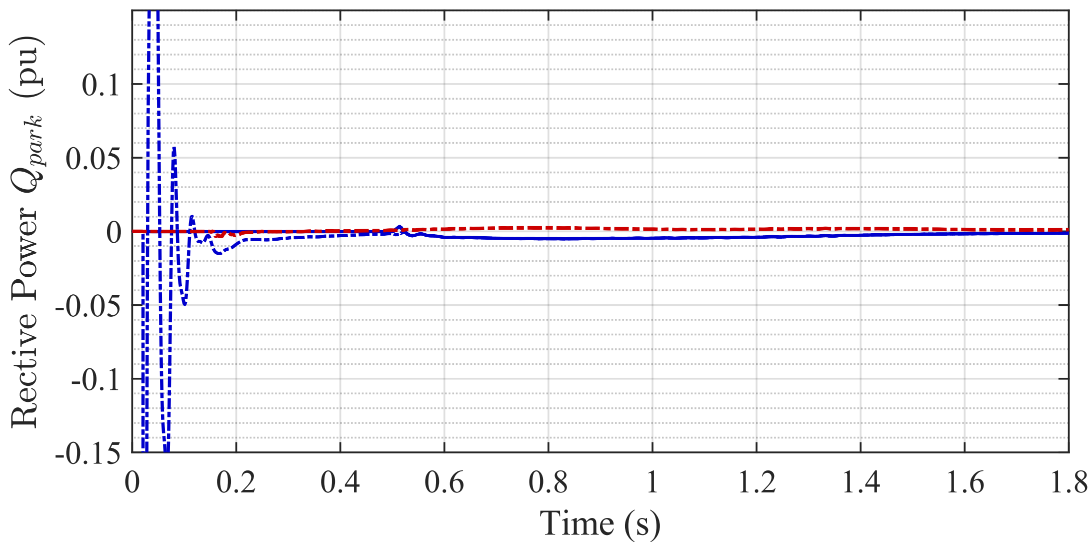

(b)

Figure 5.5 Park-level performance for test case 1: (a) active power at the PCC, (b) reactive power at the PCC, comparing LFSI and HDI initialization.

The times to reach steady-state are 0.65 s and 0.15 s for LFSI and HDI, respectively, corresponding to 3.76 s and 0.92 s of computational time. From an EMT simulation perspective, the proposed HDI method achieves a four-fold reduction in computational cost compared to LFSI. These results highlight the effectiveness of the proposed initialization strategy in improving simulation efficiency while maintaining stability. A summary of this comparison is provided in **Error! Reference source not found.**.

5.1.4.2 Test case 2: 120 kV system with detailed DFIG park model

This test case evaluates the proposed initialization strategy on a fully detailed DFIG WP model. The system comprises 45 individual DFIG units, connected to the PCC transformer through three feeders containing 18, 12, and 15 turbines, respectively. The layout of the WP, including the internal feeder configuration and transformer connections, is shown in Figure 3.13 and Figure 3.14.

In both the LFSI and proposed HDI methods, initialization is applied individually to each wind turbine, ensuring full electrical decoupling and preventing machine-to-machine interactions during startup. However, the two methods differ fundamentally in how they handle the initialization of internal controller states, particularly in DFIG outer loops responsible for regulating active and reactive power.

The impact of these differences can be observed at the feeder and WP levels. Figure 5.6 presents the initialization performance for each feeder, showing the active and reactive power response under both methods. Notably, both LFSI and HDI start from the same steady-state operating point, consistent with the LF solution. However, in the LFSI case, once the auxiliary sources are disconnected at $t = 0.5\ s$, the effects of improper controller initialization begin to surface. The absence of pre-initialized values for the WP and the d-axis current references within each DFIG leads to control mismatches and uncoordinated responses across feeders.

Each feeder exhibits distinct reactive power transients under LFSI, ranging from steep overshoots to prolonged drifts, as the controllers attempt to recover and stabilize in the time-domain. These discrepancies are especially amplified in feeders located farther from the PCC, where the electrical distance further challenges the system's ability to self-correct.

In contrast, the HDI method, through its partial steady-state initialization, ensures consistent internal control states from the outset. As a result, all feeders exhibit fast, coordinated, and smooth convergence of reactive power, regardless of their location in the network.

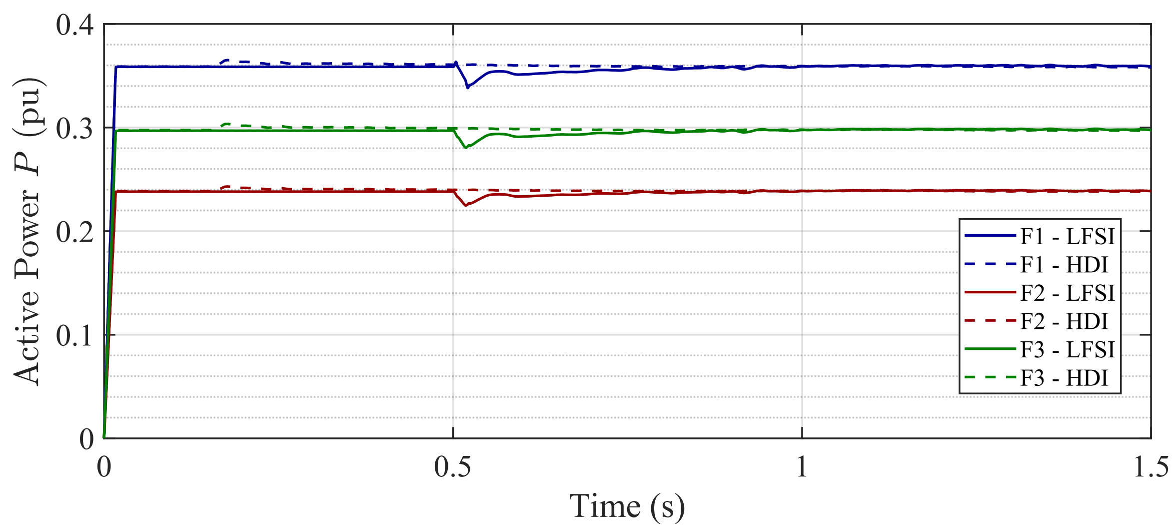

CP(a)

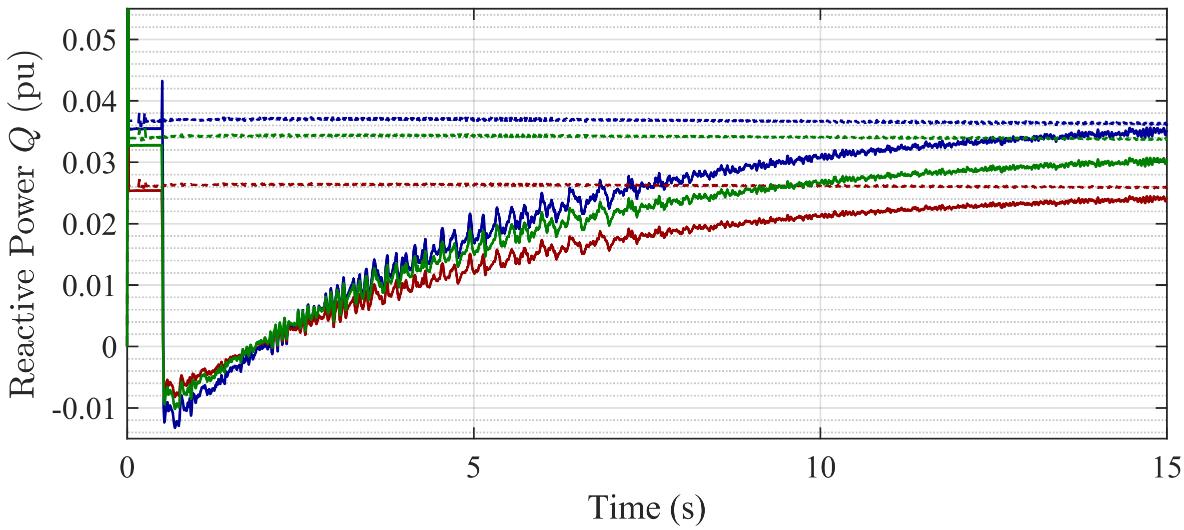

(b)

Figure 5.6 Feeder-level performance for test case 2: (a) active power, (b) reactive power at the three feeders, comparing LFSI and HDI methods.

Figure 5.7 illustrates the overall system response. Subfigure (a) shows the total active and reactive power at the PCC under both initialization methods, with the response consistent with the behavior observed in the aggregated test case (test case 1). Subfigure (b) highlights a more pronounced difference in reactive power convergence. Under LFSI, the response is characterized by delayed settling exceeding 12 seconds, accompanied by visible oscillations and slow ramping. This slow response is due to improper initialization of the d-axis current controllers and the WPC. While the initial conditions were consistent with the LF solution, the absence of correctly initialized control states causes reactive power to deviate significantly as the system evolves dynamically.

In contrast, the HDI method ensures stable operation, matching the behavior of the aggregated system, and reaches steady-state within a 0.15-second simulation interval. As summarized in **Error! Reference source not found.**, the CPU times corresponding to these initialization intervals are 6760 s and 78.6 s for LFSI and HDI, respectively, representing a nearly 100× improvement in computational efficiency.

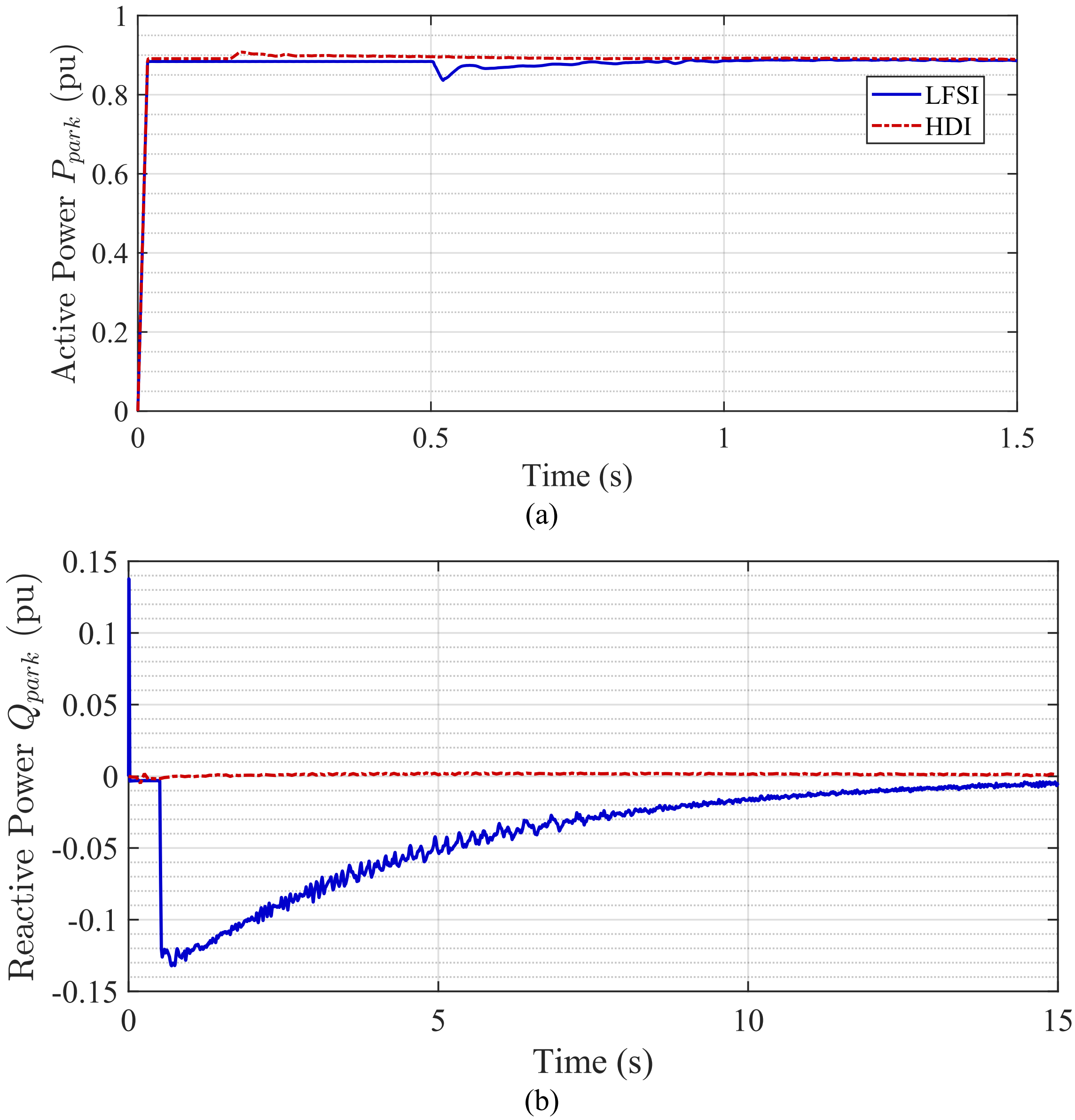

Figure 5.7 Park-level performance for test case 2: (a) active power at the PCC, (b) reactive power at the PCC, comparing LFSI and HDI initialization.

Table 5.2 Comparison of LFSI and HDI initialization methods from a computational perspective

Test Case	Initialization method	Initialization time(s)	Computation time (s)
1	LFSI	0.65	3.76
	HDI	0.15	0.92
2	LFSI	12.67	6760 (≈1.87 hours)
	HDI	0.15	78.6 (≈1.3 minute)

5.1.4.3 Conclusion

This chapter presented a hybrid initialization method for DFIG-based WPs, combining decoupling interfaces with partial steady-state control initialization. The approach specifically targets controllers affected by internal DI application, including the WPC and the outer loops of the RSC. By selectively initializing key PI controllers and applying DI only at critical points, the proposed method achieves fast and stable simulation startup.

Case studies demonstrated that the hybrid method significantly improves initialization accuracy and reduces computational burden. In aggregated and detailed test systems, the method consistently reduced the simulation interval required to reach steady-state and achieved up to 100-fold reduction in computational time compared to traditional LFSI. The results confirm that the proposed strategy offers a robust, scalable solution for initializing large-scale WP EMT models.

CHAPTER 6 CONCLUSION

6.1 Thesis summary

This dissertation has addressed the critical challenge of initializing EMT simulations for modern power systems dominated by IBR. As power grids transition toward high penetrations of renewable energy, the traditional "run-up" initialization methods have proven computationally prohibitive and prone to introducing artificial transients that compromise simulation accuracy.

The primary contribution of this research is the development of a comprehensive, modular initialization framework. This framework is divided into two distinct methodologies:

1. **Full Control Initialization (FCI):** A white-box approach that mathematically reconstructs the steady-state variables of all internal subsystems—including mechanical dynamics, converter bridges, and hierarchical control loops—derived directly from the load-flow solution.
2. **Hybrid Decoupling Interface (HDI):** A novel approach for proprietary (grey- and black-box) models that combines external decoupling with partial steady-state estimation to enable fast initialization without requiring access to internal control logic.

These methodologies were successfully applied to PV parks, FSC wind parks, and DFIG wind parks, demonstrating that accurate initialization is not merely a convenience but a fundamental requirement for efficient large-scale EMT studies.

6.2 Main Findings

The research reached significant findings across the specific technologies investigated:

Photovoltaic Parks: The FCI method proved that backward propagation of control variables eliminates the need for the system to "settle" in the time-domain. Validated against IEEE benchmarks, the method reduced the computation time required to reach steady-state by a factor of approximately 2 for both AVM and DM. It ensured that the simulation started with correct current and voltage references at the first time-step, effectively suppressing initialization transients.

Full-Scale Converter Wind Parks: The research highlighted that initialization must extend beyond electrical parameters to include the mechanical subsystem. By initializing the turbine speed, torque, and pitch angle alongside the electrical controls, the FCI method achieved a 90%

reduction in computation time compared to existing methods. For complex scenarios involving detailed wind park models, simulation time for initialization transients was reduced from over 90 minutes (non-initialized) to under 2 minutes.

DFIG Wind Parks: The DFIG model presented the most complex challenge due to the magnetic and algebraic coupling between the stator, rotor, and converter. The dissertation demonstrated that a unified initialization of the induction machine and the back-to-back converter is essential. The proposed FCI method successfully aligned all subsystems with the load-flow setpoints, ensuring numerical robustness and significant computational savings even for large-scale systems with multiple DFIG units.

Proprietary Models: A key finding was that complete internal access is not strictly necessary for efficient initialization. The HDI method demonstrated that strategically isolating the device at the PCC and estimating key outer-loop control states allows proprietary models to settle rapidly. This approach achieved up to a 100-fold reduction in computational time compared to traditional methods, offering a practical solution for industrial studies involving manufacturer-supplied black-box models.

6.3 Future Work

While this dissertation provides a robust framework for IBR initialization, several lines of research for future work remain to further enhance EMT simulation capabilities:

- **Simplified IBR Models for Fast Simulation:** Future research should focus on the development of reduced-order models that retain essential dynamic characteristics while being optimized for accelerated initialization. This is particularly critical for maintaining computational efficiency when simulating ultra-large-scale grids.
- **Standardized WECC Model Initialization:** Adapting the FCI framework specifically for WECC models would facilitate the rapid evaluation of established commercial benchmarks. This adaptation would bridge the gap between academic frameworks and industry-standard models, further reducing setup overhead for large-system studies.
- **Expansion to Grid-Forming (GFM) Converters:** Future efforts should extend the current initialization strategies to include Grid-Forming control architectures. Implementing these into standard benchmarks will involve addressing the unique steady-state requirements of

GFM converters—such as internal voltage magnitude and phase angle synchronization—to ensure stability in low-inertia grid scenarios.

REFERENCES

[1] International Energy Agency (IEA), *Renewables 2025: Analysis and forecast to 2030*, Paris, France: IEA, Oct. 2024. [Online]. Available: https://iea.blob.core.windows.net/assets/76ad6eac-2aa6-4c55-9a55-b8dc0dba9f9e/Renewables2025.pdf. [Accessed: Oct. 29, 2025].

[2] P. Christensen, G. K. Andersen, M. Seidel, S. Bolik, S. Engelken, T. Knueppel, A. Krontiris, K. Wuerflinger, T. Bülo, and J. Jahn, "High penetration of power electronic interfaced power sources and the potential contribution of grid forming converters," 2020.

[3] L. Yang, Z. Xu, J. Østergaard, Z. Y. Dong and K. P. Wong, "Advanced Control Strategy of DFIG Wind Turbines for Power System Fault Ride Through," *IEEE Trans. Power Systems*, vol. 27, no. 2, pp. 713-722, May 2012. doi: 10.1109/TPWRS.2011.2174387.

[4] Y. Yang, G. Mao, & Z. Zhou, "Enhanced Control Strategies for Improving Low-Fault Ride-Through Capability of Grid-Connected Doubly Fed Induction Wind Turbines," *Energies*, vol. 18, no. 4, p. 767, 2025. doi: 10.3390/en18040767.

[5] P. Denholm, T. Mai, R. W. Kenyon, B. Kroposki, and M. O'Malley, "Inertia and the power grid: A guide without the spin," National Renewable Energy Laboratory (NREL), Golden, CO, USA, Tech. Rep. NREL/TP-6A20-73856, May 2020, doi: 10.2172/1659820.

[6] EPRI/BPA, "Review of grid reliability services from variable energy resources (VERs) and inverter-based resources (IBRs)," Electric Power Research Institute (EPRI) and Bonneville Power Administration (BPA), Tech. Rep. 3002029347, Palo Alto, CA & Portland, OR, USA, 2024.

[7] IEEE Std 2800-2022, IEEE Standard for Interconnection and Interoperability of Inverter-Based Resources (IBRs) Interconnecting with Associated Transmission Electric Power Systems," The Institute of Electrical and Electronics Engineers, Piscataway, NJ, USA, Apr. 2022, doi: 10.1109/IEEESTD.2022.9762253.

[8] Hydro-Québec, *Technical Requirements for the Connection of Generating Stations to the Hydro-Québec Transmission System, Decision D-2022-088, effective July 15, 2022*, Montréal, QC, Canada, Jul. 2022

[9] U. Karaagac, J. Mahseredjian, H. Gras, H. Saad, J. Peralta, and L. D. Bellomo, "Simulation models for wind parks with variable speed wind turbines in EMTP," Polytechnique Montréal, Montréal, QC, Canada, Tech. Rep., Mar. 2017.

[10] U. Karaagac, H. Ashourian, I. Kocar, A. Stepanov, H. Gras, and J. Mahseredjian, "PV park models in EMTP," EMTP® Documentation, Polytechnique Montréal, Montréal, QC, Canada, Tech. Rep., Jun. 2021.

[11] M. K. Bakhshizadeh, B. Vilmann, and Ł. Kocewiak, "Modal aggregation technique to check the accuracy of the model reduction of array cable systems in offshore wind farms," *Energies*, vol. 15, no. 21, art. no. 7996, Oct. 2022, doi: 10.3390/en15217996.

[12] North American Electric Reliability Corporation (NERC), *Electromagnetic Transient Analysis in Operations Planning for BPS-Connected Inverter-Based Resources* (Draft White Paper), June 2025. Appendix A: “Key Differences Between EMT and RMS-type Simulation Solutions”.

[13] J. Mahseredjian, V. Dinavahi, and J. A. Martinez, “Simulation tools for electromagnetic transients in power systems: Overview and challenges,” *IEEE Trans. Power Delivery*, vol. 24, no. 3, pp. 1657-1669, July 2009, doi: 10.1109/TPWRD.2008.2008480.

[14] A. Stepanov, H. Saad, U. Karaagac, and J. Mahseredjian, “Initialization of Modular Multilevel Converter Models for the Simulation of Electromagnetic Transients,” *IEEE Trans. Power Delivery*, vol. 34, no. 1, pp. 290-300, Feb. 2019, doi: 10.1109/TPWRD.2018.2872883.

[15] O. Alican, C. Collados-Rodriguez, D. W. Spier, M. Cheah-Mañe, E. Prieto-Araujo, and O. Gomis-Bellmunt, “Initialization method of power electronic dominated networks in EMT simulations,” in Proc. 2023 IEEE Belgrade PowerTech, Belgrade, Serbia, Jun. 2023, pp. 498–505, doi: 10.1109/PowerTech55446.2023.10202800.

[16] Y. Coughlan, P. Smith, A. Mullane, and M. O'Malley, "Wind Turbine Modelling for Power System Stability Analysis-A System Operator Perspective," in *IEEE Trans. Power Systems*, vol. 22, no. 3, pp. 929-936, Aug 2007, doi: 10.1109/TPWRS.2007.901649.

[17] F. Blaabjerg, R. Teodorescu, M. Liserre, and A. V. Timbus, “Overview of control and grid synchronization for distributed power generation systems,” *IEEE Trans. Industrial Electronics*, vol. 53, no. 5, pp. 1398–1409, Oct. 2006, doi: 10.1109/TIE.2006.881997.

[18] K. C. Divya and P. S. N. Rao, “Models for wind turbine generating systems and their application in load flow studies,” *Electric Power Systems Research*, vol. 76, no. 9-10, pp. 844-856, Jun. 2006, doi: 10.1016/j.epsr.2005.10.012.

[19] E. Muljadi, N. Samaan, V. Gevorgian, J. Li, and S. Pasupulati, “Short circuit current contribution for different wind turbine generator types,” in *Proc. 2010 IEEE Power & Energy Society General Meeting*, Minneapolis, MN, USA, Jul. 2010, pp. 1-8.

[20] S. M. Muyeen, *Wind Energy Conversion Systems: Technology and Trends*. London, U.K.: Springer, 2012, doi: 10.1007/978-1-4471-2201-5.

[21] K. Burman, D. Helm, T. Mai, A. Brinkman, E. Hale, and D. J. Arent, *Integrating Renewable Energy into the Transmission and Distribution System of the U.S. Virgin Islands*. Golden, CO, USA: National Renewable Energy Laboratory (NREL), Tech. Rep. NREL/TP-6A20-50580, Nov. 2011, doi: 10.2172/1042347.

[22] J. Martínez, P. C. Kjær, P. Rodriguez, and R. Teodorescu, “Short circuit signatures from different wind turbine generator types,” in *Proc. 2011 IEEE/PES Power Systems Conference and Exposition (PSCE)*, Phoenix, AZ, USA, Mar. 2011, pp. 1-7, doi: 10.1109/PSCE.2011.5772497.

[23] Z. J. Čorba, V. A. Katić, B. P. Dumnić, and D. M. Milićević, “In-grid solar-to-electrical energy conversion system modeling and testing,” *Thermal Science*, vol. 16, suppl. 1, pp. S159-S171, 2012, doi: 10.2298/TSCI120224069C.

[24] D. Kolantla, S. Mikkili, S. R. Pendem, and A. A. Desai, “Critical review on various inverter topologies for PV system architectures,” *IET Renewable Power Generation*, vol. 14, no. 17, pp. 3418-3438, Dec. 2020, doi: 10.1049/iet-rpg.2020.0317

[25] F. Blaabjerg, *Control of Power Electronic Converters and Systems, Volume 3*. San Diego, CA, USA: Elsevier Science & Technology, 2021, doi: 10.1016/C2018-0-02098-1.

[26] S. Filizadeh, J. Belanger, F. Fernandez, P. Forsyth, J. Mahseredjian, J. Morales, and G. Lietz, “Electromagnetic transient modeling and simulation of large power systems: EMT simulators for the future grid,” *IEEE Power & Energy Magazine*, vol. 23, no. 4, pp. 53-65, Jul./Aug. 2025, doi: 10.1109/MPE.2024.3515921.

[27] J. F. Medina Padrón and A. E. Feijoo Lorenzo, “Calculating steady-state operating conditions for doubly-fed induction generator wind turbines,” *IEEE Trans. Power Systems*, vol. 25, no. 2, pp. 922-928, May 2010, doi: 10.1109/TPWRS.2009.2036853.

[28] J. B. Ekanayake, L. Holdsworth, and N. Jenkins, “Comparison of 5th order and 3rd order machine models for doubly fed induction generator (DFIG) wind turbines,” *Electric Power Systems Research*, vol. 67, no. 3, pp. 207-215, 2003, doi: 10.1016/S0378-7796(03)00109-3.

[29] M. Wu and L. Xie, “Calculating steady-state operating conditions for DFIG-based wind turbines,” *IEEE Trans. Sustainable Energy*, vol. 9, no. 1, pp. 293–301, Jan. 2018, doi: 10.1109/TSTE.2017.2731661.

[30] M. Z. Kamh and R. Iravani, “Three-phase steady-state model of Type-3 wind generation unit—Part I: Mathematical models,” *IEEE Trans. Sustainable Energy*, vol. 2, no. 4, pp. 477–486, Oct. 2011, doi: 10.1109/TSTE.2011.2156821.

[31] M. Z. Kamh and R. Iravani, “Three-phase steady-state model of Type-3 wind generation unit—Part II: Model validation and applications,” *IEEE Trans. Sustainable Energy*, vol. 3, no. 1, pp. 41–48, Jan. 2012, doi: 10.1109/TSTE.2011.2166415.

[32] V. S. S. Kumar and D. Thukaram, “Accurate steady-state representation of a doubly fed induction machine,” *IEEE Trans. Power Electronics*, vol. 30, no. 10, pp. 5370–5375, Oct. 2015, doi: 10.1109/TPEL.2015.2425140.

[33] G. R. Slemon, “Modelling of induction machines for electric drives,” *IEEE Trans. Industrial Applications*, vol. 25, no. 6, pp. 1126–1131, Nov./Dec. 1989, doi: 10.1109/28.44260.

[34] A. Tapia, G. Tapia, J. X. Ostolaza, and J. R. Saenz, “Modeling and control of a wind turbine driven doubly fed induction generator,” *IEEE Trans. Energy Conversion*, vol. 18, no. 2, pp. 194–204, Jun. 2003, doi: 10.1109/TEC.2003.811727.

[35] CIGRÉ Working Group B4.57, *Modelling of Modular Multilevel Converters (MMC) for Electromagnetic Transient Studies*, CIGRÉ Technical Brochure 604, Paris, France, 2014

[36] H. Saad, J. Peralta, S. Dennetiere, and J. Mahseredjian, "Dynamic averaged and simplified models for MMC-based HVDC transmission systems," *IEEE Trans. Power Delivery*, vol. 28, no. 3, pp. 1723-1730, Jul. 2013, doi: 10.1109/TPWRD.2013.2251912.

[37] A. Feijóo, J. Cidrás, and C. Carrillo, "A third order model for the doubly-fed induction machine," *Electric Power Systems Research*, vol. 56, no. 2, pp. 121–127, Aug. 2000, doi: 10.1016/S0378-7796(00)00116-4.

[38] A. Yazdani and R. Iravani, *Voltage-Sourced Converters in Power Systems: Modeling, Control, and Applications*. Hoboken, NJ, USA: Wiley–IEEE Press, 2010, doi: 10.1002/9780470551563.

[39] P. Rodriguez, A. Luna, R. Teodorescu, F. Blaabjerg, and M. Liserre, "Control of power converters in distributed generation applications," *IEEE Trans. Industrial Electronics*, vol. 60, no. 4, pp. 1491–1508, Apr. 2013, doi: 10.1109/TIE.2012.2194969.

[40] D. de Giudice, F. Bizzarri, D. Linaro, and A. M. Brambilla, "Shooting method based modular multilevel converter initialization for electromagnetic transient analysis," *Int. J. Electr. Power & Energy Syst.*, vol. 157, 2024, Art. No. 109990, doi: 10.1016/j.ijepes.2023.109990.

[41] J. Mahseredjian, "Comportement des réseaux électriques, Multiphase load-flow method" Course notes, Dept. Electrical Engineering, Polytechnique Montréal, Montréal, QC, 2024.

[42] I. Kocar, U. Karaagac, J. Mahseredjian, and B. B. Cetindag, "Multiphase load-flow solution and initialization of induction machines," *IEEE Trans. Power Systems*, vol. 33, no. 2, pp. 1650-1658, Mar. 2018, doi: 10.1109/TPWRS.2017.2721547.

[43] J. Mahseredjian, I. Kocar, and U. Karaagac, "Solution techniques for electromagnetic transients in power systems," in *Transient Analysis of Power Systems: Solution Techniques, Tools and Applications*, M. A. Pai and A. R. van C. Smith, Eds. Hoboken, NJ, USA: John Wiley & Sons, 2015, ch. 2, pp. 9–38, doi: 10.1002/9781118694190.ch2.

[44] N. Rashidirad, J. Mahseredjian, I. Kocar, U. Karaagac, and O. Saad, "MANA-based load-flow solution for islanded AC microgrids," *IEEE Trans. Smart Grid*, vol. 14, no. 2, pp. 889–898, Mar. 2023, doi: 10.1109/TSG.2022.3199762.

[45] A. Feijoo, "On PQ models for asynchronous wind turbines," *IEEE Trans. Power Systems*, vol. 24, no. 4, pp. 1890–1891, Nov. 2009, doi: 10.1109/TPWRS.2009.2030243.

[46] G. Abad, J. Lopez, M. Rodriguez, L. Marroyo, and G. Iwanski, *Doubly Fed Induction Machine: Modeling and Control for Wind Energy Generation*. Hoboken, NJ, USA: John Wiley & Sons, 2011, doi: 10.1002/9781118104965.

[47] K. C. Divya and P. S. N. Rao, “Models for wind turbine generating systems and their application in load flow studies,” *Electric Power Systems Research*, vol. 76, no. 9–10, pp. 844–856, Jun. 2006, doi: 10.1016/j.epsr.2005.10.012.

[48] F. Blaabjerg, *Control of Power Electronic Converters and Systems, Volume 3*. San Diego, CA, USA: Elsevier Science & Technology, 2021, doi: 10.1016/C2018-0-02098-1.

[49] R. Teodorescu, M. Liserre, and P. Rodriguez, *Grid Converters for Photovoltaic and Wind Power Systems*. Hoboken, NJ, USA: John Wiley & Sons, 2011, doi: 10.1002/9780470667059.

[50] A. Timbus, M. Liserre, R. Teodorescu, and F. Blaabjerg, “Synchronization methods for three-phase distributed power generation systems—An overview and evaluation,” in *Proc. 2005 IEEE 36th Power Electronics Specialists Conference (PESC)*, Recife, Brazil, Jun. 2005, pp. 2474–2481, doi: 10.1109/PESC.2005.1581965.

[51] D. Xu, F. Blaabjerg, W. Chen, and N. Zhu, *Advanced Control of Doubly Fed Induction Generator for Wind Power Systems*. Hoboken, NJ, USA: John Wiley & Sons, 2018, doi: 10.1002/9781119172086.

[52] P. Rodriguez, A. Luna, M. Ciobotaru, R. Teodorescu, and F. Blaabjerg, “Advanced grid synchronization system for power converters under unbalanced and distorted operating conditions,” in *Proc. IECON 2006 – 32nd Annual Conference on IEEE Industrial Electronics*, Paris, France, Nov. 2006, pp. 5173–5178, doi: 10.1109/IECON.2006.347725.

[53] North American Electric Reliability Corporation (NERC), *Reliability Guideline: Electromagnetic Transient Modeling for BPS-Connected Inverter-Based Resources — Recommended Model Requirements and Verification Practices*, March 2023. Available: https://www.nerc.com/globalassets/who-we-are/standing-committees/rstc/irps/reliability_ guideline-emt _modeling_and_simulations.pdf

[54] T. J. Aprille and T. N. Trick, “Steady-state analysis of nonlinear circuits with periodic inputs,” *Proc. IEEE*, vol. 60, no. 1, pp. 108–114, Jan. 1972, doi: 10.1109/PROC.1972.8563.

[55] M. S. Nakhla and F. H. Branin Jr., “Determining the periodic response of nonlinear systems by a gradient method,” *Int. J. Circuit Theory Appl.*, vol. 5, no. 3, pp. 255–273, Jul. 1977, doi: 10.1002/cta.4490050307.

[56] B. K. Perkins, J. R. Marti, and H. W. Dommel, “Nonlinear elements in the EMTP: steady-state initialization,” *IEEE Trans. Power Systems*, vol. 10, no. 2, pp. 593–601, May 1995, doi: 10.1109/59.387893.

[57] K. L. Lian and T. Noda, “A time-domain harmonic power-flow algorithm for obtaining nonsinusoidal steady-state solutions,” *IEEE Trans. Power Delivery*, vol. 25, no. 3, pp. 1888–1898, Apr. 2010, doi: 10.1109/TPWRD.2010.2043547.

[58] J. Mahseredjian, S. Dennetière, L. Dubé, B. Khodabakhchian, and L. Gérin-Lajoie, “On a new approach for the simulation of transients in power systems,” *Electric Power Systems Research*, vol. 77, no. 11, pp. 1514–1520, Oct. 2007, doi: 10.1016/j.epsr.2006.08.027.

[59] K. W. Louie, A. Wang, P. Wilson, and P. Buchanan, “Discussion on the initialization of the EMTP-type programs,” in *Proc. Canadian Conf. on Electrical & Computer Engineering (CCECE)*, Saskatoon, SK, Canada, Jan. 2005, pp. 1962–1965, doi: 10.1109/CCECE.2005.1557367.

[60] V. Sangsawang and S. Chaitusaney, “Modeling of photovoltaic module from commercial specification in datasheet,” in *Proc. 2012 9th International Conference on Electrical Engineering/Electronics, Computer, Telecommunications and Information Technology (ECTI-CON)*, Phetchaburi, Thailand, Aug. 2012, pp. 1–4, doi: 10.1109/ECTICon.2012.6254222.

[61] V. J. Chin, Z. Salam, and K. Ishaque, “Cell modelling and model parameters estimation techniques for photovoltaic simulator application: A review,” *Applied Energy*, vol. 154, pp. 500–519, Sept. 2015, doi: 10.1016/j.apenergy.2015.05.035.

[62] O. Anaya-Lara, N. Jenkins, J. Ekanayake, P. Cartwright, and M. Hughes, *Wind Energy Generation: Modelling and Control*, 1st ed. Chichester, U.K.: John Wiley & Sons, 2009, doi: 10.1002/9780470714333.

[63] M. Sarkar, M. Altin, P. E. Sørensen, and A. D. Hansen, “Reactive power capability model of wind power plant using aggregated wind power collection system,” *Energies*, vol. 12, no. 9, pp. 1607–1615, Apr. 2019, doi: 10.3390/en12091607.

[64] L. M. Fernández, F. Jurado, and J. R. Saenz, “Aggregated dynamic model for wind farms with doubly fed induction generator wind turbines,” *Renewable Energy*, vol. 33, no. 1, pp. 129–140, Jan. 2008, doi: 10.1016/j.renene.2007.01.010.

[65] M. Singh and S. Santoso, *Dynamic Models for Wind Turbines and Wind Power Plants*. Golden, CO, USA: National Renewable Energy Laboratory (NREL), Tech. Rep. NREL/SR-5500-52780, Mar. 2011, doi: 10.2172/1026413.

[66] P. Lacasse, L. Gerin-Lajoie, D. McNabb, P.-J. Lagacé, and J. Mahseredjian, “New initialization method for controls in transient analysis,” in *Proc. 2001 IEEE Power Engineering Society Winter Meeting. Conference Proceedings (Cat. No. 01CH37194)*, vol. 3, Columbus, OH, USA, Jan. 2001, pp. 1317–1322, doi: 10.1109/PESW.2001.917153.

[67] J. M. Garcia, *Voltage Control in Wind Power Plants with Doubly Fed Generators*. Aalborg, Denmark: Department of Energy Technology, Aalborg University, 2010.

[68] A. Haddadi, J. Mahseredjian, “Power system test cases for EMT-type simulation studies,” CIGRE Technical Report, Aug. 2018

[69] IEEE Power & Energy Society, *IEEE PES Test Feeder* [Online]. Available: https://cmte.ieee.org/pes-testfeeders/resources/. [Accessed: Apr. 1, 2024].

[70] M. D. Liu, K. Jacobs, and J. Mahseredjian, “Load-flow time-series simulation of a distribution grid with PV modules and voltage regulation,” in *Proc. 2023 IEEE Belgrade PowerTech*, Belgrade, Serbia, Aug. 2023, pp. 1–7, doi: 10.1109/PowerTech55446.2023.10202710.

[71] U. Karaagac, J. Mahseredjian, R. Gagnon, H. Gras, H. Saad, L. Cai, I. Kocar, A. Haddadi, E. Farantatos, S. Bu, K. W. Chan, and L. Wang, “A generic EMT-type model for wind parks with permanent magnet synchronous generator full size converter wind turbines,” *IEEE Power Energy Technol. Syst. J.*, vol. 6, no. 3, pp. 131–141, Sept. 2019, doi: 10.1109/JPETS.2019.2928013.

[72] E. Muljadi, S. Pasupulati, A. Ellis, and D. Kosterev, “Method of equivalencing for a large wind power plant with multiple turbine representation,” in *Proc. 2008 IEEE Power Engineering Society General Meeting*, Pittsburgh, PA, USA, Jul. 2008, pp. 1–8, doi: 10.1109/PES.2008.4596055.

[73] J. Brochu, C. Larose, and R. Gagnon, “Validation of single- and multiple-machine equivalents for modeling wind power plants,” *IEEE Trans. Energy Convers.*, vol. 26, no. 2, pp. 532–541, Jun. 2011, doi: 10.1109/TEC.2010.2087337.

[74] Analytic Methods for Power Systems Committee, Transient Analysis and Simulations Subcommittee, Wind SSO Task Force, *PES-TR80: Wind Energy Systems Sub-Synchronous Oscillations: Events and Modeling*, IEEE Power & Energy Society, Tech. Rep., Jul. 2020. [Online]. Available: https://resourcecenter.ieee-pes.org/publications/technical-reports/pes_tp_tr80_amps_wsso_070920. [Accessed: Mar. 19, 2024].

[75] A. Stepanov, H. Saad, U. Karaagac, and J. Mahseredjian, “Initialization of modular multilevel converter models for the simulation of electromagnetic transients,” *IEEE Trans. Power Delivery*, vol. 34, no. 1, pp. 290–300, Feb. 2019, doi: 10.1109/TPWRD.2018.2872883.

[76] J. Slootweg, H. Polinder, and W. Kling, "Initialization of wind turbine models in power system dynamics simulations," in 2001 IEEE Porto Power Tech Proceedings (Cat. No. 01EX502), 2001, vol. 4: IEEE, p. 6 pp. vol. 4.

[77] N. W. Miller, J. J. Sanchez-Gasca, W. W. Price, and R. W. Delmerico, “Dynamic modeling of GE 1.5 and 3.6 MW wind turbine-generators for stability simulations,” in *Proc. 2003 IEEE Power Engineering Society General Meeting*, Toronto, ON, Canada, Jul. 2003, pp. 1977–1983, doi: 10.1109/PES.2003.1267470.

[78] J. A. Ocampo-Wilches, A. Ramirez, K. Jacobs, J. Mahseredjian, and A. G. Pavani, “Full-control initialization of photovoltaic park models for electromagnetic transient simulations,” in *Proc. IECON 2024 – 50th Annual Conference of the IEEE Industrial Electronics Society*, Chicago, IL, USA, 2024, pp. 1–8, doi: 10.1109/IECON55916.2024.10905292.

[79] “Caledonian Cable,” CaledonianCable.com. [Online]. Available: http://www.caledoniancable.com/English/index.htm. [Accessed: Jul. 09, 2024].

[80] A. Haddadi, and J. Mahseredjian, CIGRÉ Working Group C4.503, *Power System Test Cases for EMT-Type Simulation Studies*, CIGRÉ Technical Report, Aug. 2018. [Online]. Available: https://www.e-cigre.org/publications/detail/736-power-system-test-cases-for-emt-type-simulation-studies.html. [Accessed: Mar. 19, 2024].

[81] F. de Leon, R. A. Jabr, K. Uhlen, K. W. Louie, A. C. Smith, and A. M. Gole, “Development of data translators for interfacing power-flow programs with EMTP-type programs: Challenges and lessons learned,” *IEEE Trans. Power Delivery*, vol. 28, no. 2, pp. 1192–1201, Apr. 2013, doi: 10.1109/TPWRD.2012.2227836.

[82] J. F. Medina Padron and A. E. Feijoo Lorenzo, “Calculating steady-state operating conditions for doubly-fed induction generator wind turbines,” *IEEE Trans. Power Systems*, vol. 25, no. 2, pp. 922–928, May 2010, doi: 10.1109/TPWRS.2009.2036853.

[83] Y. Dong, Z. Yang, J. Wang, H. Zhang, and L. Huang, “A novel electromagnetic transient simulation method of large-scale AC power system with high penetrations of DFIG-based wind farms,” *IEEE Access*, vol. 10, pp. 53188–53199, 2022, doi: 10.1109/ACCESS.2022.3175891.

[84] J. A. Ocampo-Wilches, J. Mahseredjian, K. Jacobs, A. G. Pavani, and H. Xue, “Comprehensive full-scale converter wind park initialization for electromagnetic transient studies,” *IEEE Trans. Power Delivery*, 2025, doi: 10.1109/TPWRD.2025.3551546.

[85] H. Yuan, R. S. Biswas, J. Tan, and Y. Zhang, “Developing a reduced 240-bus WECC dynamic model for frequency response study of high renewable integration,” in Proc. 2020 IEEE/PES Transmission and Distribution Conference and Exposition (T&D), Chicago, IL, USA, Oct. 2020, pp. 1–5, doi: 10.1109/TD39804.2020.9299942.

[86] A. Allabadi, J. Mahseredjian, K. Jacobs, I. Kocar, and T. Ould-Bachir, “Initializing EMT models of grid-forming VSCs in MTDC systems,” *Electric Power Systems Research*, vol. 235, Art. no. 110674, Jul. 2024, doi: 10.1016/j.epsr.2024.110674.

[87] V. Vittal and R. Ayyanar, *Grid Integration and Dynamic Impact of Wind Energy*, in Kluwer International Series in Engineering and Computer Science: Power Electronics & Power Systems. New York, NY, USA: Springer Science & Business Media, 2012, doi: 10.1007/978-1-4614-1306-3.

[88] I. Kocar and J. Mahseredjian, “Accurate frequency dependent cable model for electromagnetic transients,” *IEEE Trans. Power Delivery*, vol. 31, no. 3, pp. 1281–1288, Jun. 2016, doi: 10.1109/TPWRD.2015.2481323.

APPENDIX A CABLE PARAMETERS

The parameters of the cable shown in Figure 3.15 and its layout in the offshore WP shown in Figure 3.13, are summarized in the following tables:

Table 6.1 Parameters of seawater and seabed

Parameter	Seawater	Seabed
Depth (m)	15	1×10^{15}
Resistibity (Ωm)	0.2	5
Relative permittivity (ε_r)	80	15
Relative permeability (μ_r)	1	1

Table 6.2 Parameters of pipe-type cable

Number of cores	3	Relative permittivity (ε_r)	1
Horizontal position (m)	0	Relative permeability (μ_r)	600
Vertical position (m)	16.5	Resistivity (Ωm)	2.48×10^{-7}
Pipe outer radius (cm)	4.578	Number of stranded wires	66
Pipe inner radius (cm)	4.228	Total radius (cm)	2.3
Inner insulator relative permittivity (ε_r)	2.3	Outer insulator relative permittivity (ε_r)	4.978

Table 6.3 Parameters of pipe-type cable cores

Core	1	2	3
Distance from center (cm)	2.154	2.154	2.154
Angle (deg)	0	120	240
Outer radius (cm)	1.865	1.865	1.865
Number of conductors	2	2	2

Table 6.4 Parameters of conductors/insulators per core

Parameter	Conductor 1	Conductor 2
Inner radius (cm)	0	1.505
Outer radius (cm)	0.575	1.675
Number of stranded wires	1	1
Conductor resistibity (Ωm)	1.678×10^{-8}	2.198×10^{-7}
Conductor relative permeability (μ_r)	1	1
Conductor relative permittivity (ε_r)	1	1
Insulator relative permittivity (ε_r)	2.5	2.3